HEINRICH HEINE
UNIVERSITÄT DÜSSELDORF

3D-Drug-Printing:
Extrusion of Printable Drug-Loaded Filaments and Development of Novel Solid Dosage Forms

Inaugural-Dissertation

zur Erlangung des Doktorgrades der Mathematisch-Naturwissenschaftlichen Fakultät der
Heinrich-Heine-Universität Düsseldorf

vorgelegt von

Carolin Korte

aus Haltern am See

Düsseldorf, August 2018

aus dem Institut für Pharmazeutische Technologie und Biopharmazie
der Heinrich-Heine-Universität Düsseldorf

Gedruckt mit der Genehmigung der
Mathematisch-Naturwissenschaftlichen Fakultät der
Heinrich-Heine-Universität Düsseldorf

Berichterstatter:

1. Prof. Dr. Jörg Breitkreutz
2. Prof. Dr. Dr. h.c. Peter Kleinebudde

Tag der mündlichen Prüfung: 14.11.2018

Publications

Parts of this doctoral thesis have already been published in peer-reviewed journals:

Formulation Development and Process Analysis of Drug-loaded Filaments manufactured via Hot-Melt Extrusion for 3D-Printing of Medicines

C. Korte, J. Quodbach, Pharm. Dev. Technol., 2018, 23(10), pp. 1117-1127, DOI: 10.1080/10837450.2018.1433208

Evaluation of the authorship

author/ co-author	idea [%]	study design [%]	experimental [%]	evaluation [%]	manuscript [%]
Carolin Korte	40	50	100	70	80
Julian Quodbach	60	50	0	30	20

The idea and the study design for the paper “Formulation Development and Process Analysis of Drug-loaded Filaments manufactured via Hot-Melt Extrusion for 3D-Printing of Medicines” was developed by both authors in cooperation. The conduction of the experiments, the evaluation of the obtained data and writing of the manuscript was done by Carolin Korte. Julian Quodbach was further responsible for supporting the data evaluation and for the revision of the manuscript.

3D-Printed Network Structures as Controlled Release Drug Delivery Systems: Dose Adjustment, API Release Analysis and Prediction

C. Korte, J. Quodbach, AAPS Pharm SciTech, 2018, 19(8), pp. 3333-3342, DOI: 10.1208/s12249-018-1017-0

Evaluation of the authorship

author/ co-author	idea [%]	study design [%]	experimental [%]	evaluation [%]	manuscript [%]
Carolin Korte	85	100	100	90	80
Julian Quodbach	15	0	0	10	20

Carolin Korte has developed the basic idea and the study design. She conducted the experimental work, evaluated the data and wrote the manuscript. Julian Quodbach assisted in the development of the concept and supported the data evaluation. He was further responsible for the revision of the manuscript.

Oral Presentations

Parts of this doctoral thesis have been presented in oral presentations at international conferences and symposia:

C. Korte, J. Breitkreutz, J. Quodbach, *Evaluation of the thermal load during 3D-printing via an IR camera,* Workshop 3D Printing in Pharmaceutical and Biomedical Applications – Possibilities and Challenges, oral presentation, Hiddensee 2016

C. Korte, J. Breitkreutz, J. Quodbach, *PAT for 3D-printing: Assessment of the thermal profile of nozzle and filament,* 10th Annual PSSRC Symposium, oral presentation, Copenhagen 2016

C. Korte, J. Quodbach, *Pilot scale twin-screw extrusion: formulation development of 3D-printable filaments,* 11th Annual PSSRC Symposium, oral presentation, Graz 2017

Posters

Parts of this doctoral thesis have been presented in poster presentations at international conferences and symposia:

C. Korte, J. Breitkreutz, J. Quodbach, *Drug-loaded HPC filaments produced via twin-screw extrusion for 3D-printing,* 10th World Meeting on Pharmaceutics, Biopharmaceutics and Pharmaceutical Technology, poster presentation, Glasgow 2016

C. Korte, J. Breitkreutz, J. Quodbach, *Theophylline-loaded 3D-printable filaments produced via twin-screw extrusion,* 2nd European Conference on Pharmaceutics, poster presentation, Krakow 2017

C. Korte, J. Breitkreutz, J. Quodbach, *Thermometric evaluation of 3D FDM printing process* 2nd European Conference on Pharmaceutics, poster presentation, Krakow 2017

C. Korte, J. Quodbach, *Effect of HME process parameters on quality attributes of 3D-printable filaments,* 9th Polish-German Symposium on Pharmaceutical Sciences, poster presentation, Krakow 2017

C. Korte, J. Quodbach, *3D-printed network structures as novel solid dosage form: Dose adaption and prediction of dissolution profiles,* 11th World Meeting on Pharmaceutics, Biopharmaceutics and Pharmaceutical Technology, poster presentation, Granada 2018

Table of Contents

Abbreviations

3PB	three-point bending
A	adenosine receptors
API	active pharmaceutical ingredient
aPMMA	ammonio methyacrylate copolymer type A (Ph. Eur.), Eudragit® RL
bPMMA	basic butylated methacrylate copolymer (Ph. Eur.), Eudragit® E
CAD	computer-aided design
CBS	conveyor belt speed [mm/s]
CI	confidence interval
CNC	computerized numerical control
$c_{p,m}$	molar heat capacity
DDS	drug delivery system
DIN	Deutsches Institut für Normung
DoE	design of experiments
DSC	differential scanning calorimetry
E_{mod}	modified Young’s modulus; slope between 0.05 and 0.25 % elongation in a force-elongation-curve
FDM™	fused deposition modeling
FFT	fast Fourier transform
(TS)HME	(twin-screw) hot-melt extrusion
HPC	hydroxypropyl cellulose, MW = 850,000 g/mol
IR	infrared
ISO	International Organization for Standardization
MRT	median residence time during hot-melt extrusion
MW	molecular weight
PEG300	macrogol 300 (Ph.Eur.), polyethylene glycol MW = 300 g/mol

PEG4000	macrogol 4000 (Ph.Eur.), polyethylene glycol MW = 4000 g/mol
PFR	powder feed rate [g/min]
Ph.Eur	European Pharmacopoeia
PI	proportional-integral
PLA	polylactic acid
PVA	polyvinyl alcohol
Q^2	measure of predictive power
R^2	coefficient of determination
RMSEP	root mean square error of prediction
RPM	screw speed of the twin-screw extruder [rpm]
SA	stearic acid
SSA	specific surface area
TEMP	extrusion temperature [°C]
T_m	melting temperature
USP	United States Pharmacopoeia
YM	Young’s modulus, modulus of elasticity

1. Introduction

1.1. Opportunities, Challenges and Limitations of 3D-Printing as Production Technology for Drug-Loaded Dosage Forms

Paediatric and geriatric patients represent groups of the population benefiting from progress in the production of highly individualized drug delivery systems (DDS), since they show physical particularities. Neonates and infants do not only exhibit less body weight than adults. Enzymes, efflux transporters and metabolizing organs are not yet fully developed and larger specific surfaces of skin, lung and the gastrointestinal tract contribute to differences in drug metabolism compared to grown-ups [1, 2]. Elderly, on the other hand, often exhibit decreased function of metabolizing organs, e.g. kidney and liver, and express age-related differences in transmitters and receptors [3, 4]. A reduced amount of muscles and comparatively increased fat mass, influence the distribution volume of drugs [3]. Common means to individualize doses for patients are to administer an adapted amount of a liquid preparation (i.v. or p.o.) or to fill capsules [5]. Both methods are limited for the administration of drugs in a sustained-release manner. This might be achieved by crushing tablets, cutting drug-loaded rods to an individual size or measuring a certain amount of multi particulates, e.g. mini tablets or pellets [6, 7]. Highly customized medicinal products are likely to increase compliance and drug effectiveness with simultaneous reduction of side effects [8].

In this regard, 3D-printing might be a new and versatile technique, which could be suitable for the on-site production of sustained-release matrices for oral or parental use, customized regarding shape and dose. 3D-printing is claimed to enable customized dosing, dose combinations of medicines, tailored dissolution profiles and production of DDSs, whose shapes are individually adapted to the patient, e.g. as an implant [9-12]. It is characterized by building up the desired product layer-by-layer. Thereby, objects might be manufactured, which cannot be manufactured via established pharmaceutical production techniques, e.g. injection moulding or tableting. Such structures might be hollow or highly sophisticated (Figure 1). Complex objects might enable varying release profiles or fulfil requirements for implantable devices, since endogenous structures could be mimicked [13]. Size, and thereby dose, of the dosage forms can easily be adapted, since scaling of the object via the printer controlling software is feasible [14, 15]. In contrast to established production techniques of solid dosage forms in the pharmaceutical field, no change of the apparatus or equipment is necessary. However, high individualization is also realized at the expense of throughput. Therefore, 3D-printing might preferably be used in the field of extemporaneously compounded medicines and less in the pharmaceutical industry.

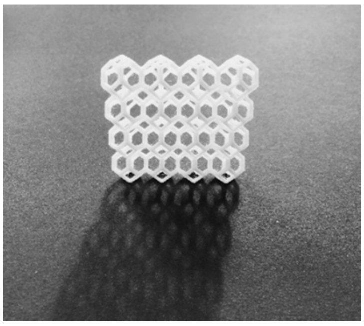

Figure 1. 3D-printed object produced from commercial PLA filament.
The computer-aided design file was modified from a template provided by thingiverse.com [16].

3D-printing has already been shown to be suitable for the production of different drug combinations, which can be tailored to the patient's needs. Acetylsalicylic acid, hydrochlorothiazide, pravastatin, atenolol and ramipril were combined via printing in a five-dose combination poly-pill containing different drug-loaded sections [17]. Captopril, nifedipine and glipizide as drug combination in the treatment of arterial hypertension in type II diabetes were successfully printed in one dosage form achieving different release mechanisms. Nifedipine and glipizide were released via diffusion, whereas for captopril an osmotic pump was created by means of printing causing zero order release [18].

Despite many opportunities, in particular regarding customization of medication, 3D-printing also involves certain limitations. Limitations concerning the particular printing technique are presented in the corresponding section. General limitations for all 3D-printing techniques are mainly related to regulatory issues [19]. With regard to the production of compounded drugs, liability in case of an adverse incident is a key topic. Until now, it is not clarified, who would be the manufacturer in this case and who would assume the responsibility for the quality of the dosage form. The operator of the printer, the developer of the three-dimensional software file, the producer of the filament as bulk material, the owner of the pharmacy or hospital and the responsible pharmacist might be taken into consideration [20]. For this, however, it has to be clarified, if conditions for a magistral formula or an officinal formula mentioned in directive 2001/83/EC (article 3, 1° and 2°) or for extemporaneous preparations defined in the Ordinance on the Operation of Pharmacies [21] are fulfilled.

Open questions are also related to cleaning issues impeding cross-contamination. This problem might be solved, if machine producers put more effort in the development of printers appropriate for Good Manufacturing Practice.

For reasons of clarification, the Food and Drug Administration established working groups for research on safety, effectiveness, quality and resilience of 3D-printed medical devices and medicinal products [22]. These efforts, however, clearly focus on industrial production and even bore fruit with the approval of Aprecia's ZipDose® as first commercially available 3D-printed dosage form. In this particular case, main motivation for using 3D-printing for the production were not related to customization, but rather to very fast disintegration of the dosage form, which could be achieved by powder bed printing [23]. For the establishment of 3D-printing in the industrial environment, implementation of process analytical technology tools might be of importance. First studies using Fourier-transform infrared spectroscopy and terahertz spectroscopy were conducted off-line and promised applicability of these technologies in 3D-printing processes [24, 25].

1.2. 3D-Printing Techniques

3D-printing is classified as an additive manufacturing technique. This means in particular that objects are built up layer-by-layer following the production process shown in Figure 2. For all 3D-printing techniques the production process is based on the same steps. Typically, a three-dimensional computer-aided design (CAD) drawing of the object, which shall be printed, is created using a CAD software. Shape information is then translated into an .stl-file describing the surface of the object in triangles. This file is then processed with the slicing software, cutting the object in slices or layers of a predefined height [26]. Thereby, a file written in G-code, containing commands for the printer, is created. G-code is a common programming language used for numerically controlled machines. It contains all information for the printer how the object should be built up, e.g. movements of the different printer parts and their speed. Then, the object can be printed beginning with the bottom layer. Theoretically, every geometry is printable. Some of the 3D-printing techniques require support structures, if overhangs shall be created. Other 3D-printing techniques work with powder particles. Both, support structures and residual powder, have to be removed in a post-processing step.

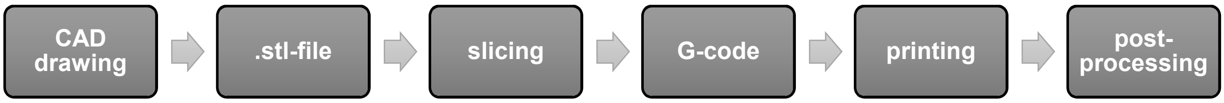

Figure 2. Flow chart depicting a typical production process using 3D-printing.

The most important 3D-printing techniques are schematically depicted in Figure 3. In stereolithography (Figure 3 a) a resin is photopolymerised on a build plate using a laser beam. The build plate is positioned in a resin bath. After solidifying the first layer, the build plate moves down to a predefined height and the next layer is produced likewise. A rotating mirror allows movement of the laser spot and, thereby, solidification in the whole x-y-plane [27]. Stereolithography enables printing with high resolution and accuracy. Nevertheless, serious disadvantages of this method are the limited availability of resins meeting pharmaceutical standards and the incalculable risk of residual monomers, which might be toxic [8, 13].

The technique used to produce Aprecia's ZipDose® is called binder deposition method. A binder solution is printed, using inkjet printing, onto a powder bed (Figure 3 b1, b2). After each layer, the build plate moves down and a new layer of powder is spread, either via a scraper (Figure 3 b1) or via spraying (Figure 3 b2). Mechanisms of solidification are the same as for wet granulation: particle bridges might be built by the binder or by the particles via solution and recrystallization [8]. The active pharmaceutical ingredient (API) might be incorporated in the powder bed or in the binder solution. In pharmaceutics, different binder solutions, e.g. containing Eudragit® E (bPMMA), Eudragit® RL (aPMMA) or polyvinylpyrrolidone, have been evaluated, enabling different dissolution profiles [28, 29]. Highly porous structures for rapid disintegration can be produced [23] at a high resolution and room temperature. The powder bed serves as scaffold structure in the process and, thereby, facilitates printing of sophisticated structures and overhangs [8]. However, additional drying [13], high friability, low mechanical resilience [28] as well as indispensable removal of residual powder as post-processing step are major drawbacks of this technique.

Selective laser sintering might be considered as combination of stereolithography and binder deposition (Figure 3, c). Similar to stereolithography a laser beam deflected by a mirror is applied. However, it is radiated on a powder bed, which is built up using a scraper. Powder particles are sintered by the energy of the laser beam. They melt and consequently solidify [30]. This method is commonly used for metals, since the energy input is high and might involve API degradation [13, 31], but was recently also investigated to produce pharmaceuticals [32, 33].

In extrusion-based techniques, the entire building material is forced through the print head. No powder bed or resin bath is needed. Consequently, layering can be performed onto surfaces of any kind, flat, concave or convex ones [34]. Extruded material might be in a solid state as filament (Figure 3, e) or in semisolid state as pastes or suspensions (Figure 3, d). Suitable materials might have very different physico-chemical properties. Poly(meth)acrylates [15, 24, 35], silicones [36], cellulose derivatives [11, 37-40], polylactides [38, 41, 42], polyvinyl alcohol [43] and waxes [44] have already been shown as printable materials at a pharmaceutical grade. Processing of semisolids is advantageous, since this can take place at room temperature. However, for avoidance of nozzle clogging several preparations contain dimethyl sulfoxide or acetone [17, 18], which are classified as solvents in Class 3 according to the ICH guideline for residual solvents [45]. This means that the permitted daily exposure is limited to 50 mg in pharmaceuticals and that these solvents are not suitable for paediatric preparations. Further, a comparatively low resolution, shrinking or deformation of the product and drying as post processing step are major drawbacks [13].

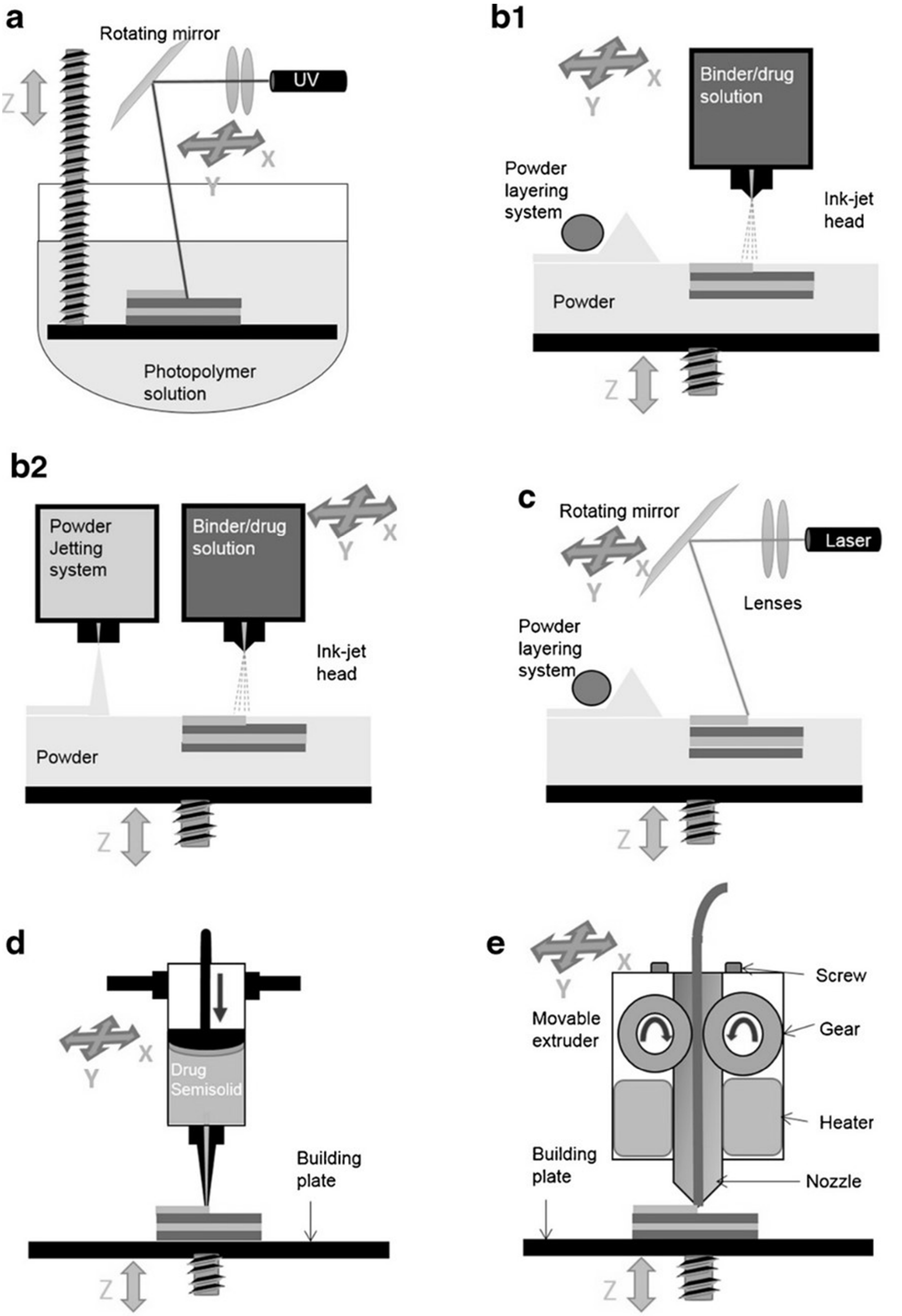

Figure 3. Techniques of 3D-printing: (a) stereolithography, (b1, b2) powder bed and powder jetting, (c) selective laser sintering, (d) semi-solid extrusion, (e) FDM^{TM} (modified from [13], by courtesy of Springer Nature).

During the present work, fused deposition modelling (FDM^{TM}) was chosen as extrusion-based production method. It processes solid-state material as polymer strand, also called filament. Main reason to choose FDM^{TM} was that it was considered as a promising approach for compounding of drugs at local or hospital pharmacies in the future. For this, industrially produced drug-loaded filaments might serve as printer feedstock. Since the API is fixed in the polymer matrix, processing of highly potent APIs, e.g. hormones, at a low risk for the operator might be feasible. Further, problems related to segregation cannot occur. This is likely to ensure a homogeneous quality of the dosage forms, which should mainly be influenced by the homogeneity of drug distribution along the filament. Further, post-processing is normally not needed, only in case of using supporting structures for possible overhangs. However, thermal stress and, thereby, potential thermal decomposition of API or polymer during FDM^{TM} printing and eventually during filament production are a major problem of this technique. This was already shown for salicylic acid and 4-aminosalicylic acid [46, 47]. Printers should be used, which ensure that a narrow pre-set temperature range will be kept. Questions of liability are important to answer in advance, in case irregularities occur in this regard. All methods based on deposition of material through a nozzle further involve problems of potential nozzle clogging.

Moreover, various printing techniques might also be combined. In this concern, FDM^{TM} and liquid dispensing, similar to inkjet or piezoelectric printing, were combined to print capsule shells, which were filled with liquid material in the same process [48, 49].

The printer applied during the present work is shown in Figure 4. It contains two print heads, a left and a right one, which could be used for printing two different filaments within one print job. Most studies of the present work were conducted with commercially provided print heads, called print heads type I in the following. Prior to the last printing study (section 3.4.4), these were replaced by print heads type II, containing a different conveying system.

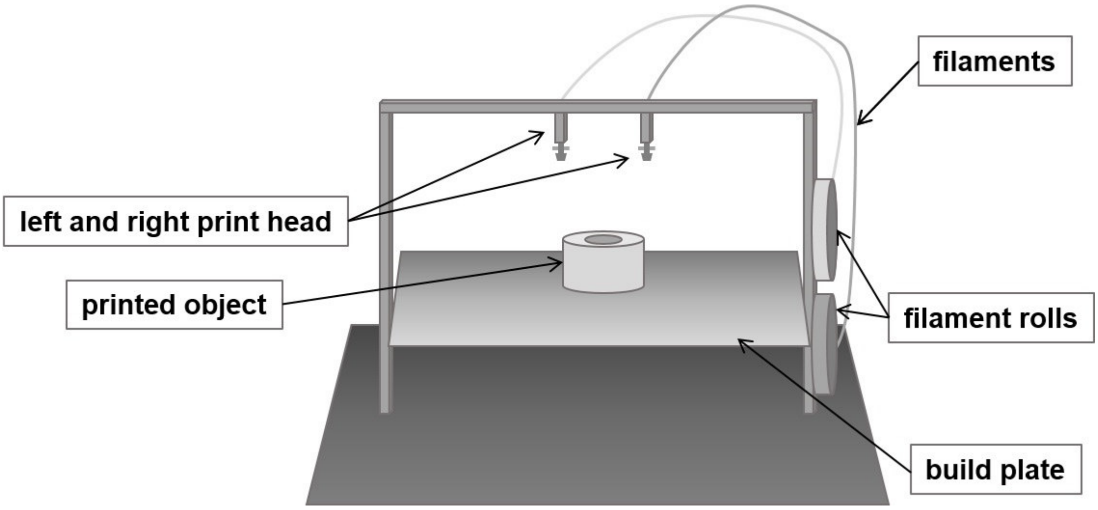

Figure 4. Schematic sketch of the FDM^{TM} printer (Prodim XXL pro) used for the printing studies.

1.3. Production Methods for 3D-Printable Filaments

The common production method of filaments as feedstock for an FDM^{TM} printer is hot-melt extrusion (HME). However, filaments of material at a pharmaceutical grade or loaded with API are not commercially available, so far.

Mechanical resilience of filaments containing pharmaceutical grade excipients is often a problem [35, 50], since filaments are mechanically stressed in various ways during the printing process. Therefore, the first approach was to process commercial non-pharma grade filaments. These starting materials were either soaked with an API containing solvent [14, 51] or they were grinded and subsequently extruded after adding API as powder [42, 52-54]. This might be suitable for first trials, but commercial filaments contain many excipients, which increase mechanical resilience, but are not pharmaceutically usable. Further, soaking only led to drug loads up to 2 % and organic solvents might degrade the API or further excipients. Furthermore, adjustment of the drug load is not feasible with this method.

Most publications on HME of printable filaments present a production process using micro-conical twin-screw extruders, working with batch sizes between 4.5 and 7 g [15, 42, 52, 55-58]. This might be suitable for formulation development, in particular in case of dealing with expensive APIs or excipients. However, batch sizes are so small that without considering production losses in extrusion or printing, approximately 10 tablets at an average size might be printed (450 to 700 mg per dosage form). An open barrel of a micro-conical twin-screw extruder is displayed in Figure 5. Usually, the extruder outlet is closed at the beginning of the process to allow blending of the mixture by rotating screws in the heated barrel. Subsequently, the outlet is opened and the mixture is extruded at once. These processes are not versatile regarding the screw configuration, flexible dosing of liquid plasticizer or continuous processing. Changing the screw configuration and location of the liquid plasticizer feed, however, might be needed to adapt the process to particular materials. The opportunity of continuous processing would also be of great importance to bring filament extrusion into pharmaceutical industry. Some working groups performed filament extrusion using a single-screw extruder [47, 59, 60], originally designed for non-professionals to create their own filament mixtures. These extruders do not meet standards of pharmaceutical equipment, on the one hand. On the other hand, twin-screw extruders are preferred in pharmaceutical industry, e.g. due to better feeding and melting properties, extensive mixing, the possibility of degassing and self-wiping characteristics [61]. A rather exceptional approach of filament production was presented by Costa et al. [62]. They performed a small-scale injection moulding process using a silicone tube, in which they injected a heated mixture of poloxamine, poly-ε-caprolactone and dexamethasone. After solidification, the tube was removed and a filament was obtained. This method allows exact predetermination of the diameter, which is very advantageous.

Nevertheless, this process cannot be used in a continuous manner and is limited to small scale applications.

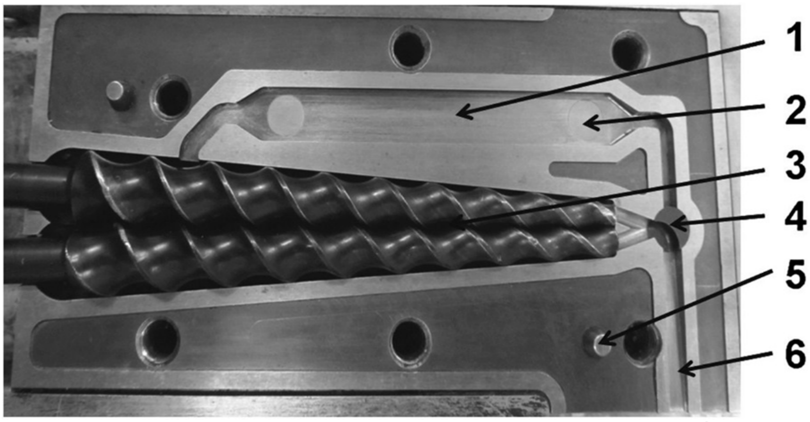

Figure 5. Open barrel of a micro-conical twin-screw extruder (HAAKE MiniLab): backflow channel (1), pressure probe (2), conical screws (3), bypass valve (4), temperature probe (5), extrusion channel (6) (adopted from [63], by courtesy of Elsevier).

Recently (in 2017), first studies were published by Zhang et al. applying an 11 mm hot-melt twin-screw extruder for filament production [64, 65]. Although further upscaling might be desirable, these were the first processes run continuously and offering adequate process flexibility. In the present work, continuous production of 3D-printable filaments should be performed using a 16 mm 40 D twin-screw extruder.

1.4. Theophylline as Model Drug

Theophylline was chosen as model drug in this work. The chemical structure of theophylline is depicted in Figure 6. It is assigned to the group of methylxanthines [66], to which also caffeine and theobromine as pharmacologically important substances belong. Related drugs containing a purine as heterocyclic compound are 6-mercaptopurine, thioguanine and azathioprine.

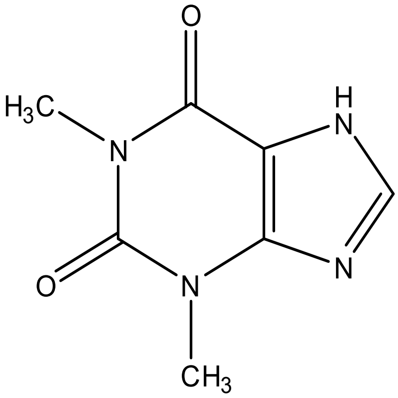

Figure 6. Chemical structure of anhydrous theophylline.

In recent years, theophylline lost importance in medical treatment, but is still administered as anti-asthmatic drug in some cases of asthma for adults from step 2 to 4 and as add-on for children and adolescents in step 4 [67]. Further, it is used in treatment of chronic obstructive pulmonary disease [68]. It can be used in acute attacks as immediate release formulation or as infusion [67]. For chronic drug therapy, however, only sustained-release formulations are suitable [68]. Theophylline shows a half-life of 9 h and is metabolized hepatically via cytochrome P450 1A2. This metabolizing enzyme may be induced by smoking [69]. This is in particular a problem in treatment of chronic obstructive pulmonary disease induced by long-term smoking.

Theophylline shows multiple mechanisms of action within the human body. Most prominent ones, which occur in the therapeutic range of 5 to 15 mg/L in plasma [68], are the inhibition of phosphodiesterases and antagonism of adenosine receptors (A). Phosphodiesterase inhibition is non-selective and comparatively weak. However, phosphodiesterase 3 is inhibited predominantly. Antagonizing of adenosine is mostly effective at subtypes A1 and A2 [70]. Thereby, airways are relaxed and bronchodilation occurs. Reasons for recent loss of importance were the comparatively low efficacy and severe side effects. These occur more frequently at > 20 mg/L in plasma. Side effects include, besides common ones, such as headache, nausea and gastroesophageal reflux, severe cardia arrhythmias, probably caused by the A1 receptor blockade [70]. Advantages of theophylline therapy, however, are its good availability and its inexpensiveness.

For the present work, theophylline was suitable as model drug due to several different reasons. First, theophylline is considered to be thermally stable. Therefore, it is widely used as model drug and tracer in HME [15, 57, 71]. Further, its low tendency for chemical reactions and, thereby, incompatibilities as well as its water solubility are of great advantage. This allowed application of established methods in dissolution studies and minimized the risk of API degradation during the process. Theophylline exhibits polymorphism and pseudo-polymorphism. This means in particular that it appears as anhydrate, which has two polymorphic forms, form I and form II, and as monohydrate. Both, anhydrous theophylline and the monohydrate are officinal according to the European Pharmacopoeia (Ph. Eur.). Regarding the polymorphic forms I and II, it can be stated that form II is the thermodynamically stable form. Form I does not play any role in practice, since it is only formed at 270 °C in a hermetically sealed container and is quickly transformed into form II under standard conditions [72, 73]. Therefore, no difficulties regarding polymorphism had to be considered. To avoid incomplete transformations of the monohydrate into the anhydrate due to thermal load during extrusion, the anhydrate was chosen as model drug to work with. Reconciliation of wide dose range of 100 to 600 mg of theophylline per applied dosage form [74] and the small therapeutic range was considered feasible via 3D-printing. However, comparatively high doses demanded the production of highly drug-loaded filaments and was a problem to be solved in the present work.

Summarizing all these properties, theophylline appeared to be a suitable model drug for first feasibility studies about FDM™.

1.5. Selection of Excipients for Formulation Development of 3D-Printable Filaments

Since theophylline is mostly applied in sustained-release dosage forms and FDM™ might represent a novel technique for the on-site production of individualized sustained-release dosage forms, aPMMA as sustained-release polymer was chosen as main basis for formulation development of printable filaments. Its chemical structure is displayed in Figure 7.

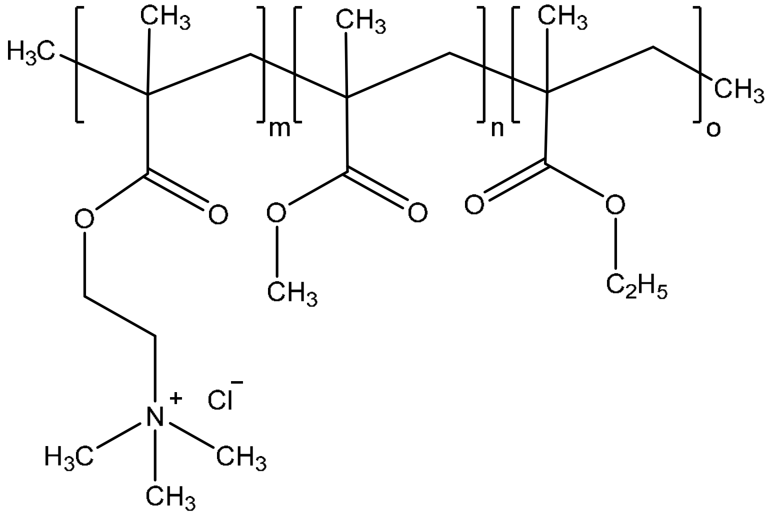

Figure 7. Chemical structure of aPMMA. Ratio of m:n:o is approximately 0.2:2:1.

aPMMA is described as ammonio methacrylate copolymer type A in the Ph. Eur. [75]. It is a copolymer and consists of three different monomers: 2-(trimethylammonio)ethyl [m], methyl 2-methylpropenoate [n] and ethyl propenoate [o]. The counterion for the positively charged nitrogen is chloride. aPMMA is practically insoluble in water and shows limited swelling, but no gel-forming or erosion [76]. Regarding pharmaceutical purposes, it is either used for film coatings [77, 78] or as hot-melt extruded matrix [15, 24]. Since in the present work HME as processing technology should be used, extrudability of the polymer and compatibility with the API under extreme temperature conditions were important to consider. Both factors have been widely explored in literature demonstrating joint processability of theophylline and aPMMA [15, 24].

Triethyl citrate and glyceryl triacetate are documented plasticizers for aPMMA [15, 79]. Both substances are in a liquid state at ambient conditions and exhibit, thereby, usually a higher vapour pressure than solids. This might involve higher tendency for evaporation during the HME process or from the finished extrudate over storage [80, 81]. Thereby, mechanical properties might be impeded and relative API content might change. Therefore, the focus should be on the evaluation of solid plasticizers in this work, although formulation development might be more complicated. In comparison to liquid plasticizers, the amount of solid plasticizer cannot be adapted flexibly during the HME process depending on the mechanical properties of the extrudate. An exception of this might be a process using split feeding of two solid components. This, however, was not applicable in the present case due to small throughputs and, therefore, very low amounts of polymer and plasticizer to be fed into the barrel. As solid plasticizers, stearic acid (SA) and macrogol 4000 (PEG4000) were chosen. Both have already been used to plasticize bPMMA during HME [80]. For this reason, they were assumed suitable for aPMMA, as well.

SA and corresponding derivatives are commonly used in the pharmaceutical field as lubricant in roller compaction or tableting [82, 83]. It belongs to the class of fatty acids. According to the Ph. Eur., it is lipophilic, practically insoluble in water and represents a mixture of stearic (C_{18}) and palmitic (C_{16}) acid (Figure 8) [84].

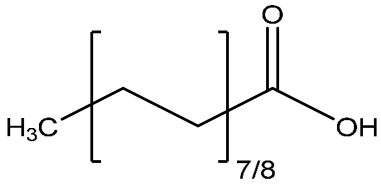

Figure 8. Chemical structure of stearic acid ($C_{16/18}$) according to the Ph. Eur. definition.

PEG4000 (Figure 9) was chosen as solid plasticizer with hydrophilic properties. It is a polyoxyethylene glycol with an average molecular weight of 3000 to 4800 g/mol. Due to its high amount of oxygen atoms, it is hydrophilic and classified as very soluble in water [85]. Hence, it is suitable as pore former in extruded lipid formulations [86]. In other pharmaceutical regards, PEG4000 is used as hydrophilic suppository or ointment base [87]. Due to great differences in hydrophobicity and expected impact on drug dissolution, both plasticizers were evaluated.

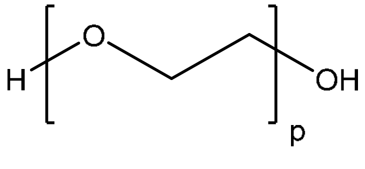

Figure 9. Chemical structure of PEG4000, with p ≈ 69.0 to 84.0.

For the evaluation of mechanical properties and corresponding thresholds, additional materials were used. As they did not fully comply with the set goals for the work regarding dissolution behaviour, studies mainly focused on aPMMA as polymer matrix.

1.6. Printed Networks as Novel Solid Dosage Form

For the present work, exploring of sustained-release matrices for FDM^{TM} seemed in particular worth investigating, since these might be used for compounding of sustained-release oral solid dosage forms or for implants. However, variation of dose using different sizes of the printed DDS, was shown to cause completely different release properties, since the surface/mass ratio dramatically changed (Figure 10) [15].

Figure 10. Printed sustained-release dosage forms of different doses and surface/mass ratios (adapted from [15], by courtesy of Elsevier).

The estimation of drug release is indispensable, for the production of sustained-release dosage forms in community or hospital pharmacies. Nevertheless, in-vitro testing of API release is usually not feasible on-site, as most pharmacies do not have the equipment and dosage forms would have to be produced several times. Hence, the motivation of the printing studies was to overcome mentioned problems and to develop a sustained-release DDS, which allows dose adaption and concurrent prediction of API release. This was expected to be achievable using a printed three-dimensional network system, completely exposed to the dissolution medium. The idea was to vary the dose by varying the density of this network. The size of the branches should be the same in all the cases. Thereby, the surface area of the DDS should increase equally if the dose is increased. This was expected to cause a constant surface/mass ratio and consequently enable easy and precise prediction of the dissolution behaviour. Ideally, pharmacies should be able to receive industrially produced filaments with corresponding information about release properties, in the future. Customized solid dosage forms might be printed and drug release could be estimated. Feasibility of dose adjustment using different printed fill densities has already been shown [37, 51]. These dosage forms, however, were closed by solid layers at the top and at the bottom. Consequently, branches of the network were not freely accessible for the dissolution medium. In other studies, networks without shell or only a partial shell were investigated. These did not offer any predictions of drug release behaviour based on dose variation via fill density [65, 88]. The present study about sustained-release network structures was further extended using a combination of two different filaments in one dosage form. Thereby, tailoring of drug release and prediction of biphasic dissolution profiles based on dosage forms containing only a single filament was investigated.

2. Aims and Outline

The present work focuses on HME and analysis of printable filaments and 3D-printing of novel, sustained-release dosage forms.

First, a systematic formulation development shall be performed. Anhydrous theophylline as API and aPMMA as sustained-release polymer serve as basis. In consideration of mechanical resilience and intended release properties, plasticizers of different hydrophobicity in different ratios shall be elaborated. A further aim is to develop a reasonable testing regime for the mechanical resilience of filaments. For the evaluation of printability, thresholds in the corresponding mechanical testing methods shall be defined.

After the development of a suitable formulation, the process of hot-melt filament extrusion has to be analysed in detail to investigate effects of the process parameters on critical quality attributes of the filaments. Homogeneity of drug distribution along the filament shall be examined to ensure homogeneous drug distribution in printed dosage forms. As important issue regarding filaments as intermediate products, stability over storage and ageing is important to be elaborated.

Subsequent to a detailed analysis of the extrusion process, the 3D-printing process has to be focused on, too. In this concern, the thermal stress shall be of particular importance, since heating the API twice, during HME and FDM^{TM}, might significantly influence the quality of the produced dosage form. An infrared (IR) camera shall be used to allow contactless temperature measurement of both, the print head and the heated build plate. In this context, an assessment of approximate residence times in the print head is indispensable.

The final goal of the present work shall be the development of a sustained-release novel solid dosage form, which enables flexible dose adjustment and predictable dissolution profiles. Via a combination of two different filaments in one printed dosage form, biphasic dissolution profiles, e.g. for loading and maintenance dose, shall be achieved and predicted based on data of dosage forms printed using only one filament.

3. Results and Discussion

3.1. Formulation Development of 3D-Printable Filaments

3.1.1. Pretext

Essential contents of this chapter are based on the previously published research article “Formulation Development and Process Analysis of Drug-loaded Filaments manufactured via Hot-Melt Extrusion for 3D-Printing of Medicines” (Pharm. Dev. Technol. 2018, DOI: 10.1080/10837450.2018.1433208) by Carolin Korte and Julian Quodbach. Texts have been linguistically adapted and the content was extended by further data.

3.1.2. Introduction and Objectives

The first aim of this work was the formulation development of drug-loaded 3D-printable filaments producible in a continuous HME process. For this, a suitable composition and an adequate production process had to be found. Further, a testing regime for the mechanical properties enabling discrimination between printable and non-printable filaments had to be developed.

The drug-loaded filament, and consequently the printed DDS, should ideally enable sustained drug release. This might be useful for orally administered dosage forms or drug-loaded implants. Further, also water-soluble polymers should be taken into account, e.g. for the production of water-soluble drug-free scaffold structures or as drug-loaded filament enabling the release of a loading dose in a combined dosage form with a biphasic drug release profile.

Production of drug-loaded filaments has already been performed by soaking commercially available non-pharma grade filaments in organic solutions of API [14, 46, 51]. Nonetheless, API-loads were usually < 2 %, excipients were not pharma grade and removal of organic solvents had to be ensured. Several studies using micro-conical twin-screw extruders were presented as well, with batch sizes of 5-7 g [15, 35, 55-58]. These processes are suitable for the first steps of formulation development, but not for production of filaments at larger scales. Further, they did not allow split feeding and exhibited limitations regarding the variability of process parameters. This, however, will be necessary to bring the advantages of individualized drug therapy via FDM^{TM} to the patients: API-loaded filaments should be produced in a continuous way at larger scales by the pharmaceutical manufacturer and could then be printed at hospital and community pharmacies. In 2017, first studies using continuous HME in an 11 mm 40 D extruder for filament production were published [64, 65]. These studies did not cover rational formulation development, which the present work aimed to analyse as well. During the present work, the scale was elevated to a 16 mm 40 D extruder.

Rational formulation development was predominantly performed considering mechanical resilience of filaments. For this, variation of API and plasticizer ratios were key points. Mechanical resilience has already been identified as crucial factor for the print feasibility of filaments [58, 64, 89]. The Young's modulus (YM) determined in a tensile test [47], the stress and the distance at break in a three-point bending (3PB) test [64] were solely not able to define certain threshold values to ensure printability. Therefore, part of this section was also to identify types of mechanical stress inside the print head and to develop a comprehensive mechanical testing regime for estimation of printability. Moreover, different drug loads and their influence on mechanical properties were evaluated to generate a formulation with as much theophylline as possible. Diameter and solid-state properties as other important quality attributes were also considered.

3.1.3. Production of Different Formulations via Hot-Melt Extrusion

16 different formulations, containing four different polymers, were evaluated during this work (Table 1). All batches were produced using a 16 mm 40 D twin-screw extruder. For all formulations 0.4 % (w/w) colloidal anhydrous silica was used as flow regulator to ensure proper powder transportation into the extruder barrel.

As sustained-release polymer aPMMA was chosen and investigated in several different formulations (F1-F13). Formulations containing aPMMA were varied regarding the amount and the type of plasticizer as well as the API-content and were, thereby, extensively analysed. Preliminary studies revealed that aPMMA was compatible with solid plasticizers. Consequently, only those were taken into account. Thereby problems that might be caused by liquid plasticizers, e.g. evaporation during the process and during storage due to higher vapour pressures in comparison to solid plasticizers [80, 90], were circumvented. SA and PEG4000 were selected as they have contrary properties regarding hydrophobicity and consequently might influence the API-release from the matrix.

Other formulations (F14-F16) were analysed to evaluate different polymers and to extend conclusions regarding the testing of mechanical properties. Formulations of high molecular hydroxypropyl cellulose (HPC) (MW = 850,000 g/mol) (F14) and polyvinyl alcohol (PVA) (F15) contained macrogol 300 (PEG300) as liquid plasticizer. PEG300 was used as plasticizer, since combination with HPC has already been shown feasible [91] and since PVA and PEG300 were expected compatible as they are both hydrophilic. The formulation of bPMMA contained SA (F16), which was already shown to exhibit plasticizing properties for bPMMA [80].

Table 1. Hot-melt twin-screw extruded formulations (mass ratio [%]).

formulation	aPMMA	PVA	HPC	bPMMA	plasticizer	anhydrous theophylline	colloidal anhydrous silica
F1	69.6	-	-	-	-	30	0.4
F2	92.6	-	-	-	SA 7	-	0.4
F3	82.6	-	-	-	SA 7	10	0.4
F4	66.1	-	-	-	SA 3.5	30	0.4
F5	62.6	-	-	-	SA 7	30	0.4
F6	55.6	-	-	-	SA 14	30	0.4
F7	48.6	-	-	-	SA 21	30	0.4
F8	42.6	-	-	-	SA 7	50	0.4
F9	64.6	-	-	-	PEG4000 5	30	0.4
F10	62.6	-	-	-	PEG4000 7	30	0.4
F11	59.4	-	-	-	PEG4000 10	30	0.4
F12	57.1	-	-	-	PEG4000 12.5	30	0.4
F13	54.6	-	-	-	PEG4000 15	30	0.4
F14	-	-	84.7	-	PEG300 5.5	9.4	0.4
F15	-	64.7	-	-	PEG300 7	27.9	0.4
F16	-	-	-	95.6	SA 4	-	0.4

Ratios of polymer, plasticizer and API were evaluated in preliminary studies applying a capillary rheometer used as piston extruder (Rosand RH2000, Malvern, UK). Starting points for the ratios of plasticizers were chosen according to literature dealing with HME of the particular polymer-plasticizer-combination. Due to the appearance of melt fracture and insufficient homogeneity caused by application of the piston extruder, these studies only gave first evidence of the mechanical resilience of the filament. Mechanical testing using a texture analyser and printing trials were exclusively performed with homogenous and smooth twin-screw extruded filaments (Table 1). For continuous twin-screw extrusion batch sizes were always ≥ 300 g.

Experimental setting of the filament extrusion process is displayed in Figure 11. Behind the extruder outlet the filament was cooled on a conveyor belt. This was also used to stretch the filament to the target diameter. Afterwards, the diameter of the filament was determined in-line prior to rolling it up in a bucket. The obtained filament was then used as feedstock for the printer without any further post-processing.

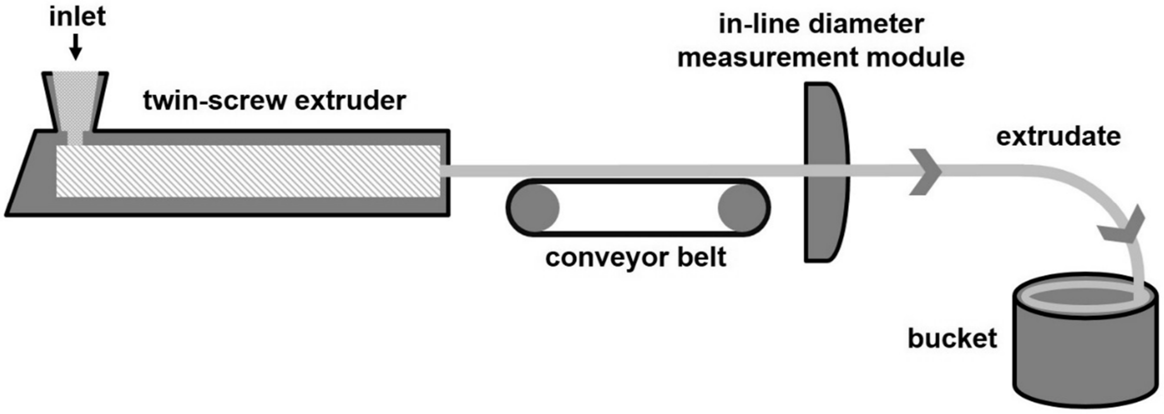

Figure 11. Experimental setup of filament extrusion process.

Different formulations required different experimental settings. Screw configuration, screw speed (RPM, 20 rpm), powder feed rate (PFR, 5 g/min) and die diameter (Ø = 1.75 mm) were the same in all cases. The applied screw configuration is exemplarily shown in Figure 12. At the powder inlet, it contained conveying elements with a higher pitch (3/2 L/D, section a in Figure 12) to ensure accurate powder entry into the barrel, even if flow properties of the powder were not optimal. Further, the screws contained two kneading zones of 2 D each. Barrel temperatures and the conveyor belt speed (CBS) were chosen individually for the formulations to achieve an extruded filament without melt fracture or surface irregularities.

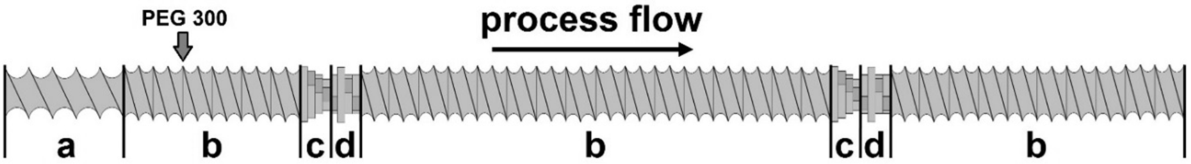

Figure 12. Screw configuration applied during HME: (a) 4 D conveying (helix of 3/2 L/D) – (b) 6 D conveying (helix of 1 L/D) – (c) 4 x kneading discs 30° (1 D) – (d) 4 x kneading discs 60° (1 D). The grey arrow indicates position of feed for liquid plasticizer PEG300 in case of formulations F14 and F15 (Adapted from [92] by courtesy of Taylor & Francis).

Since the formulations often contained high amounts of excipients, which were not molten at the applied temperatures, and since the screw configuration did not contain extensive kneading zones creating shear stress, the general rule recommending a process temperature of glass transition temperature plus 20-40 °C, did not fit [93]. Due to different temperatures and materials, also different CBS were required to produce filaments with suitable diameters for the printer. The particular settings are displayed in Table 2.

Table 2. Process parameters for HME of different formulations.

formulation	barrel temperatures from inlet to outlet [°C]	CBS [mm/s]
F1	40-100-170-175-175-180-180-180-180	31.52
F2, F5, F6, F8, F10	30-60-160-160-160-160-160-160-160	
F4	30-60-170-170-170-170-170-170-170	
F7	30-60-150-150-150-150-150-150-150	
F9	30-80-160-160-160-160-160-160-160	
F3	60-160-160-160-160-160-160-160-160	31.01
F11	30-60-145-145-145-145-145-145-145	31.52
F12		28.97
F13		29.14
F14	30-120-185-185-185-185-185-185-185	33.73
F15	30-120-195-195-195-195-195-195-195	30.5
F16	30-100-140-150-150-150-150-150-150	34.75

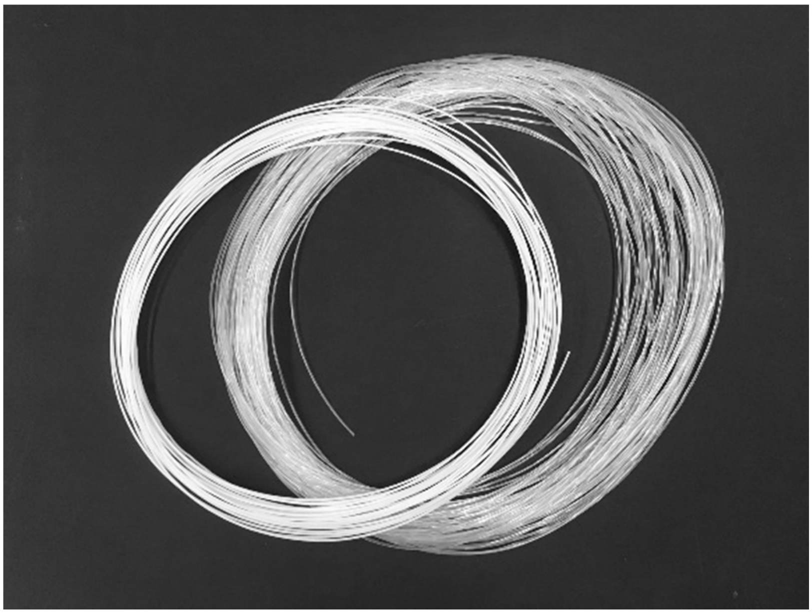

Figure 13. Rolled-up filaments of F5 (white, left) and F2 (transparent, right).

Extrudates were collected as long rolled-up strands, which were used as feedstock for the printer. Examples for obtained products are depicted in Figure 13.

3.1.4. Characterization of Filaments

3.1.4.1. Diameter

The diameter of filaments was considered as critical quality attribute, which decisively influences the printability. Usually, diameters of commercially produced filaments as drug-free printer feedstock are 1.75 mm to 3 mm depending on the specifications of the print head [14, 51, 56]. Print heads type I and type II used during the present work required a filament size of 1.75 mm predominantly determined by the inner diameter of the print head. This could not be exceeded, as a conveyance would have been impeded. Consequently, target diameters during formulation development were around or below 1.75 mm. Besides the absolute diameter, which decisively influences the processability of the filament, the consistency of the diameter was considered important [60]. During FDM^{TM}, the filament is continuously conducted through the print head. The mean diameter of filament is respected in the printer settings. If the filament exhibits irregularities, the speed of conveyance is not adjusted. A uniform conveyance thereby might lead to a non-uniform product. This might especially be important in case of low-dose DDS or printing of smaller objects. In other publications, relative standard deviations of 2.9 % to 18.6 % were tolerated [43, 59, 60]. Moreover, large differences in diameter over a filament length would also cause differences in mechanical resilience and, in the worst case, breakage at thinner parts of the filament during conveyance inside the print head.

Behind the extruder outlet, filaments were cooled on a conveyor belt and then fed through a measurement module enabling in-line diameter determination. Target diameters were achieved by adaption of the CBS and, thereby, varying the extent of stretching the filament. The measurement module recorded the diameter in three different directions at a frequency of 1 Hz. Three laser beams irradiated the sample in the measurement channel and a shadow was registered at sensors placed in opposite position. Diameter values were automatically calculated based on collected shadow information. If the filament did not pass horizontally the measurement module or a bend appeared, at least one of the values increased as an oval cross section was detected (Figure 14). Due to this and based on the assumption that the extrudates had an ideal-round cross section, always the smallest of the given values was used for data evaluation.

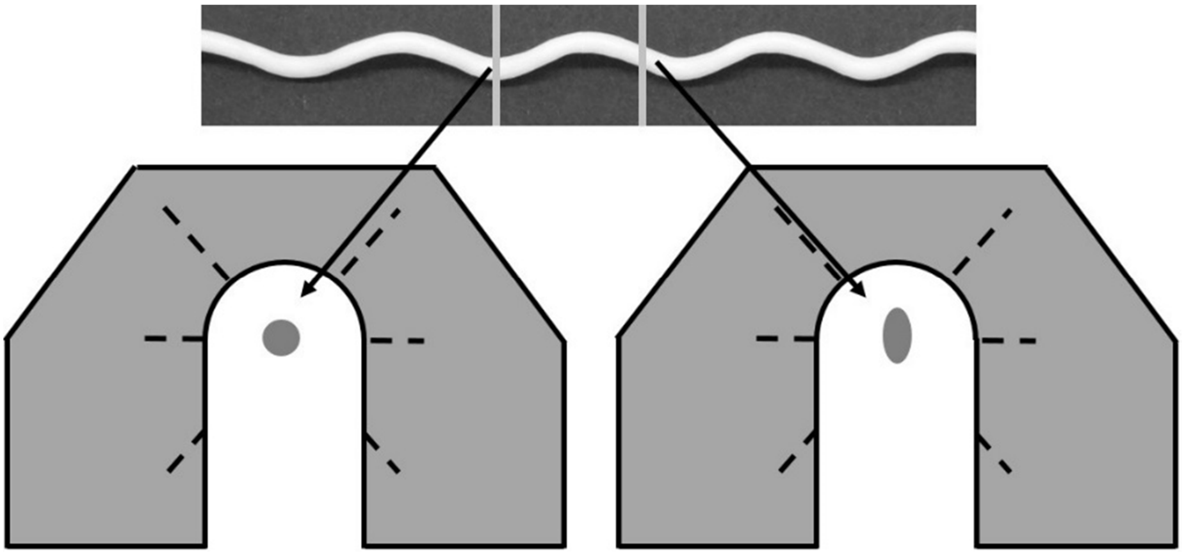

Figure 14. Diameter measurement module and detection of oval shapes. Dashed lines mark the three laser beam paths.

Figure 15 shows the material pressure at the die during extrusion and the in-line diameter data of the filament over time. The material pressure showed fluctuations, which were also reflected in the diameter data with a delay of ~20-30 s. This corresponded approximately to the time needed for the filament to pass the conveyor belt in this experiment. It was supposed that material accumulated in front of kneading zones and pulsatile conveyance occurred only if enough pressure was built up [94]. Thus, the amount of material reaching the die fluctuated and, thereby, the diameter. The fluctuations were not periodical as the screw configuration contained two kneading blocks. Therefore, different material accumulations and flows interfered with each other. Peaks of diameter values occurred in regular intervals of ~80 s (Figure 15, black rectangles). These resulted from manual movement of the filament to roll it up into the bucket. Movement caused increased values because the sample did not pass the measurement channel horizontally for a few seconds. These values were discarded for the determination of mean and standard deviation.

Figure 16 displays the diameters of the tested formulations. The range for target diameters was chosen between 1.6 and 1.75 mm for formulation development to avoid a large distortion of values for mechanical resilience solely due to the diameter. The number of diameter values used for the calculation varied between 246 (F14) and 2967 (F15) due to differences in sampling times.

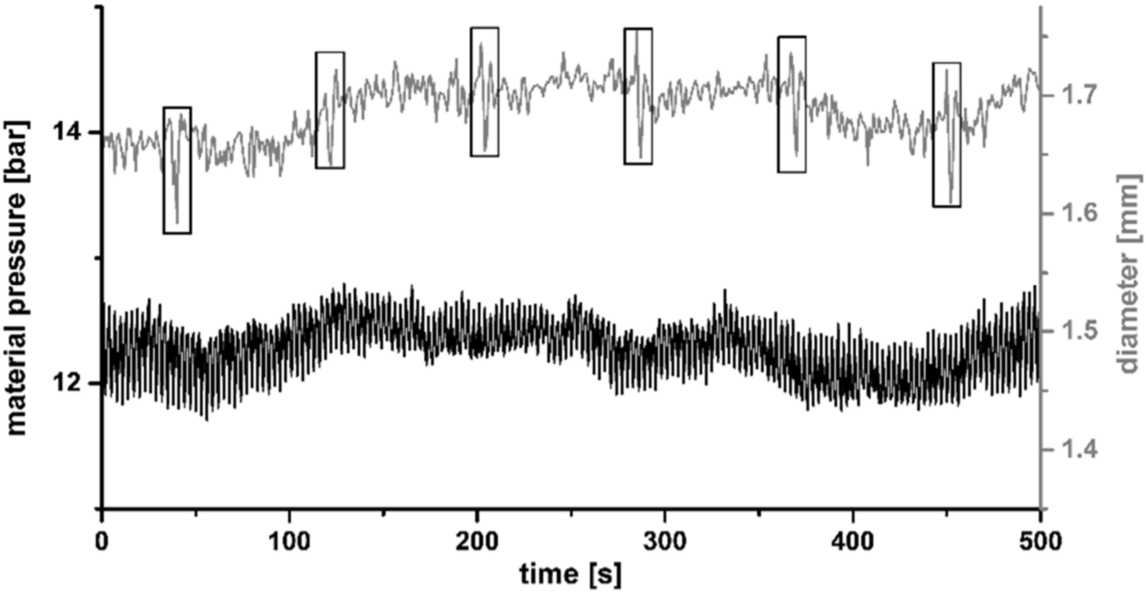

Figure 15. Material pressure at the die and diameter of the F5 filament over time (1 Hz). Peaks in diameter values are marked with a black rectangle.

Nevertheless, (relative) standard deviations were comparable as 246 values already represent a relatively high number of samples. Relative standard deviations were between 0.82 % (F13) and 4.99 % (F16) and thus in accordance with limits from literature or even better. The mean values met the target range of diameters in all cases but standard deviations of F2, F7, F14 and F16 exceeded the pre-set threshold values. This, however, was considered to have negligible influence on values for mechanical resilience and, thereby, comparability of the formulations.

F2 and F5, processed at identical conditions, contained aPMMA as polymer and SA as plasticizer. However, for F5 30 % of polymer was replaced by anhydrous theophylline. F5 exhibited a smaller diameter and a lower relative standard deviation in diameter (1.67mm, 2.27 %) compared to F2 (1.71 mm, 4.03 %). This phenomenon was explained by viscoelastic properties. The polymer was in a softened state at the extrusion temperature of 160 °C, whereas the API still was in a solid state ($T_{m,\text{Theophylline}}$ = 270 to 274 °C [95]). After being forced through the die, the polymer exhibited extrudate swell due to elastic recovery. Generally, it can be stated that the higher the shear stress at the die, the more pronounced is the die swell [61]. Due to observed material fluctuations (Figure 15), fluctuations in shear stress at the die and in the diameter were generated. Thus, increasing the portion of viscoelastic polymer resulted in a more distinct elastic recovery. This tendency was also underlined considering F8, which contained aPMMA, 7 % SA and 50 % anhydrous theophylline. In this case, production conditions were the same as for F2 and F5 and an even lower relative standard deviation resulted (2.06 %). The diameter of F3, containing aPMMA, 7 % SA and 10 % anhydrous theophylline, was not comparable to these formulations, because different extrusion settings and CBS were used (Table 2). F16, containing bPMMA as polymer and SA as plasticizer, exhibited the highest relative standard deviation among all formulations. As one reason pronounced elastic recovery due to absence of API was identified. Further, bPMMA was rather cohesive and, therefore, difficult to feed accurately into the extruder. This might have caused inaccuracies in diameter. Generally, it was concluded that higher amounts of API were beneficial for the production of filaments with high uniformity in diameter. To achieve even higher uniformity, the screw configuration might be changed. Due to accumulation of material in front of the kneading zones and thereby created material fluctuations, usage of one kneading zone instead of two or shorter kneading zones could be examined. This approach, however, might not be suitable for using liquid plasticizers, since these have to be kneaded into melt. Calculations regarding the influence of the diameter on the resulting printed dose are exemplarily shown in section 3.2.3.2 for one of the final formulations (F5).

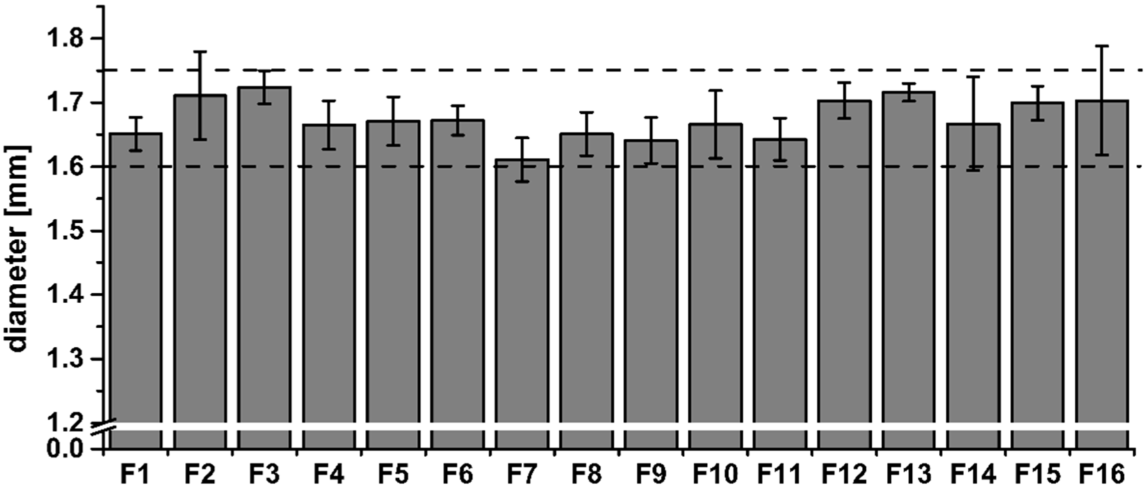

Figure 16. Diameters of the different formulations (mean ± sd; n ≥ 246). The dashed lines mark the aspired thresholds for the mean diameter of the filaments during formulation development.

3.1.4.2. Mechanical Resilience and Printability

In literature, the term printability in the field of 3D-printing is not generally defined. For this work, printability of a filament was defined as property of an extrudate to print the dosage form displayed in Figure 46 (left, section 3.4.3.1) in the applied FDM^{TM} printer without interruption. Figure 17 shows a schematic sketch of the two different print heads used during this work. The working principle is similar in both cases. The print heads contain a heating element connected to a metal tube, which is called hot end. Via heat conduction, the hot end is entirely heated. The filament is transported through the hot end and fused through a tip at its end. Filament transport was done via two counter-rotating gears in case of print heads type I and via two conveyor belts in case of print heads type II. The filament transport causes certain mechanical stress on the filament. Hence, besides the diameter and its uniformity, the mechanical resilience plays a decisive role for the printability of an extrudate [35, 50]. Printable extrudates have to resist certain types of mechanical stress during the printing process. On the one hand, filaments undergo compression in longitudinal direction between the motor driven gears and the tip (Figure 17, left). They should be rigid to avoid breakage due to high brittleness and curling of the filament due to high flexibility. On the other hand, there is punctual mechanical stress in axial direction when the filament passes the gears. The filaments should show neither breakage nor plastic deformation inside the print head. During this work, only print heads type I were considered for the evaluation of printability, as the replacement of print heads type I by print heads type II took place only a few months before the practical work was completed. But both print heads were used in printing studies presented in section 3.4. Since punctual stress in axial direction often resulted in difficulties, the new print heads type II were designed in cooperation with the Technical University in Cologne. Punctual stress in axial direction should be minimized by using two conveyor belts for promoting the filament (Figure 17, right). Two counter-rotating V-ripped belts, which were clean on the surface used for conveyance, were supported by several gears to avoid punctual pressure on the filament. However, whether this was a successful mean to circumvent this problem was not analysed in this work. Using print heads type II for the experiments presented in section 3.4.4, printability of the applied filament was estimated only empirically.

Other working groups used print heads with a large distance between the gears and the tip, so that several centimetres of a self-extruded filament were put in this section and were then promoted by a commercial polylactic acid (PLA) filament. This was able to withstand the axial stress applied by the gears and filament breakage was avoided [38, 96]. However, distance between the gears and the tip strongly limited the amount of printable material impeding continuous production.

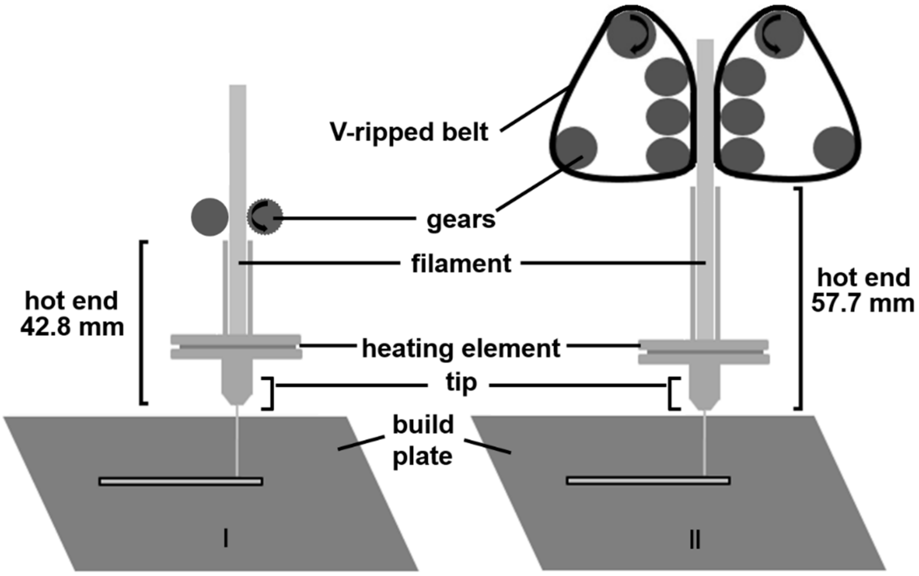

Figure 17. Print heads type I and type II. Motor driven gears are marked with black arrows.

During printability examination of the extruded formulations using print head type I, different problems occurred. Examples for inappropriate conveyance inside the print head are shown in Figure 18. The high flexibility of F14 led to curling up of the filament in small gaps at the print head, i.e. between the gears and the hot end (Figure 18, left). The distinct brittle behaviour of F8 caused breakage of the filament due to punctual axial stress between the two conduction gears (Figure 18, right). These observations emphasized the need for a testing regime for the mechanical resilience of filaments to evaluate printability in advance. Inappropriate conveyance of filaments can lead to print interruption, nozzle clogging or other severe malfunctions of the printer.

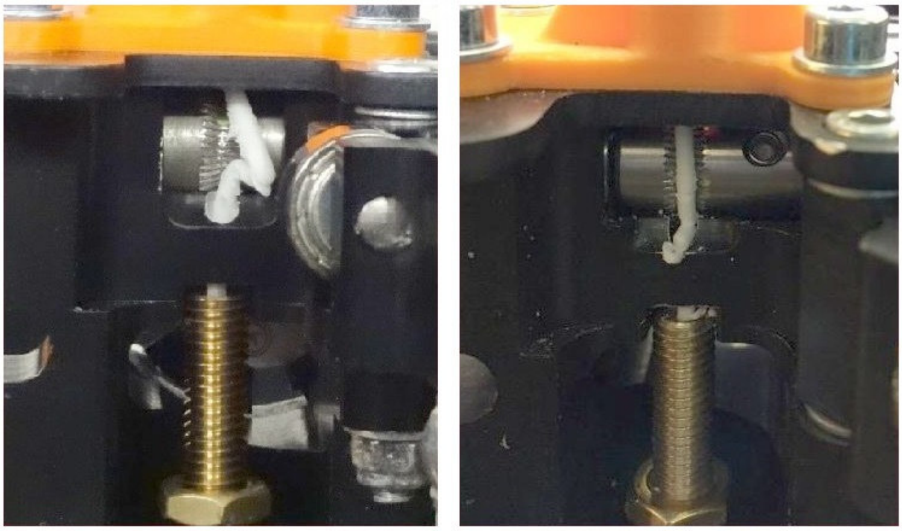

Figure 18. Unclosed print head showing non-printable filaments. Left one (F14) was not printable due to lack of stiffness, whereas the right one (F8) exhibited brittle behaviour (adopted from [92] by courtesy of Taylor & Francis).

It is widely known that material characteristics, e.g. YM or tensile strength, depend on the testing direction [97]. In case of extrudates, this might be explained by arrangement of polymer chains in longitudinal direction due to shear stress, especially occurring at the die [98, 99]. Regarding 3D-printable filaments, both testing directions have been explored. In previous publications the YM in a the tension test [47] and the distance and stress at break in a the 3PB test [64] were determined. Gioumouxouzis et al. tested the micro-hardness of the filaments [89]. However, studies always applied only one of the mechanical tests and none of the tests was solely able to discriminate between printable and non-printable filaments.

Based on the described types of mechanical stress applied during the printing process, the YM in a compression test and the distance at break in a 3PB test, representing axial punctual stress, were considered most descriptive. ISO 604 states that in a compression test of plastics, representative values for YM are only obtained, if Euler buckling of the test specimen does not occur [97, 100]. Therefore, length of the test specimen depends on its diameter. For a filament of d = 1.75 mm, this would be between 2.63 and 4.38 mm. During fixation of the filaments slight changes in the distance between the clamps can occur. In addition, the calculated test lengths were considered rather small and hardly reproducible. Hence, during the present work, the tensile test was chosen to determine the YM (section 5.5.5.3). So the direction of mechanical stress could be considered and inaccuracies caused by the test method were minimized. YM results were combined with obtained values for the distance at break in a 3PB test (section 5.5.5.4). Approaches, which produced a completely new test specimen out of filament, e.g. by 3D-printing or compression [88], were rejected due to strong dependency of mechanical properties on geometry of the test specimen [97]. Furthermore, the feasibility of production of a test specimen via 3D-printing would make a prediction on printability redundant.

Extruded formulations were subjected to the described test regime. Testing conditions were adopted from Zhang et al. and DIN EN ISO 527-1 [64, 101]. Typical curves obtained during mechanical testing are exemplarily displayed for F10 in Figure 19. For the tensile test, a stress-strain-curve is shown. The YM was determined as slope between 0.05 and 0.25 % strain in this graph. For F10, plastic deformation was observed before breakage occurred (Figure 19, left). Plastic deformation was indicated by deviation of the curve from a linear slope at higher strains. Not all formulations showed plastic deformations and consequently exhibited brittle fracture after the elastic deformation. At lower strains (< 0.25 %), however, all curves were linear and, therefore, suitable for YM calculation. For the 3PB test, however, a force-distance-curve is depicted, from which the distance at break could directly be determined as distance, at which the maximum force was recorded. In the 3PB test, F10 filament also exhibited plastic deformation, revealed by a shoulder at the beginning of the curve (Figure 19, right).

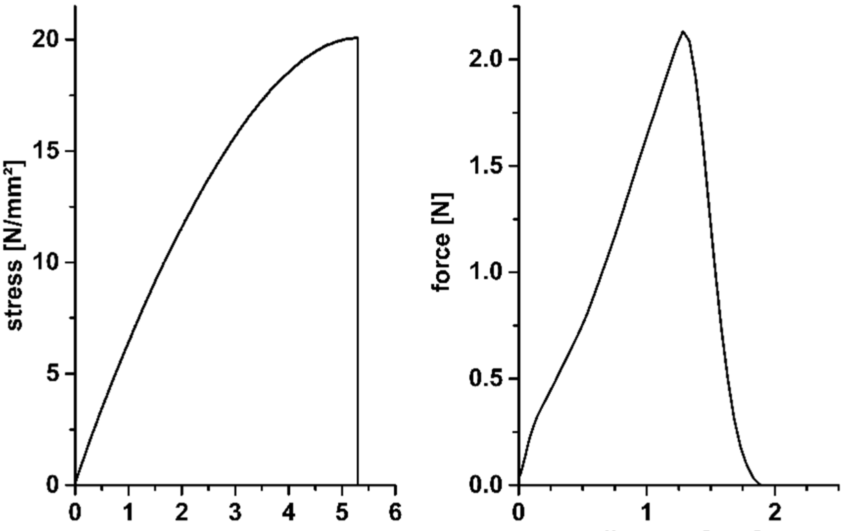

Figure 19. Mechanical testing of formulations F1 and F10.

Formulations containing aPMMA were extensively investigated as the polymer promised to enable the desired sustained API release. Changes in mechanical properties should be determined depending on the excipients to find the optimal formulation to work with. Results of mechanical tests are presented in Figure 20. Most samples exhibited small confidence intervals (CI), emphasizing the suitability of the testing methods and the uniformity of filaments. F1 contained only aPMMA and 30 % anhydrous theophylline. The filaments were stiff, expressed by a YM of 786 N/mm², but also brittle with a distance at break of only 0.75 mm. F4 to F7 contained aPMMA and 30 % anhydrous theophylline, but also increasing portions of SA (3.5, 7, 14 and 21 %). Due to the plasticizing properties of SA, F4 and F5 exhibited a higher distance at break and a decreased YM compared to F1. However, higher portions of SA (>7 %) decreased the distance at break. This was explained by defects in the matrix due to dispersed SA. These defects were expected to occur above the solubility concentration of an excipient in the matrix, as the plasticizer crystallized aside the polymer. Values for YM were hardly affected. Comparing F2, F3, F5 and F8 (aPMMA, 7 % SA and 0, 10, 30 or 50 % theophylline) revealed a decreased distance at break for an increased API amount. Although YM of F3 was slightly below the one of F2 (591 vs. 539 N/mm²), general tendency of higher YM for increased API content could be detected. This effect might not be observed during the escalation of SA amount, as relative amounts were much lower than in case of theophylline.

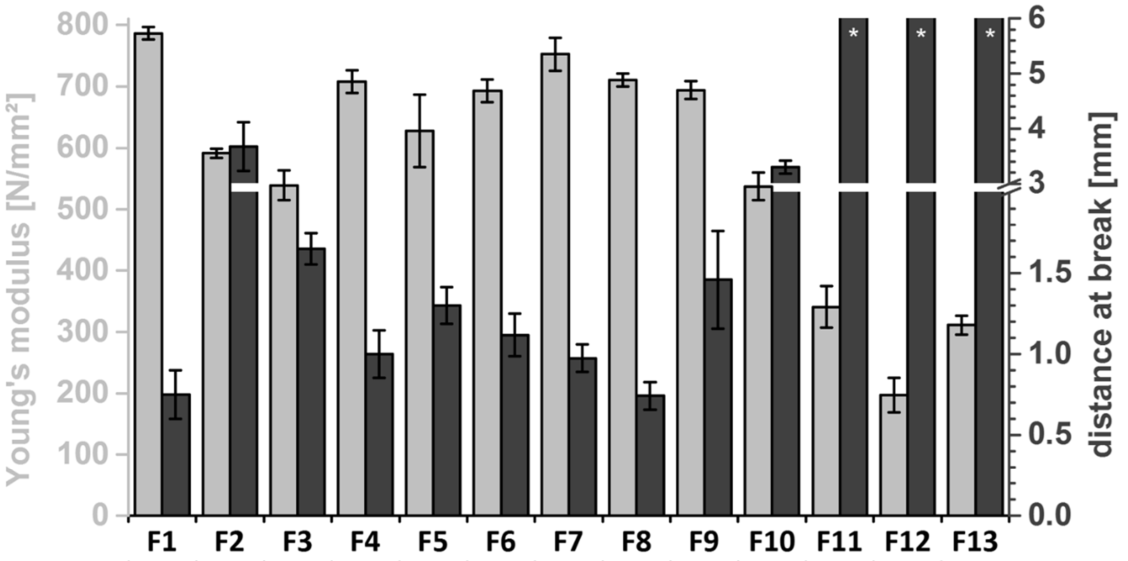

	F1	F2	F3	F4	F5	F6	F7	F8	F9	F10	F11	F12	F13
SA [%]	-	7	7	3.5	7	14	21	7	-	-	-	-	-
PEG4000 [%]	-	-	-	-	-	-	-	-	5	7	10	12.5	15
theophylline [%]	30	-	10	30	30	30	30	50	30	30	30	30	30

Figure 20. Mechanical properties of aPMMA containing formulations. YM was determined in a tensile test, distance at break in a 3PB test (both tests: n = 6, mean ± CI). Table below indicates ratios of plasticizers and API. * indicate that no breakage was detected under the applied test conditions.

F9 to F13 consisted of aPMMA, 30 % anhydrous theophylline and increasing amounts of PEG4000 (5, 7, 10, 12.5 and 15 %). In this case, adding of PEG4000 (F1 vs. F9) also decreased the YM and increased the distance at break, underlining its plasticizing properties. The distance at break increased from 1.5 mm for F9 (5 % PEG4000) to 3.3 mm for F10. F11, F12 and F13 did not show any breakage at all during the test. For F13 the YM was increased compared to F12, probably because the solubility was exceeded by increasing the PEG4000 amount from 12.5 to 15 %. The distance at break was not detectable. Using SA and PEG4000 as plasticizers changed the filament properties decisively. At the same concentrations in a filament, e.g. F5 and F10, YM was lower and the distance at break was higher for the formulation containing PEG4000. PEG4000 was also applicable in higher concentrations and led to further plasticizing until 12.5 %, whereas the limit regarding the plasticizing ability for SA was 7 %. Hence, inside the aPMMA matrix, a higher plasticizing ability for PEG4000 than for SA was concluded.

Results showed that excipients or API were able to increase flexibility, expressed as distance at break, to a certain extent. But, as plasticizing effects are usually observed below the solubility of the excipient inside the matrix, addition of more material, which is then dispersed inside the matrix, might level out these effects by creating predetermined breaking points. Results showed as well, that YM and distance at break could not be changed independently.

For formulation development, changes of filament properties in case of varying ratios of excipients are important. However, the link between the mechanical properties and the processability by the 3D-printer was of major interest for the present work. All formulations enabling printing of a dosage form as specified at the beginning of this section were considered printable. Mechanical properties of selected formulations and their printability are presented in Figure 21. Formulations F1, F4 and F8 were too brittle for being printed and behaved similar to the filament shown in Figure 18, right. They contained either too little plasticizer (F1, F4) or too much API (F8). Formulation F14, however, was too flexible for being processed. Failure inside the print head was already shown in Figure 18, left. F14 was used as negative reference for a too small YM and a high distance at break, since these properties could not be found in any of the extruded aPMMA formulations. Formulations F3, F5, F9, F10, F11, F15 and F16 exhibited suitable mechanical properties for the printing. Five of these mixtures contained aPMMA, one bPMMA and one PVA as polymer. Based on the 12 formulations, thresholds of 300 N/mm² for the YM and 1.125 mm for the distance at break were found suitable for print heads type I. Of course, these values are not universally valid and have to be determined individually for every type of print head. Mechanical resilience of filaments certainly depends on the filament diameter. The mechanical stress inside the print head caused by the conveyance of a filament is identical, irrespectively of the filament diameter. Therefore, it was suitable to set an absolute threshold value for the distance at break, which is independent from the diameter. Although the YM represents a value dependent on the diameter, it was applicable since the diameter range for formulation development was small (1.6 to 1.75 mm) and big distortions of the YM by the diameter were not expected. Suitable testing regimes for mechanical properties are also likely to be dependent on the conveying mechanism of the print head. This applies equally for print heads type II, which contained a conveyor belt based feeding system instead of a gear-driven one. Print heads type II were not considered during formulation development of filaments since they were implemented later. Nevertheless, printability of F5 was also given in case of using it in print heads type II. This was important to ensure proper processing for printing studies in section 3.4.4.

Since the YM and the distance at break cannot be modified individually, it is likely that certain polymer/excipient or polymer/API combinations and ratios are not suitable to generate 3D-printable filaments. The applied testing regime, consisting of determination of YM in a tensile test and distance at break in a 3PB test was shown to be appropriate for defining printability of filaments in advance. Further, it was feasible to identify flexible filaments as printable, although they did not exhibit breakage in a 3PB test, e.g. F11. This would not have been feasible with methods presented in literature, as these needed breakage of the filament as endpoint for data evaluation [64].

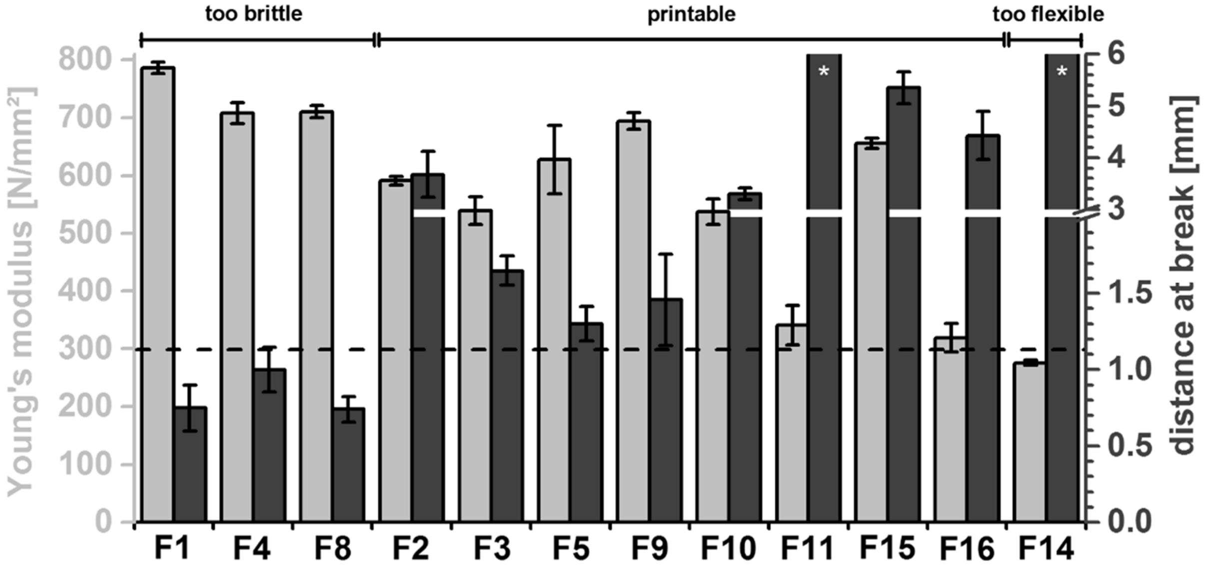

Figure 21. Selected formulations and their mechanical properties. Dashed line marks the threshold for the print feasibility. YM was determined in a tensile test, distance at break in a 3PB test (Both tests: n = 6, mean ± CI; for F14: n = 3, mean ± sd) (Adapted and extended figure [92], by courtesy of Taylor & Francis) * indicate that no breakage was detected under the applied test conditions.

Mechanical resilience of filaments was examined as critical quality attribute for 3D-printable filaments to ensure adequate printing. The identification of different printable formulations with aPMMA as a sustained-release polymer was successfully performed. Two other polymers, bPMMA and PVA, were found suitable to produce printable filaments. However, further analyses focused on aPMMA-formulations due to the sustained-release character of the polymer.

To sum up the formulation development of 3D-printable filaments, Figure 22 schematically illustrates the general procedure elaborated during the present work according to DIN (Deutsches Institut für Normung) 66001 [102]. At the beginning, a suitable polymer has to be chosen. Important criteria in this regard are a suitable extrusion temperature for the API and the expected release properties, for forming a matrix in which the API is embedded. However, release behaviour of the printed dosage form is decisively influenced by numerous other factors, i.e. the solubility of the API in the dissolution medium and the polymer matrix, the amount and type of other excipients such as plasticizers and the design of the printed object. For the API, maximum processing temperature avoiding thermal degradation and suitable target concentration in the extrudate have to be determined. After that, preliminary studies using a ram extruder can be performed. This allows a rough estimation, whether API and polymer are compatible or whether and to what extent the API acts as plasticizer for the polymer. These filaments cannot be examined using a texture analyser, since results would be unreliable due to diameter and surface irregularities the filaments produced in a ram extruder usually exhibit. Therefore, first examination is solely organoleptic. If the stiffness in longitudinal direction appears insufficient, increase of API amount might help to solve this problem, since the API can act as structure-giving substance. In case of sufficient stiffness, brittleness in axial direction should be focused on. If this also appears to be good, the mixture can be processed via twin-screw hot-melt extrusion and can subsequently be analysed using a texture analyser. If the preliminary filament appears quite brittle, remedial measure might be the addition of plasticizer. Selection of plasticizer should also be done carefully taking physico-chemical properties into account. On the one hand, the plasticizer must have a certain affinity to the polymer to be embedded between the polymer chains and, thereby, evolve its plasticizing ability. On the other hand, the plasticizer might accelerate or slow down the release of API from the matrix. Different amounts of plasticizer can be added to the formulation. After extrusion via a twin-screw hot-melt extruder, the mechanical resilience can be evaluated. If thresholds for YM and distance at break are exceeded, filaments are printable and can be used for the production of dosage forms, which are then subjected to dissolution analysis. If the mechanical resilience is still not sufficient, different amounts of plasticizer or different types shall be evaluated. If an undesired dissolution profile results the plasticizer might be exchanged or the API-polymer-ratio might be adapted. Further, a modification of the printed structure can be taken into account. One of these options should be chosen based on the requirements the dosage form should fulfil.

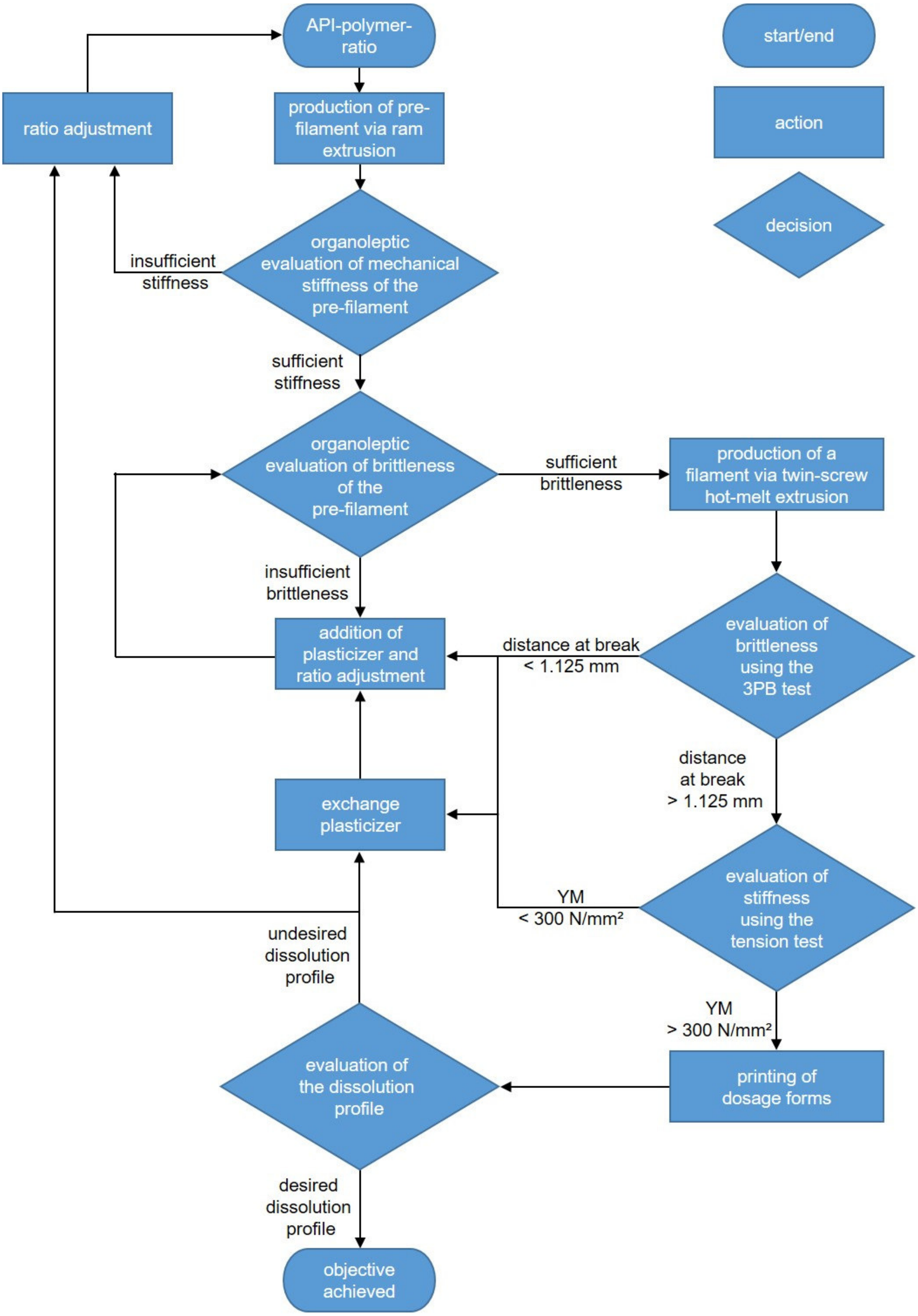

Figure 22. Flow chart for formulation development of printable filaments.

3.1.4.3. Solid-State Properties

Since the common technique for the production of API-loaded filaments is HME, thermal stability of API, excipients and polymer at processing temperatures is essential. Therefore, differential scanning calorimetry (DSC) analyses of raw materials were conducted, as well as of extruded formulations to ensure absence of degradation during the HME process.

Raw materials were always heated twice to mimic the extrusion process and to ensure absence of water, which could cause distortion of measured values [103]. Thus, solely data of the second heating cycle was evaluated. Extrudates, however, were heated once, as they were measured shortly after extrusion. None of the formulations or excipients exhibited thermal decomposition below 180 °C. Figure 23 displays thermograms of selected excipients and formulations. Besides thermal stability, for anhydrous theophylline, SA and PEG4000 melting peaks were found due to their crystalline character ($T_{m,Theophylline}$ = 270 °C; $T_{m,SA}$ = 61 °C; $T_{m,PEG4000}$ = 57 °C, Figure 23 a and b). aPMMA, on the other hand, showed a glass transition temperature around 68 °C as it is in an amorphous state (Figure 23 c). The amorphous state of aPMMA has also been described in literature based on results of X-ray powder diffraction [104]. At temperatures above ~ 180 °C degradation was observed.

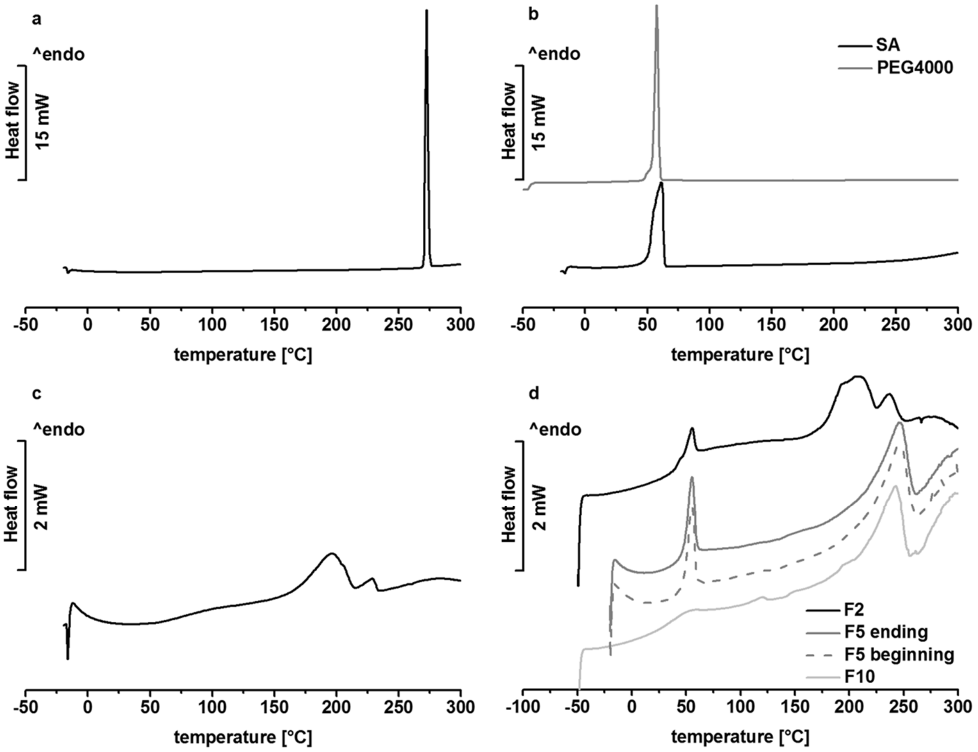

Figure 23. DSC thermograms of anhydrous theophylline (a), plasticizers SA and PEG4000 (b), aPMMA (c), and extrudates of formulations F2, F5 and F10 (d). F5 extrudates were measured at the beginning and at the ending of the sample. (Adapted and extended figure [92], by courtesy of Taylor & Francis)

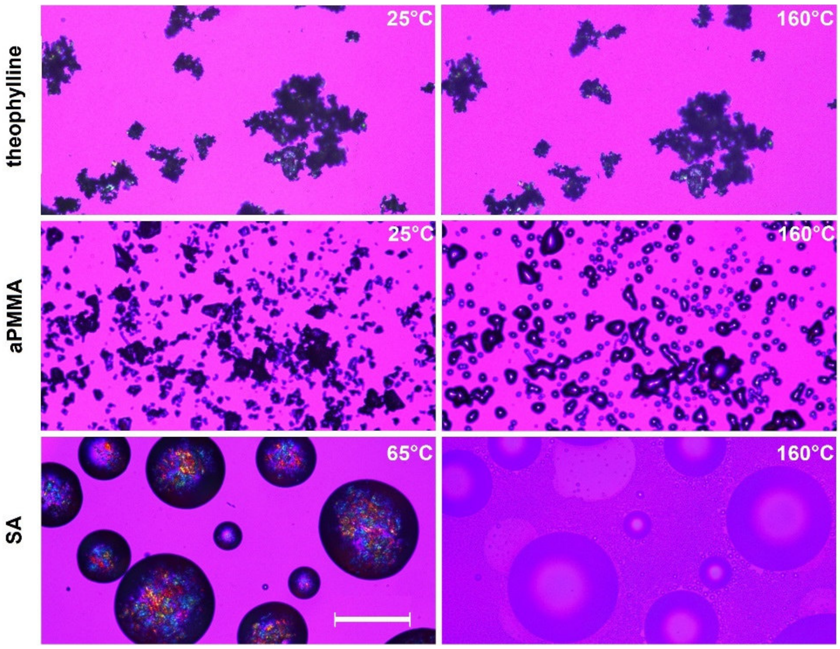

Figure 24. Polarized light microscope pictures of theophylline, aPMMA and SA. Temperature condition is indicated for each picture (scale bar: 250 µm).

Pictures of theophylline and SA (Figure 24) obtained in a hot-stage microscope using polarized light also underlined their crystalline character. Coloured structures indicate crystallinity, due to a change of the direction of polarizing light and, thereby, incomplete blocking of the light between the two perpendicularly orientated polarizer filters. At 160 °C, which was equal to the extrusion temperature, SA was molten whereas theophylline did not exhibit any obvious changes and remained crystalline. Regarding aPMMA, the amorphous character was underlined because it appeared dark in polarized light (Figure 24).

DSC thermograms of formulations F2, F5 and F10 are shown in Figure 23 d. F2 (API-free, 7 % SA) and F5 (30 % theophylline, 7 % SA) exhibited glass transitions of 36 and 41 °C, respectively. A decreased glass transition temperature in comparison to pure aPMMA underlined plasticizing properties of SA. The effect might be explained using the free volume theory [80, 105]. Plasticizers were embedded between the polymer chains. Therefore, the free volume of the polymer increased and, consequently, the chains' mobility. Thereby the glass transition temperature decreased. In thermograms, glass transition of the polymer and melting peak of dispersed SA were not clearly separated, indicated by an endothermic overshoot between 50 and 60 °C [106]. F10, not containing SA but the same amount of PEG4000, had a glass transition of 26 °C without any melting peak of PEG4000 or endothermic overshoot. It was concluded, that 7 % PEG4000 could completely be dissolved in the matrix and had a higher plasticizing potency than SA. Thermal instability of aPMMA at temperatures above 180 °C was found for the raw material and all aPMMA-containing formulations. Regarding F5, between samples of the beginning and of the ending of the extrudate, the DSC did not reveal any differences. This gave a first indication of a homogeneous consistency of the filament over process time.

For F16, the only formulation containing bPMMA as polymer, an interesting phenomenon was observed. Although mechanical properties, YM and distance at break, were tested to be sufficient for printing (Figure 21), at higher ambient temperatures (> 22 °C) and higher printing speeds, plastic deformation as shown in Figure 25 occurred. Mechanical failure seemed to be caused by softening of the filament and consequently forming of a bulge, which inhibited conveyance through the hot end. As this phenomenon preferably appeared at higher ambient temperatures and higher printing speeds, it was supposed that frictional heat due to the conveying gears in combination with the elevated ambient temperature was responsible for this behaviour.

Figure 25. Unclosed print head with F16 filament showing plastic deformation due to frictional heat.

F16 filaments exhibited a glass transition temperature of 19 °C. At room temperature, they were in a viscous or rubber state, favouring plastic deformation as seen in Figure 25. F11 and F12, showed a glass transition temperature of ~4.5 °C, but did not show such deformation. However, in contrast to API-free F16, F11 and F12 contained 30 % anhydrous theophylline. At room temperature, this was in a solid state giving structure to the filament and impeding plastic deformation. Similar phenomena have already been described for bPMMA [50]. Sadia et al. aimed to optimize bPMMA containing formulations by adding non-melting fillers, as e.g. 20 to 50 % tribasic calcium phosphate and microcrystalline cellulose. Nevertheless, a ratio of 20 to 50 % filler is likely to influence strongly the dissolution profile and makes a high drug load impossible. Therefore, if high API-loads were required, using the API as structure-giving non-melting filler would be preferred, like in case of F11 and F12.

3.1.5. Summary

The present section showed that formulation development and continuous production of 3D-printable filaments was successfully performed applying a 16 mm 40 D twin-screw extruder. Besides aPMMA as sustained-release polymer, bPMMA and PVA as water-soluble polymers were identified as suitable for the production of filaments, which could be processed in an FDM^{TM}-3D-printer. Tested HPC formulation (F14) was not printable and only served as negative reference for the evaluation of a testing regime of mechanical properties. API-loads up to 30 % resulted in printable filaments using aPMMA as polymer. Consistency of the diameter was given with a relative standard deviation below 5 %. Further, a testing regime concerning mechanical resilience of the filaments was developed to estimate printability. A combination of the distance at break in a 3PB test and the YM in a tensile test turned out to give reliable information in this regard. For all formulations, thermal stability during processing was identified using DSC. With respect to the API-load, studies revealed that increasing API ratio led to a higher YM, a lower distance at break, a higher diameter consistency and a more reliable conveyance inside the print head due to structure-giving properties. However, increasing the API ratio could be done only until a certain threshold, since brittle behaviour and therefore probability for breakage inside the print head increased. In this study, drug loads of 30 % in aPMMA filaments resulted optimal.

In this work, sustained-release individualized solid dosage forms were in the focus. Therefore, F5 and F10, based on aPMMA, were analysed further. They had a high drug load and contained solid plasticizers minimizing the risk of evaporation or insufficient mixing during the process compared with liquid plasticizers. Printability was given and diameter consistency was good with a relative standard deviation < 2.3 %. Both formulations were examined in detail, as the included plasticizers, SA (F5) or PEG4000 (F10), exhibit strong differences regarding their polarity and water solubility. This was likely to influence the dissolution profiles and was discussed thoroughly in section 3.4.

3.2. Production and Analysis of 3D-Printable Filaments Containing Theophylline

3.2.1. Pretext

Contents of this chapter are based on the previously published research article “Formulation Development and Process Analysis of Drug-loaded Filaments manufactured via Hot-Melt Extrusion for 3D-Printing of Medicines” (Pharm. Dev. Technol. 2018, DOI: 10.1080/10837450.2018.1433208). Texts have been linguistically adapted and the content was considerably extended by further data.

3.2.2. Introduction and Objectives

The most promising formulation analysed during the present work was F5, containing aPMMA, 30 % anhydrous theophylline and 7 % SA. The drug load was suitable to achieve therapeutic doses, printability for print heads type I and type II was given, diameter was consistent and the matrix was based on a sustained-release polymer. Preliminary studies indicated that SA, classified as insoluble in water [84], was able to delay the drug release compared to PEG4000, classified as very soluble in water [85]. Therefore, F5 was selected for thorough analysis in the following chapter.

Firstly, the continuous HME process of the chosen formulation should be analysed. For this, a full factorial design of experiments (DoE) was applied analysing the impact of process parameters (PFR, RPM, CBS, extrusion temperature (TEMP)) on critical quality attributes of 3D-printable filaments. Critical quality attributes were predefined in section 3.1 and were in particular, the diameter and the mechanical resilience. Further, the median residence time (MRT) of the raw material inside the extruder barrel was determined using the same process parameters, which were applied for production of filaments used for printing described in section 3.4. This should provide deeper insight into the process and help to estimate thermal stress applied during HME of F5.

Secondly, drug content and distribution were analysed. To obtain a uniform drug distribution in a printed dosage form, a homogeneous drug distribution along the filament and thermal stability of the API were considered of great importance. In addition, probable segregation of powder components inside the feed hopper was examined.

Due to perceived ageing accompanied by deterioration of mechanical properties, changes of physico-chemical properties during storage were studied. Curing was tested as probable method to improve the filament properties.

3.2.3. Process of Hot-Melt Filament Extrusion

3.2.3.1. Effects of Process Parameters on Quality Attributes of Filaments

One goal of the present work was to pave the way for closing gaps between pharmaceutical industry, as possible manufacturer of filaments as printer feedstock, and hospital and community pharmacies, which might use the filaments for DDS production. For this, continuous HME was preferred as production technique of 3D-printable filaments. HME and combination with the conveyor belt is a complicated production process and requirements regarding quality attributes for filaments are high. Thus, there was a need to analyse the HME process systematically. This was done using a DoE. As yield variables, the diameter, the mechanical strength and the API content of the extrudate were chosen. As factors, possibly influencing these parameters, PFR, RPM, CBS and temperature were taken into account. Applied settings are displayed in Table 3 and Table 14. They were chosen based on preliminary studies, which aimed to allow a rough estimation of the design space. The experimental space was chosen large considering that RPM and PRF were doubled from level -1 to level 1.

The testing regime for the mechanical resilience was reduced and deviated from section 3.1.4.2. The slope in a force-elongation-curve (modified YM, E_{mod} in N) determined in a tensile teste was defined as surrogate (0.05 to 0.25 % elongation). In this study, the YM was not considered representative because it is determined in a stress-elongation-curve. The stress is calculated using the cross-sectional area of the filament. The YM is thereby influenced by the diameter and is not able to display mechanical strength independently from the diameter. However, a big range of diameters was covered in these experiments (~1.1 to ~1.9 mm), which was considered likely to distort YM values stronger than during formulation development with a diameter range of 1.6 to 1.75 mm. Since only mechanical strength among the samples should be compared, a 3PB test was not conducted. Hence, no prediction was made for the estimation of printability in this section.

19 experiments (2^4+3) were performed in randomized order. Filaments exhibiting different diameters were produced covering the entire range of acceptable filament diameters. Acceptable diameters of ~1.1 to ~1.9 mm were empirically determined in preliminary studies for F5 and print heads type I. The lower threshold for the diameter is predominantly determined by the fragility of a filament, which might deviate depending on the utilized formulation and polymer. The upper threshold, on the contrary, is limited by the inner diameter of the hot end.

Extruded filaments were tested to be printable according to adjustments shown in Table 13. Separate print jobs were used to print three DDS (Figure 46) of each filament. Set filament diameter was adapted in slicer settings based on the in-line determined mean diameter. Thus, the slicer software calculated the required amount for the printing process. This was indispensable, as e.g. cross-sectional areas of filament no. 9 and filament no. 4 differed approximately three times. Keeping the diameter constant would have caused conveyance through the print head at the same speed and, thereby, porous or perforated printed DDS. Filament diameter, E_{mod} values, content, mass of the printed DDS and corresponding experimental settings are displayed in Table 3.

Table 3. Summary of determined properties of filaments produced during DoE runs sorted by increasing diameter (mean ± sd, n > 150 for filament diameter, n = 3 for E_{mod}, content and mass) (modified from [92] by courtesy of Taylor & Francis; Copyright © 2018 Taylor & Francis Group).

Exp. No.	PFR [g/min]	RPM [1/min]	TEMP [°C]	CBS [mm/s]	Filament diameter [mm]	E_{mod} [N]	API content referring to 30 % API as label claim [%]	Mass of printed DDS [mg]
9	5	20	140	74.55	1.08 ± 0.03	920 ± 55	104.07 ± 0.62	930.7 ± 13.8
15	5	40	180	74.55	1.09 ± 0.03	881 ± 8	105.33 ± 0.25	Not printable
11	5	40	140	74.55	1.09 ± 0.06	893 ± 34	102.95 ± 0.09	Not printable
13	5	20	180	74.55	1.19 ± 0.06	914 ± 42	102.71 ± 2.10	765.0 ± 10.9
14	10	20	180	74.55	1.35 ± 0.03	1124 ± 99	103.84 ± 0.71	973.9 ± 111.4
3	5	40	140	46.67	1.37 ± 0.05	1257 ± 54	105.76 ± 1.32	942.4 ± 39.2
7	5	40	180	46.67	1.38 ± 0.05	1211 ± 73	103.22 ± 2.08	918.2 ± 53.5
1	5	20	140	46.67	1.40 ± 0.04	1278 ± 50	99.71 ± 2.02	986.6 ± 17.84
5	5	20	180	46.67	1.40 ± 0.05	1215 ± 17	101.11 ± 0.63	947.1 ± 130.1
17	7.5	30	160	60.61	1.46 ± 0.03	1380 ± 18	102.49 ± 0.61	721.7 ± 14.6
18	7.5	30	160	60.61	1.48 ± 0.03	1294 ± 18	103.06 ± 1.01	766.9 ± 10.7
19	7.5	30	160	60.61	1.48 ± 0.03	1380 ± 38	104.50 ± 1.24	741.6 ± 12.8
10	10	20	140	74.55	1.54 ± 0.03	1446 ± 15	105.52 ± 1.95	813.7 ± 20.6
12	10	40	140	74.55	1.54 ± 0.04	1384 ± 13	102.48 ± 0.80	801.6 ± 29.0
16	10	40	180	74.55	1.60 ± 0.03	1283 ± 84	108.69 ± 1.13	955.1 ± 41.18
6	10	20	180	46.67	1.83 ± 0.02	1505 ± 88	105.52 ± 1.15	1034.9 ± 12.9
4	10	40	140	46.67	1.92 ± 0.03	1579 ± 25	105.18 ± 1.68	739.9 ± 10.2
2	10	20	140	46.67	1.93 ± 0.02	1336 ± 53	103.36 ± 0.79	Not printable
8	10	40	180	46.67	1.96 ± 0.03	1608 ± 19	102.48 ± 1.29	Not printable

Models were built using backward regression to achieve highest Q^2 for all yield variables. For the API content only a poor model was developed ($R^2 = 0.45$; $Q^2 = -3.78$). The poor models illustrated that although set temperatures were varied in a wide range of 40 °C (140 °C to 180 °C) and increased PFR and RPM caused higher shears stress at the screws, these process parameters did not affect the API content, thus did not cause API degradation as already expected from DSC results (Figure 23). API contents ranged between 99 and 109 %. No systematic dependencies on process parameters were revealed. Regarding the API content, the formulation was considered robust and was hardly affected by process parameters. Content deviations were attributed to segregation inside the feeder and analysed in more detail in section 3.2.4.2. Conduction of 19 experiments was split among two days without choosing a block variable. Each time, the powder mixture (700 g) for one day was completely filled into the feeder before starting the extrusion. Different runs were then performed by adjusting the extrusion parameters. However, the mixture remained in the feeder during all runs of the day. Filaments produced later exhibited higher API contents. Therefore, segregation was considered probable. Regarding the polymer, 180°C was a high set extrusion temperature. However, the temperature and pressure transducer in front of the die, showed temperatures below 150 °C for the melt for all experiments. Based on DSC measurements and literature degradation was considered unlikely (section 3.1.4.3 and [107]).

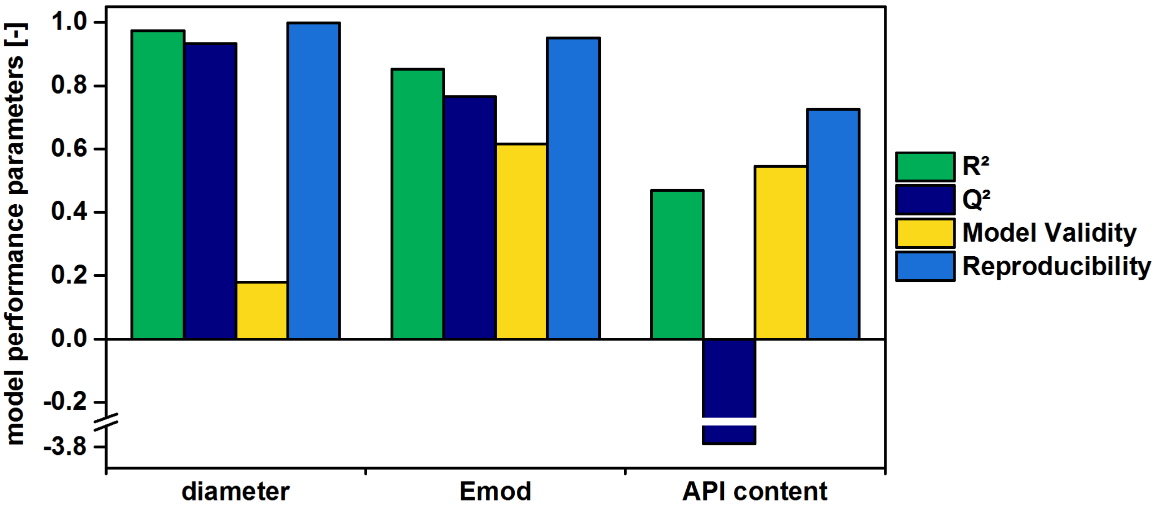

Figure 26. Summary of fit for yield variables diameter, E_{mod} and API content ($n = 19$; $\alpha = 0.05$).

Goodness of the models for diameter and E_{mod} as yield variables was underlined by $R^2 > 0.85$ and $Q^2 > 0.77$. Model validity was low in both cases due to the high reproducibility: experimental settings of the centre points led to very similar filaments (Table 3, filaments no. 17-19). Coefficient plots for the diameter and the E_{mod} values are displayed in Figure 27. They illustrate that the PFR and the CBS strongly influenced both parameters in a similar manner. Thereby, they underlined the assumption that the mechanical resilience of filaments based on the same formulation was mainly determined by the diameter. Increasing PFR increased the diameter and the mechanical resilience. Two effects might have contributed to this. On the one hand, more material reached the die, which might have led to a more pronounced elastic recovery. On the other hand, the filament came out faster and might have been compressed by the conveyor belt, whose speed was kept constant. Consequently, filaments were larger in diameter and had increased mechanical resilience. Increasing CBS, on the other hand, caused more stretching of the extrudate and, thereby, decreased diameters and mechanical resilience.

During model building for the yield variables diameter, E_{mod} and API content, TEMP as factor and all corresponding interactions were excluded as insignificant in all cases. In advance, it was suspected that lowering the temperature and thereby increasing melt viscosity and shear stress, might lead to a more pronounced die swell and diameter increase. This was not the case in this experiment. As stated in section 3.1.4.1., the high drug load of 30 % and consequently lower amount of viscoelastic polymer might be considered responsible for the negligible die swell.

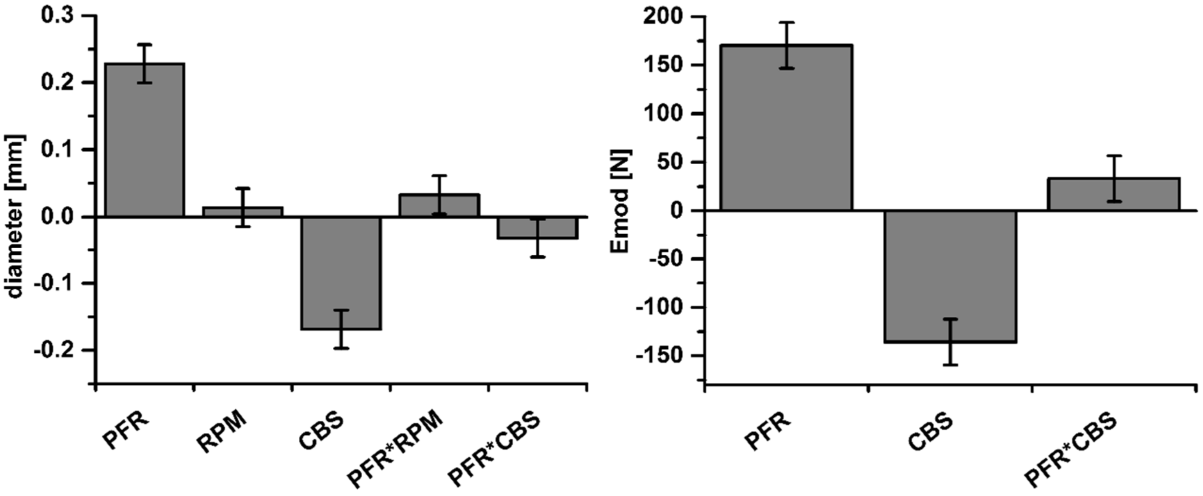

Copyright © 2018 Taylor & Francis Group

Figure 27. Coefficient plots for yield variables diameter (left adopted from [92], by courtesy of Taylor & Francis) and E_{mod} (right) (coefficient ± CI; n = 19; α = 0.05).

Between filament diameter and mass of a printed DDS no correlation was found. Thus, larger diameters did not cause a higher mean mass or the reverse. This was explained by adjustments of printing parameters according to the filament diameter, otherwise printing would not have been feasible. However, dosage forms did not exhibit the same mass, since diameter could be pre-set in the software with only one decimal, causing inaccuracies in this regard. Further, several filaments showed uneven surfaces (Figure 28), which might have contributed to this high difference as well.

Differences in surface structures of the filaments were observed. Representative examples are depicted in Figure 28. Filament no. 6 was smooth and shiny, no. 9 was less smooth and no. 16 exhibited a rough surface. However, attempts to quantify the roughness via scanning electron microscope or via determination of pixels at the interface using image analysis failed. Scattering parameters obtained by in-line diameter analysis (e.g. standard deviation), did not show consistency compared to visual inspection, either. Due to this, surface structures were solely examined visually, but could not be used as a reliable yield variable in a DoE. Differences in surface structures suggested that these filaments behaved differently during printing. A better conveying performance for rough filaments due to better grip at the conveying system of the print head or higher mass deviations due to higher diameter inaccuracies could be imagined. Comparing mass deviations of printed dosage forms with the three depicted filaments (Figure 28), filament no. 16 caused the highest relative standard deviation (4.3 %), followed by no. 9 (1.5 %) and no. 6 (1.2 %) (Table 3). Deviations in mass due to inconsistencies in diameter seemed to be probable. Assumptions that smooth filaments might show less grip during conveyance and, thereby, higher mass deviations were not confirmed. Nevertheless, even small diameters ($d_{no.9}$ = 1.08 mm) were reliably processable based on small relative standard deviations in mass of the dosage forms (1.5 %). Present findings revealed the printing process as more robust than expected, since filaments of diameters ranging from 1.08 mm to 1.92 mm were adequately processable, although the diameter recommended by the company was 1.75 mm.

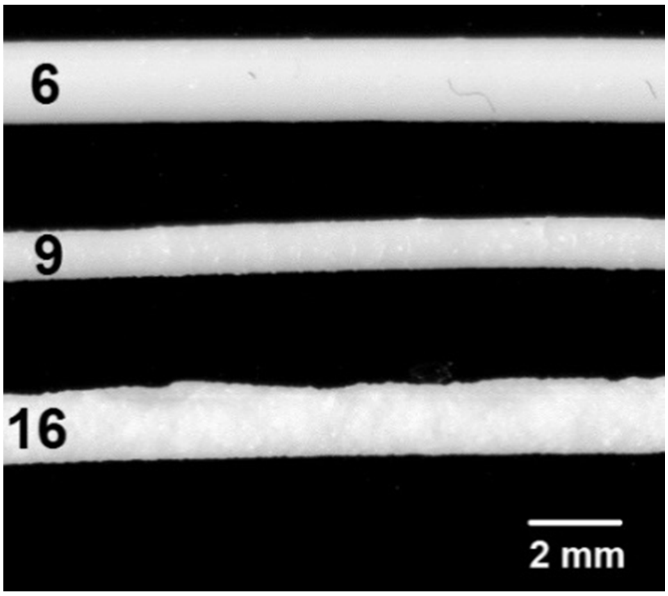

Figure 28. Extruded filaments of experiments 6, 9 and 16 (from top to bottom) exhibiting remarkable differences in surface structures.

15 of the 19 produced filaments resulted printable. No. 2 and no. 8 exhibited, at least at some points, diameters too large for passing the hot end. No. 11 and no. 15 were not printable due to high fragility. No. 9, however, which even showed a smaller mean diameter than no. 11 and no. 15 but a higher E_{mod}, was printable. It was supposed that printability of no. 11 and no. 15 was not given due to rough surfaces, involving predetermined breaking points despite a sufficient diameter. At larger diameters, this effect did not have consequences, as the filament itself was rather resilient. The predetermined breaking points of rough surfaces might also explain why the models built for diameter and E_{mod} were not completely congruent, although the diameter seemed to be the important influencing parameter for the mechanical resilience. These surface defects therefore caused in some cases faster material failure than expected solely based on the diameter.

The presented DoE allowed a more thorough understanding of the filament production process. Although experiments were performed using one formulation (F5), results are likely transferable to other formulations as well. During the DoE, a maximum throughput of 600 g/h, comprising 268 m of filament per hour, was achieved. Considering an average mass of 470 mg per dosage form as used in section 3.4.3 (25 % infill), this throughput would be suitable for the production of more than 1200 printed DDS per hour. As most important key factors, the PFR and the CBS were identified to influence the filament diameter and resilience. Therefore, CBS could be used to allow versatile adjustment of the filament diameter without changing the HME process and without waiting for a new process equilibrium. Filament diameter and resilience appeared to be associated. Exceptions were found in case of rough surfaces representing predetermined breaking points. Thereby, the mechanical resilience decreased sharply despite of similar diameters. Rough surfaces also caused higher deviations in the mass of printed DDS. Thus, production of smooth filament surfaces should implicitly be preferred. The absolute size of the diameter did not influence the mass of the DDS, since it was compensated by slicer adjustments. Which experimental settings should finally be chosen, however, mainly depends on the thermal stability of all components, the elastic recovery of the polymer and the feasibility of accurate filament collection behind the outlet, since this becomes distinctly more difficult with a higher throughput.

3.2.3.2. Continuous Production of Drug-Loaded Filaments

For the production of filaments used for 3D-printing trials, 5 g/min was chosen as PFR, 20 as RPM, 160 °C as extrusion temperature and 30.52 mm/s as CBS. 160 °C were chosen as extrusion temperature, since, during the DoE, filaments produced at higher temperatures generally exhibited a smoother surface than those produced at lower temperatures. However, 160 °C were considered sufficient and the thermal load should not be increased without need. The CBS was chosen lower than in the DoE trials to achieve a larger diameter and thereby decrease probability of filament breakage in the print head. Further, decreased moving speed of the filament, made filament collection more accurate. The collection was performed manually in a bucket directly behind the diameter measurement module and was more difficult for longer extrusion runs if the throughput was higher. This caused twisting of the filament and, thereby, difficulties during the printing process or even breakage. The CBS and the PFR had to be coordinated and, therefore, a PFR of 5 g/min was chosen decreasing the throughput in favour of accurate filament collection and avoidance of filament breakage.

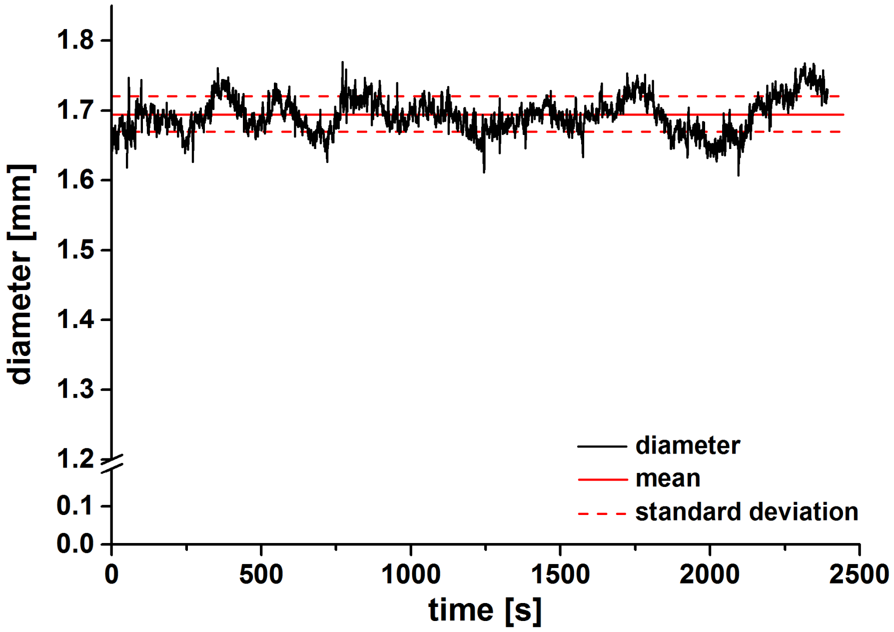

Figure 29. In-line measured diameter values (1 Hz) during 40 min extrudate sampling using F5 (adopted from [92], by courtesy of Taylor & Francis).

Figure 29 displays the in-line measured diameters for a 40 min extrudate sampling of F5 processed with above stated experimental settings. Reasons for diameter fluctuations have already been mentioned in section 3.1.4.1. Achieved mean value was 1.69 mm and diameters ranged between 1.64 and 1.75 mm. Thus, even in event of local bulges, the filament would be conveyed reliably inside the print head. Scattering of the diameter values might be decreased further by increasing CBS. Since printed DDS were rather large (section 3.4), the extent of diameter scattering was not considered severely affecting quality of the dosage forms. Approximately 15 cm of extrudate were needed to print one dosage form. With regard to a CBS of 30.52 mm/s and a recording frequency of the diameter of 1 Hz, five diameter values per extrudate piece for printing were obtained. Considering five diameter values in a maximum (342-346 s, Figure 29) and five diameter values in a minimum (2038-2042 s, Figure 29) resulted in 1.73 mm and 1.64 mm for the mean diameter and, thereby, in 2.35 mm² and 2.11 mm² for the cross-section of that filament pieces. Filament pieces achieving exactly the mean diameter of 1.69 mm had a cross-section of 2.24 mm². The filament was always printed with the same pre-set speed, meaning that always the same length of extrudate was applied for one dosage form. Based on the previously presented calculations, deviations in mass due to varying diameter would be in a range from 94 % (1.64 mm) to 105 % (1.73 mm) around the mean (1.69 mm). As these are the extreme cases and most dosage forms were supposed to exhibit a mass in between these limits, this was considered acceptable. Suggestions for further increasing the diameter uniformity were presented in section 3.1.4.1 and mainly focused on increase of API ratio and elaboration of different screw configurations.

At a PFR of 5 g/min, the throughput per hour was 300 g, corresponding to ~110 m of printable filament. Drug load was 30 %. Assuming a realistic dose of 300 mg and neglecting process waste, produced filament was suitable for printing of 1,000 DDS. Since the process was continuous and could easily be scaled up by prolongation of process time, it was called pilot scale [108, 109]. This underlined contribution of the present study for bringing continuous filament production closer to pharmaceutical industry.

3.2.3.3. Analysis of Residence Time

A detailed analysis of the HME process also involved the determination of the residence time of the API and excipients inside the extruder barrel. This information is of great interest in continuous production to trace materials in the process and to estimate waiting time for next sampling after any kind of unforeseen incident. Further, it helps to examine thermal stress generated during the HME process, which is particularly interesting, considering FDM^{TM} as subsequent process also generating thermal stress. In addition, pressure and shear stress during processing should be taken into account. These factors might lead to API degradation [110] and emphasize the necessity for residence time analysis during the present work.

For the determination of residence time distribution the ExtruVis system was utilized as it was shown to provide reliable results in other applications [94, 111]. Red iron oxide was identified as appropriate dye to be detected by the camera in a white extrudate. The experimental setup is shown in Figure 30. Generally, 1 % of the throughput per second is recommended as amount of tracer [94], since adding the tracer should not influence the process and, thereby, the residence time. In this case, amount of tracer should have been 0.83 mg using a PFR of 5 g/min. This small mass could not be weighed reliably. Therefore, a small amount was added without weighing in advance. Two trials were performed. Further process settings were the same as in section 3.2.3.2.

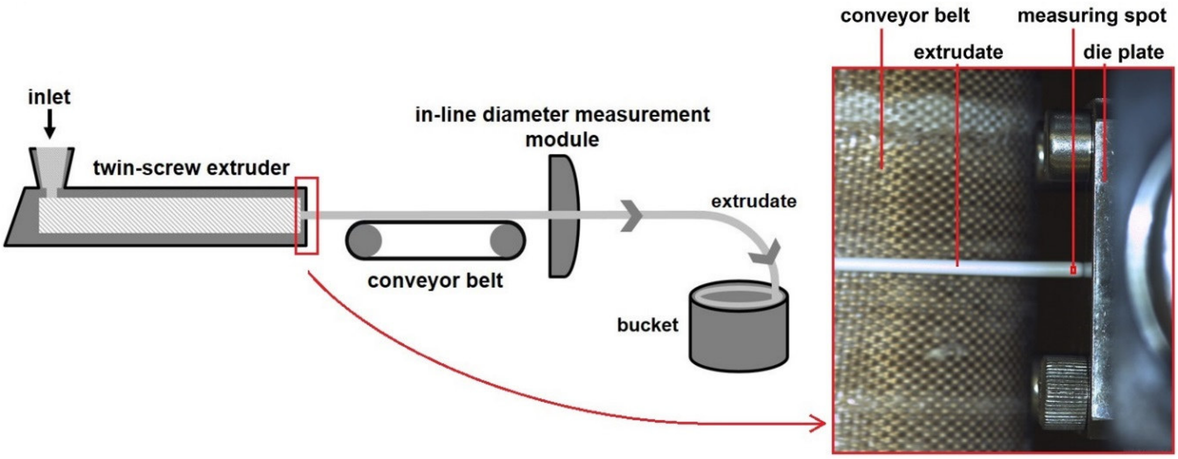

Figure 30. Schematic picture of the extrusion process (left) and top view of experimental setup for residence time analysis (right).

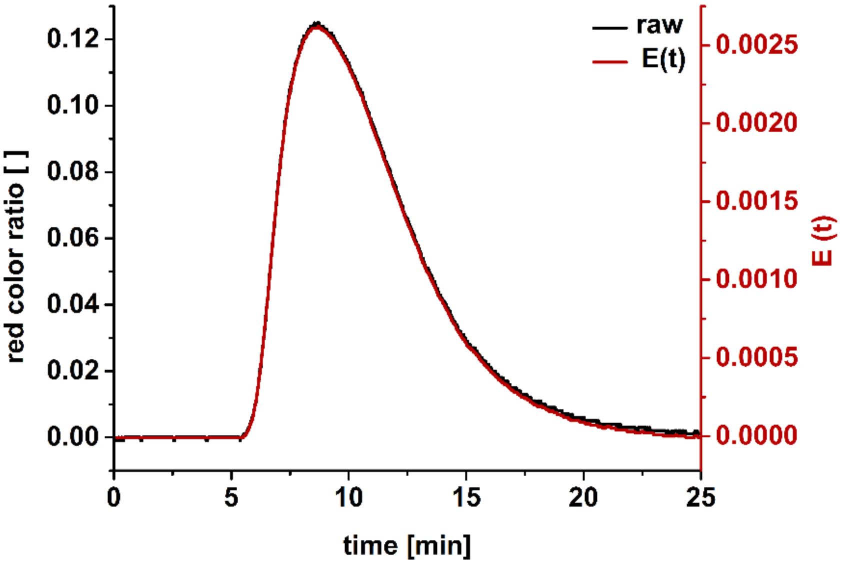

Figure 31. Raw data obtained during residence time distribution trial (n = 1) and exit age function fit calculated by ExtruVis software.

Figure 31 displays exemplarily raw data obtained during one trial and the corresponding fit to the exit age function (E(t)) performed by the ExtruVis system. As expected, a sharp increase of tracer and a longer washout phase were found resulting in an asymmetric curve. Even the raw data curve appeared very smooth and could hardly be distinguished from the fitted one. This indicated optimal measurement conditions. Reasons were the good contrast between the red colorant and the white sample, as well as the smooth surface of extrudate. The measuring spot was continuously covered by the extrudate, in comparison to granulation processes in which ExtruVis system was applied previously [94, 111]. This contributed to low scattering of raw data as well. Figure 31 further shows that the fitted curve generated by the software matched the raw data well. This was important, since the MRT was calculated based on the fitted curve. The time required for the first tracer particles to come out of the extruder was determined to 333 and 332 s. Tracer was washed out after 1475 and 1421 s, respectively. Resulting MRTs were 641 and 643 s. MRT of an extrusion process is mainly depending on the length of the extruder, on the PFR, the RPM and the screw configuration. The applied screw configuration did not contain extensively long or backwards kneading zones. Compared to other studies, which examined MRTs of 112 to 300 s in an HME process [71], residence times in this study was long due to the small throughput of 5 g/min at 20 rpm. Since these parameters were chosen due to handling problems of the finished filament (section 3.2.3.2), in case of processing thermally instable drugs, residence time might be decisively decreased, by increasing the throughput and using an automatic winder for the filament collection.

3.2.4. Theophylline Assay

3.2.4.1. Drug Distribution along the Filament

After the analysis of the production process parameters, drug distribution along the filament was investigated regarding its homogeneity, since it is essential to print DDS exhibiting proper drug content uniformity. As F5 and F10 should be used for the printing studies, drug distribution was analysed in both cases. 500 g of the powder mixtures were extruded and theophylline content was determined at the beginning, in the middle and at the ending of the sampled filament after reaching a process equilibrium. The whole length of the sampled filament was approximately 100 m. A sample size of 400 mg, corresponding to approximately 15 cm of extrudate, was chosen approximately correlating with the mass of one printed DDS with 20 % fill density and printer settings used in section 3.4.3 (Table 13). Results of content determination are displayed in Table 4.

Table 4. Theophylline content [%] of F5 and F10 filaments determined at the beginning, in the middle and at the ending of the sample.

	beginning	middle	ending	mean ± sd
F5 (7 % SA)	97.41	97.71	97.96	97.70 ± 0.27
F10 (7 % PEG4000)	98.90	98.11	98.76	98.59 ± 0.42

Between the different positions, no obvious differences could be observed. Drug distribution along the filament was homogenous, indicated by low standard deviations in both cases (0.27 % for F5 and 0.42 % for F10; Table 4). However, the content was in all cases below the target value. Thermal instability and segregation inside the feeder were considered as reasons and were examined in more detail in the following.

3.2.4.2. Analysis of low API Content: Thermal Stability and Segregation

Thermal Stability

Thermal stability of the utilized API is indispensable in case of processing it in an energy and heat intensive process, such as HME or FDM^{TM}. Anhydrous theophylline is an API widely utilized in and considered suitable for HME [112]. Further, DSC thermograms and hot-stage microscope pictures of anhydrous theophylline indicated thermal stability at temperatures below 300 °C. Nevertheless, degradation of theophylline occurred during HME, using tribasic sodium phosphate as excipient [58]. A reaction of both components at elevated temperatures was considered responsible for this. According to Ph. Eur. 2.9.40, filaments with 97.4 to 98.9 % drug content and a homogeneous distribution were likely to generate DDS within the tolerated range [113]. Filaments produced during the DoE showed higher content variations, which might not be in the tolerated range (Table 3). Therefore, this phenomenon was further investigated, as no obvious explanation was found and drug contents below the target values occurred in all cases for F5 and F10. Thermal degradation or incompatibilities due to the elevated temperatures during HME were considered as potential reasons.

Powder mixtures of F5 (30 % theophylline) and F8 (50 % theophylline) were freshly prepared and examined to reveal whether the occurrence of lower API content depended on the API concentration. Thermal treatment of physical mixtures was performed for 15 min at 180 °C in an oven. Settings were consciously chosen higher than those in the extrusion process (MRT = 10 min, TEMP = 160 °C), since the application of shear stress was not feasible in this experimental setup and the worst case should be mimicked. Same physical mixtures were also measured without thermal treatment for reasons of comparison.

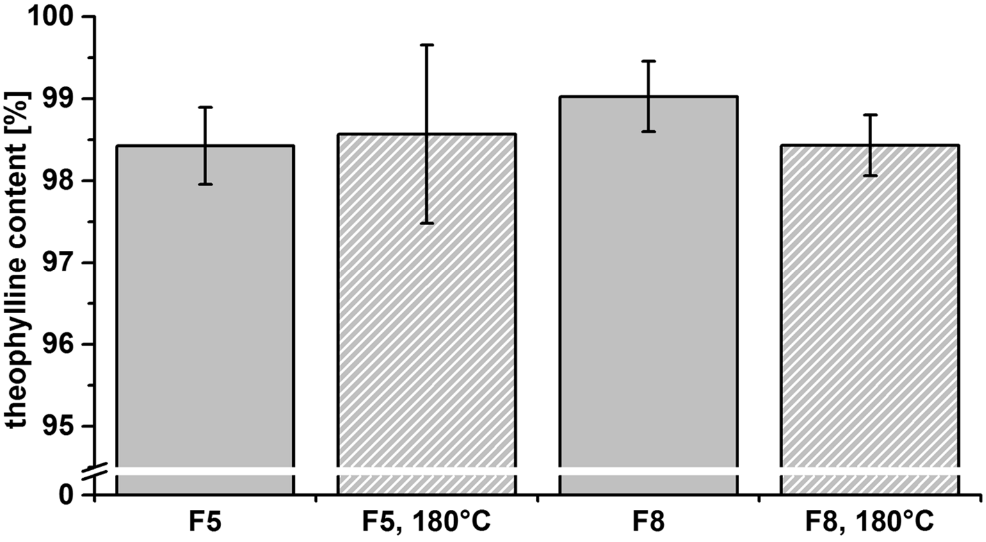

Figure 32. Theophylline content of F5 and F8 powder mixtures. Values for the dashed columns were determined after thermal treatment of 15 min at 180 °C (mean ± sd; n = 3).

Figure 32 illustrates that differences were hardly observed between thermally treated mixtures and those that were not thermally treated. 30 % theophylline mixtures exhibited an API content of 98.4 and 98.6 % of the nominal claim, whereas 50 % mixtures contained 99.0 and 98.4 %. Despite of thermal treatment no differences in content were observed. Since UV-VIS spectroscopy was used for quantitative determination without chromatographic separation using an HPLC column, degradation products absorbing at the same wavelength could not be distinguished from the drug. However, previous DSC measurements (section 3.1.4.3) and literature data [112] underlined thermal stability as well. In case of reaction products of API and excipients a shift of the maximum could be supposed, but an absorbance at the chosen wavelength would still be probable. Nevertheless, all mixtures contained less API than they were supposed to. This indicated theophylline might have selectively adhered at the glass walls of the mixing vessels.

Segregation

Regarding the low API content, segregation of components was an important issue to examine. Mixtures containing two or more non-identical raw materials might show segregation. Besides factors such as surface structure, density and shape of the particles, different particle sizes are in particular responsible for this phenomenon [114, 115]. Since in the experimental setup, the powder feeder stood on the extruder, vibrations resulting from the extruder engine, stirring of the feeder and dead zones in the feeder were likely to affect homogeneity of the powder blend during the process. However, also vibrations from the feeder itself could have an impact and favour separation of particles.

Particle size measurements for raw materials of F5 were performed and corresponding results are displayed in Table 5. Particle size of theophylline was much smaller (x_{50} = 13.6 ± 0.2 µm) than the particle size of aPMMA (x_{50} = 86.3 ± 1.9 µm). SA appeared to have the largest particles of the raw materials (x_{50} = 214.8 ± 2.8 µm). Since the mixtures only contained 7 % SA and no differences in mechanical properties along the filament were observed, segregation of SA was considered negligible. Differences in particle size regarding the API and the polymer suggested probability of particle segregation.

Table 5. Particle size of raw materials used for F5 (n = 3; mean ± sd).

	particle size [µm]		
	x_{10}	**x_{50}**	**x_{90}**
aPMMA	26.0 ± 0.6	86.3 ± 1.9	229.7 ± 2.9
SA	68.2 ± 1.3	214.8 ± 2.8	483.8 ± 5.4
anhydrous theophylline	4.6 ± 0.0	13.6 ± 0.2	50.8 ± 4.5

However, differences in particle size did not explain why a homogeneous distribution of API resulted. For this reason, off-line dosing experiments were performed with batch size and PFR (300 g and 5 g/min, section 5.5.2.1) commonly used in this work. Off-line experiment was chosen to avoid distortion of results by the extrusion process, so that issues only concerning the feeding could be determined. The trial was carried out for 45 min (≈ 225 g), since the amount of the residual powder in the feeder was not sufficient for reliable dosing. At time points 0, 10, 20, 30, 40 and 45 min samples (n = 3) were taken. Powder was directly dosed into flasks for quantitative analysis with a sampling time of 5 s, corresponding to 427 ± 34 mg (n = 18; 3 samples at 6 time points). Theophylline content of the residual powder was determined after blending it using the turbula mixer. Particles adhering at the walls of the feeder were also included in this fraction. Blending of the residual powder was done to avoid content distortion due to possible inhomogeneous drug distribution in this fraction. Sample size of the residual powder was 397 ± 2 mg (n = 3). Figure 33 displays determined theophylline contents at different time points. Before starting the experiment, content was with 101.17 ± 0.69 % slightly above the target content, probably due to analytical inaccuracies. After 10 min, content fell to

96.97 ± 0.48 % and increased over time to 99.18 ± 0.18 % at 45 min. Nevertheless, tendency between these points was hard to interpret, since standard deviations at time points 30 and 40 min were rather large. The content of the residual powder from the feeder was 5.25 % above the target content. Consequently, theophylline tended to remain in the feeder. It was supposed that segregation was present, as indicated by differences in particle size (Table 5). Due to the smaller particle size, theophylline particles would be expected at the bottom of the feeder and, therefore, to come out first. This was, however, not the case in the present experiments. It was concluded that after segregation, the small theophylline particles remained in dead zones at the feeder bottom, which were covered neither by the agitator nor by the screws feeding the powder. This effect might have been even more pronounced due to the tendency of theophylline to adhere at the feeder walls, as it was supposed for the walls of the mixing vessel in previous experiments. Explanations based on surface structures, shape or density were not investigated further.

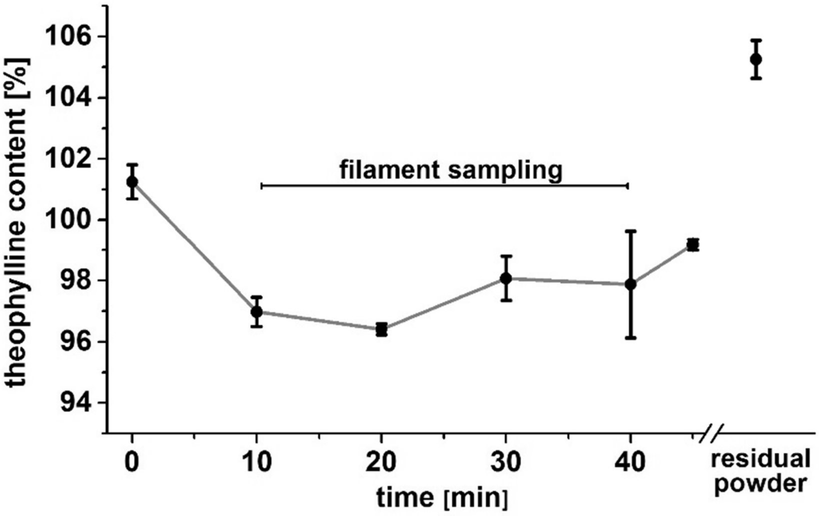

Figure 33. Theophylline content of the powder mixture determined in the off-line dosing experiments for segregation analysis (n = 3; mean ± sd). Horizontal bar indicates, which powder fraction was usually used for filament sampling.

The results of these experiments can be used to explain the homogenous API distribution, which was mentioned in section 3.2.4.1: prior to starting collection of samples, the process equilibrium was awaited. Since MRT was ~642 s (section 3.2.3.3), waiting for the process equilibrium took >10 min. Due to unreliable dosing when the feeder was almost empty, sampling always ended before 40 min. The time for filament sampling is exemplarily depicted in Figure 33. These findings and analysis of drug distribution fit well and explained the decreased but constant API content (Table 4).

In this section, it was stated that the theophylline content was in all cases lower than the target content, but homogenous along the drawn sample extrudates. As reasons for this phenomenon, segregation due to different particle sizes and adhesion of the API to the equipment walls were determined. Content variations during the DoE (Table 3) were traced back to the larger batch sizes of 700 g. For thermal instability of the API, which might be the first assumption in case of HME, no evidence was found. The same applied to potential incompatibilities. API homogeneity and content of the filaments were considered acceptable for this experimental setting. Discrepancies between the target and the effective content were evident, but filaments with 97.4 % API content in worst case were considered to comprise printed DDS within the range of the Ph. Eur. monograph 2.9.40. Further, due to the homogeneous distribution, a lower API content of filaments could easily be respected in the print settings. If larger batches are manufactured, the problem of segregation and adhesion might be more pronounced and should therefore be considered. Of course, a different API might show a different behaviour in this regard. Issues of segregation and adhesion should be re-evaluated dealing with a different API.

3.2.5. Ageing

3.2.5.1. Change of Physico-Chemical Properties During Storage

Assuming filaments might once be produced by a pharmaceutical manufacturer and later be printed into DDS by local or clinical pharmacists, stability of physico-chemical properties of filaments as intermediates becomes an important issue.

If a molten or softened amorphous polymer is cooled down, it undergoes a change from a rubbery, flexible state to a hard and glassy state. This change takes place at the glass transition temperature, the temperature at which rotation and translation of molecules are inhibited [116]. The free volume, defined as available space between the molecules, is considered large at high temperatures. This results in a high mobility of the polymer chains [117]. The free volume might be increased by using plasticizers, which consequently lower the glass transition temperature (section 3.1.4.3). Below the glass transition temperature, polymers are considered in an unstable state: the polymer exhibits a larger free volume, entropy and enthalpy than in thermodynamic equilibrium. Although rotation and translation cannot take place, movements of the polymer chains are not yet completely inhibited. Reaching a more stable thermodynamic state happens by slowly undergoing a decrease in free volume. This phenomenon is called physical ageing and occurs in all amorphous polymers. Therefore, it is likely to occur in extruded filaments as well. Ageing causes increase in stiffness and brittleness [79, 118, 119]. Further, temperature dependent solubility of the plasticizer in the polymer matrix should be considered. Throughout the HME process, a larger amount of plasticizer might have been dissolved than is soluble at room temperature. This might have caused changes in mechanical properties during storage as well. For these reasons, occurrence of ageing and changes in mechanical properties over storage was indispensable to examine.

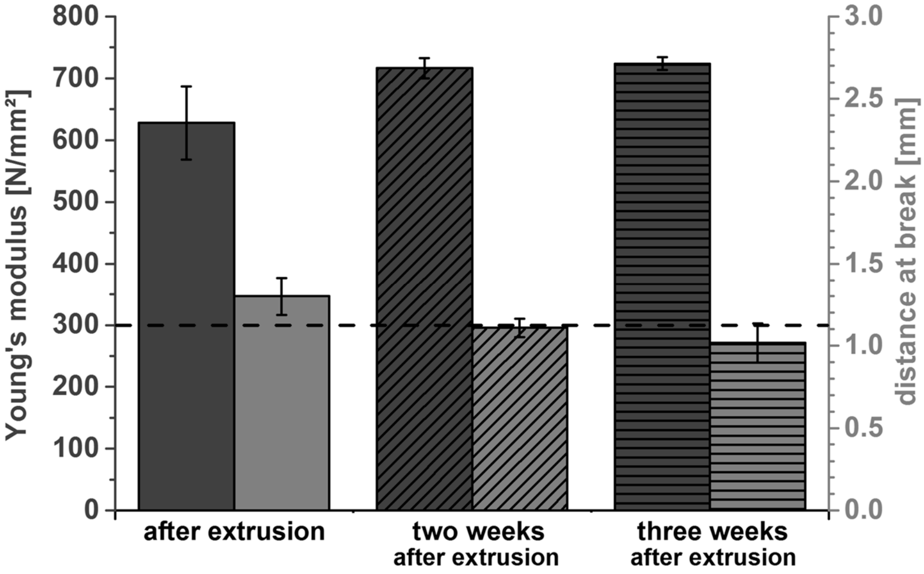

Figure 34. Changes in mechanical resilience of F5 filaments over storage of two weeks (n = 6; mean ± CI). Dashed line marks thresholds for YM and distance at break, which should be exceeded for printability.

F5 filaments were stored at 22 °C for two weeks and mechanically characterized at days 0, 7 and 14 after extrusion. Further, printing was tested at these time points. Results indicated that the YM increased during the first 7 days, from 628 to 716 N/mm² and was constant afterwards (both significant in an unpaired two sample student's t-test, α = 0.05) (Figure 34). On the other hand, distance at break decreased from 1.3 to 1.1 and finally 1.0 mm. At days 7 and 14 printability was no longer given, since the brittleness was too high. This was expected, since values for the distance at break were below the defined printability threshold of 1.125 mm (section 3.1.4.2). Observed increase in stiff- and brittleness was exactly what was expected based on literature [119]. However, the time, which was needed for the impairment of mechanical properties until printability was no longer given, could not be predicted, since it is polymer and formulation dependent. For F5, this period was found to be short with < 7 days. The consequence for the present work was that all trials on printability and printing of DDS were conducted within 2 days after extrusion. For the present work, this procedure was applicable, whereas for an industrial filament production and subsequent processing in a hospital this tight schedule would hardly be viable.

3.2.5.2. Curing

During tablet coating using aqueous dispersions, curing processes are widely known. Subsequent to the coating process, tablets are exposed to elevated temperatures to promote coalescence and, thereby, consistent film formation [77, 120]. Based on this, curing of extruded filaments was performed at temperatures of 60 °C for 24 h. Since HME is a solvent-free process compared to coating, coalescence might not play a role in this case. However, it was suspected, that storage at temperatures above the glass transition temperature, higher mobility of polymer chains might favour faster achievement of a thermodynamic equilibrium, due to kinetic facilitation. Further, storage close to the melting point of SA might promote its molecular dispersion in the matrix and, thereby, optimal plasticizing ability. Thus, the assumption was to reach a state, which was more stable before storing the filament. Higher temperatures than 60 °C led to filament deformation. Therefore, curing temperatures higher than these were not considered in this study.

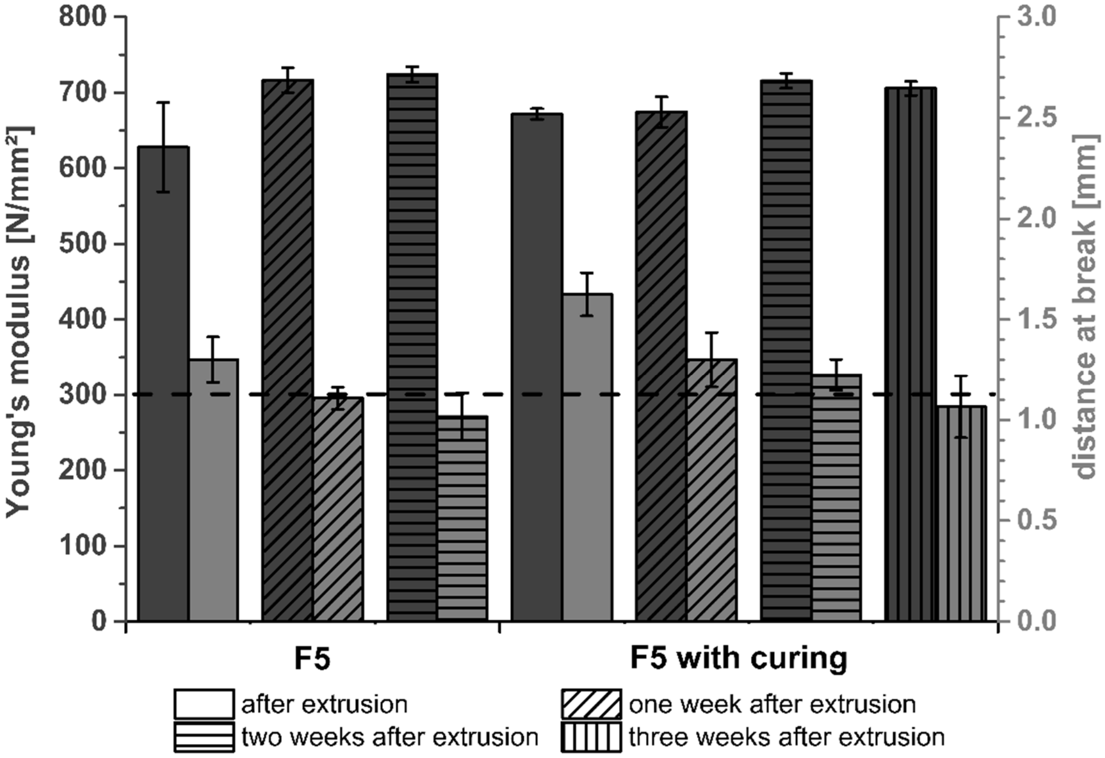

Figure 35. Changes in mechanical resilience of F5 filaments with and without curing over storage (n = 6; mean ± CI). Dashed line marks thresholds for YM and distance at break, which should be exceeded for printability.

Mechanical properties of cured filaments were determined after curing of 24 h, equal to day 2 after extrusion, days 7, 14 and 21 after production. Filaments were stored at 22 °C after curing. Relative humidity was not controlled. Results were compared to those of F5 filaments, which were already shown in Figure 34. For those filaments, which have been thermally treated, the same tendencies regarding mechanical resilience were observed (Figure 35). The YM increased and the distance at break decreased over time. During two weeks of storage, the range of the YM was smaller (672 and 716 N/mm²) than for F5 filaments without curing (628 and 724 N/mm²). Increase in stiffness was consequently less pronounced. At the same time, the distance at break of cured F5 filaments decreased from 1.6 to 1.2 mm and of uncured F5 filaments from 1.3 to 1.0 mm. For the cured filaments, printability was still given after two weeks, also indicated by mechanical resilience values exceeding the threshold in all cases.

Therefore, cured filaments were analysed after three weeks as well. After this time, however, brittleness was too high for being printed, indicated by a distance at break of 1.1 mm, although YM of 705 N/mm² was still sufficient. Consequently, filaments broke inside the print head.

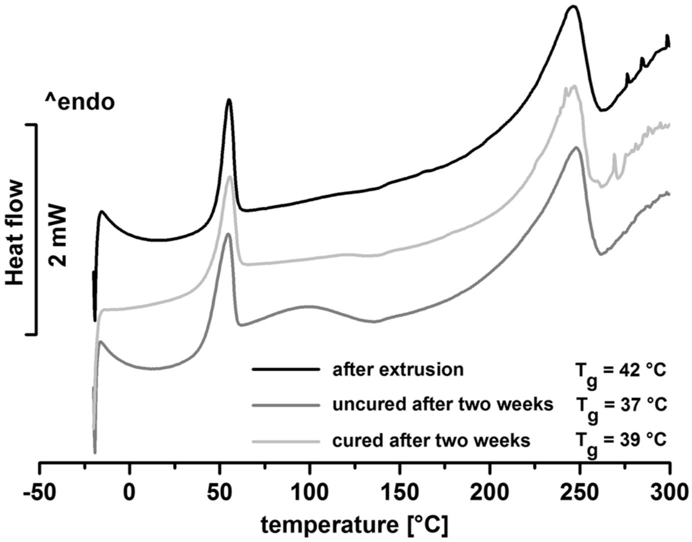

Figure 36. Selected DSC thermograms of F5. Glass transition temperatures were determined according to section 5.5.5.5.

In addition, DSC measurements of cured and uncured filaments were carried out to compare their properties after two weeks of storage. Thermograms are displayed in Figure 36. F5 after extrusion and cured F5 after two weeks exhibit similar curves. This reflects the similar results from mechanical resilience testing (Figure 35). Uncured F5 after two weeks showed incorporation of water, indicated by a wide peak between 75 and 125 °C. Generally, water can act as plasticizer, which would imply an increase of flexibility [103]. However, this is likely not the case because water is insoluble in the polymer matrix and would preferably be present at the filament surface and not in the whole filament. As the free volume was expected to decrease over time, the glass transition temperatures was expected to increase. Nevertheless, based on the obtained DSC curves, this was not confirmed. Small changes in glass transition temperature might be below the detection limit of the DSC. Further, determination of the glass transition temperature might have been susceptible to inaccuracies due to the melting peak of SA, which was detected in the same temperature range. Crystallization of the plasticizer aside the polymer was also considered as promoting factor for brittleness, since, thereby, integrity of the matrix might have been disturbed. Crystallization of the plasticizer might occur since the solubility in the polymer matrix might be higher at the elevated temperatures during production. However, due to simultaneous occurrence of melting of SA and the glass transition temperature of the polymer, quantification before and after storage via the integral of the melting peak normalized by the sample weight, was not feasible.

It can be summarized that curing indeed had a positive influence on mechanical properties (Figure 35) and prolonged processing of filaments from a few days to two weeks. This might be exceeded further when investigating optimal curing conditions also considering humidity. Nevertheless, in this study, ageing of filaments was delayed but not impeded. This problem could not be satisfactorily solved. As an influence of curing and different curing conditions on the release of theophylline from the matrix could not be excluded, all printing trials during this work (section 3.4) were conducted with uncured filaments one to two days after extrusion.

3.2.6. Summary

The key formulation, containing 30 % anhydrous theophylline, 7 % SA, aPMMA and 0.4 % colloidal anhydrous silica (F5), was thoroughly analysed, since it was applied in subsequent printing studies.

Regarding the applied process, the DoE revealed that PFR and CBS had the biggest influence on diameter and mechanical resilience. The PFR influenced the mass throughput, whereas CBS caused stretching or compression of the filament and, thereby, changes in diameter. Optimal production conditions for F5 were found, also considering the manual rolling-up of the filament behind the extruder outlet. Thus, continuous production of smooth filaments, with a throughput of 300 g/h corresponding to 110 m of filament per hour was feasible. The MRT was determined to ~642 s using a camera-based system (ExtruVis). The long residence time resulted from a low PFR of 5 g/min and a slow rotation speed (20 rpm).

Theophylline content of filaments was found to be always below the target content, in the worst case at 97.4 %. Segregation due to differences in particle size and adhesion of the API at equipment surfaces were determined as reasons for this finding. Thermal instability and incompatibilities could be excluded as possible causes. However, for a batch size of 300 g homogeneity of drug distribution along the filament was demonstrated. Reaching a target dose for DDS during 3D-printing might easily be conducted based on the actual API content of the filament. To achieve a homogeneous drug distribution in the filament if larger batches shall be extruded, the powder mixture might be divided and refilled. For the short time of refilling, the feeder shall be switched from gravimetric to volumetric mode.

F5 filaments exhibited ageing after extrusion when stored at 22 °C. Ageing extensively impaired mechanical properties, in particular by increasing brittleness. As a result, filaments were printable only a few days after extrusion. Amorphous polymers are generally considered to exhibit physical ageing due to reduction of free volume, causing higher stiff- and brittleness [116, 119]. Additionally crystallization of SA was suspected. Curing of filaments (60 °C, 24 h) delayed ageing and enabled printing up to two weeks. Nevertheless, this would still not be a sufficient storing period for processing of filaments in community or hospital pharmacies and might be analysed in further studies.

3.3. Thermal Stress in 3D-Printing

3.3.1. Introduction and Objectives

Compared to other means for individual dosing of solid dosage forms, e.g. capsule filling and tablet crushing, the thermal stress applied during DDS production (filament extrusion and FDM^{TM}) is a drawback and was consequently investigated. During 3D-printing, thermal stress was applied on the one hand during conveyance of the filament through the hot end of the print head and on the other hand during the stay of the unfinished DDS on the heated print bed. The set temperature of the print head had to be high enough to soften the polymer and was typically in a range of 60 °C to 230 °C [35, 47, 56, 58, 121]. The build plate temperature is usually elevated to ensure proper adhesion. Typical temperatures range up to 90 °C [15, 50, 58, 122]. Adhesion of the object printed was not only determined by the filament formulation but also by the shape of the DDS. Especially the amount of polymer printed in the first layer of the DDS was identified as important. DDS with little polymer printed in the first layer tended to show worse adhesion than those with more polymer in the first layer. Indeed, build plate temperatures were far below those of the print head but the exposure time was throughout the entire printing time.

Since many APIs are thermally instable, thermal stress during 3D-printing was studied assessing the residence time of the filament inside the print head based on a plug flow model. Seppala and Migler have successfully used an IR camera for thermographic measurements in 3D-printing while processing pharmaceutically non-usable acrylonitrile butadiene styrene [123]. Therefore, IR thermography was considered suitable for the present study and was applied to estimate actual temperatures at the print head and on the build plate.

3.3.2. Calibration of F-Units used in G-Code

G-code as a programming language is generally used for numerically controlled machines, e.g. for computerized numerical control (CNC) milling. It is described in DIN standards 66025-1 and 66025-2 and was further adapted for 3D-printing [124-126]. Codes consist of a variable and a dimensionless number to define its extent. Important variables are displayed in Table 6. For one command different variables are combined. G1 E1000 F150, for instance, means extrusion of 1000 units of filament at a speed of 150 units. As no coordinates are given, print head and build plate would remain in the current position. G-code files used during this work contained usually around 1200 commands for printing of one DDS. Besides generating the G-code information using a slicing software, single commands could be sent manually to the printer, too. This function was used during calibration of F-units as well as for print head and build plate thermography (sections 3.3.4 and 3.3.5). For subsequent thermography of the print head and of the build plate, a calibration of the F-unit used in G-code was mandatory (Table 6).

Table 6. Important variables used in G-code.

variable	description
G1	beginning of every command
F	feed rate of the filament **<u>or</u>** speed of the print head movement **<u>or</u>** speed of the build plate movement
E	length of the extrudate
X	coordinates for the print head
Y, Z	coordinates for the build plate

First, the feed rate of the filament was calibrated. The filament put into the print head was called inlet filament, the out-coming printed strand was called outlet filament (Figure 37). In the printer software, only the outlet speed could be entered.

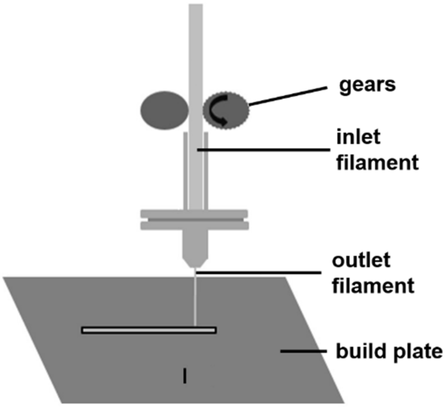

Figure 37. Print head type I. inlet and outlet filament are marked.

Since the speed of the outlet filament was hard to determine due to brittleness of the outlet filament, the speed of the inlet filament was determined (section 5.5.5.15) and converted into the outlet filament speed using Equation 1. Parameters v_o and v_i represent the speeds of the outlet and the inlet filament, r_o and r_i the radii of the outlet ($r_o \approx 0.2$ mm) and the inlet ($r_i \approx 0.85$ mm) filament.

Equation 1. Conversion of inlet filament speed into outlet filament speed.

$$v_o = \frac{\pi {r_i}^2}{\pi {r_o}^2} \cdot v_i$$

Commercial PLA (PLA green, Prodim International, Netherlands) was used for the conduction of the experiments, since it was considered to be conveyed accurately through the print head based on preliminary experiments. The inlet filament was marked lengthwise in distances of

10 cm. Manual command ‘G92 E0’, telling the printer it is in the start position, was entered followed by the extrusion command ‘G1 E100 FX’ with X equal to 20, 40, 60, 80, 100, 150 or 200. The experimental order was randomized and the print head temperature was set to 190 °C. The print head stayed in the same position during all experiments.

The conveying speed of the inlet filament was calculated using the length of the filament conveyed, determined via the applied marks, and corresponding time (n = 3) and then converted into the outlet filament speed using Equation 1. Values were in a range of 6.14 ± 0.03 mm/s and 44.29 ± 3.74 mm/s for F-units between 20 and 200 (Figure 38, a). It was apparent that standard deviations increased with increasing F-unit indicating that higher speeds caused inaccuracies in the conveying process of the filament. Therefore, conveying speeds were set to 15 mm/s for the outlet filament during the printing trials (section 3.4). In the following, the term ‘printing speed’ only refers to the outlet filament speed.

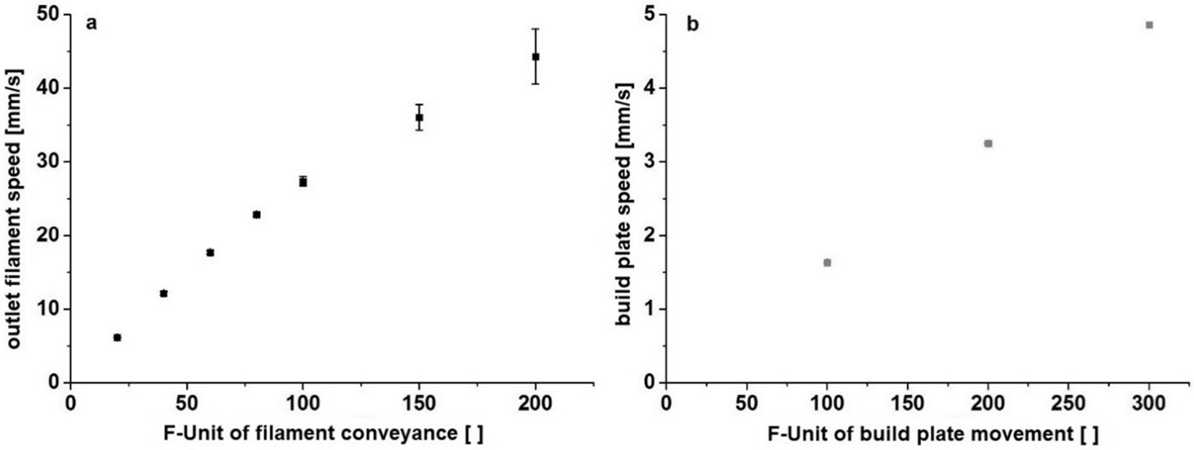

Figure 38. (a) Conveying speed of the outlet filament [mm/s] against F-units (n = 3; mean ± sd) and (b) movement speed of the build plate [mm/s] against F-units (n = 3; mean ± sd).

For thermographic measurements of the build plate, the camera was positioned centrally above the build plate. During the recordings, the build plate was moved with command G1 Y220 F300 from the back to the front, so that every part of it was once in the camera focus. After that, time-based temperature data from the recordings had to be related to corresponding positions on the build plate. Therefore, F-units for build plate movement had to be determined. Manual commands ‘G92 E0’ and ‘G1 Y100 FZ’ were entered to move the build plate. Z was equal to 100, 200 and 300. The distance and the corresponding time were measured to calculate the particular movement speed (n = 3). Values ranged between 1.63 ± 0.001 mm/s and 4.86 ± 0.000 mm/s (Figure 38, b) and showed a linear correlation ($R^2 = 0.99999$).

3.3.3. Residence Time Calculation based on a Plug Flow Model

First studies to determine the residence time distribution were conducted using F5 filaments punctually marked with methylene blue. The filament was extruded through the print head with command G1 E1500 F40, similar as in case of F-unit calibration. As the outlet filament was too thin for being analysed using the ExtruVis 3 system (ExtruVis, Germany), fractions were collected and quantitatively analysed in ethanol 70 % (w/w) via Vis-spectroscopy. Results were poorly reproducible as sampling of the outlet filament resulted difficult due to its high brittleness at a diameter of approximately 400 µm. Residence time calculations solely based on the pre-set printing speed (15 mm/s) were also performed. However, in both cases practical significance was questionable. Both methods neglected that during printing the print head also moved without extrusion of filament and that the filament was retracted several times. Retraction throughout the printing process was done automatically by the printer for instance before moving the print head without extrusion of filament.

Therefore, the residence time was determined based on a plug flow model [127] neglecting influences of turbulent flow and axial mixing, which are most likely to occur on front of the die. Using a plug flow model, determination of a particular residence time was feasible, but no residence time distribution.

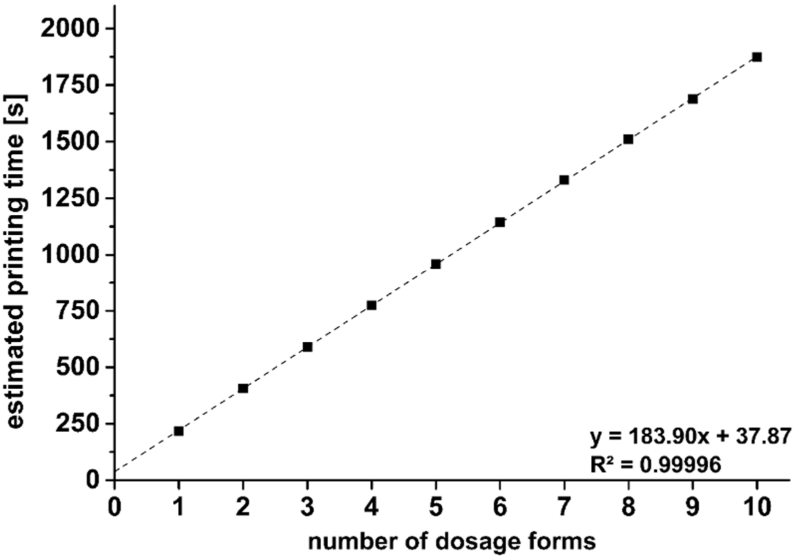

Figure 39. Estimated printing time for different numbers of dosage forms in one print job.

G-code information for printing of one to ten DDS (Figure 46) in one print job was determined based on the same adjustments as for section 3.4.3 (Table 13) and 20 % fill density. Printing speed was set to 15 mm/s. Besides the G-code file, the software provided the estimated printing time. It was used to build a linear correlation between the number of DDS and the estimated printing time (Figure 39). Y-axis intercept was considered as time for initializing procedures and movement of the print head prior to starting the print of the first DDS. For the evaluation of the residence time only the net printing time, meaning the calculated printing time minus y-axis intercept, was used. Mass per extrudate length (2.74 mg/mm; mean, n = 10) and mean mass of a DDS printed with these adjustments (423.7 mg; mean, n = 3; section 3.4.3) were used to determine the length of the extrudate required for one DDS (154.5 mm). As plug flow, the quotient of the required length of extrudate for printing one DDS and mean printing time per DDS (183.9 s, n = 55) was considered and determined to 0.84 mm/s. Sample size of 55 resulted from determined printing times for 10 + 9 + … + 1 DDS. Taking the different lengths of the hot ends into account ($l_{no.1}$ = 42.8 mm and $l_{no.2}$ = 57.86 mm; Figure 17) resulted in residence times of $t_{no.1}$ = 51 s and $t_{no.2}$ = 69 s. The same procedure was conducted using 50 mm/s and 90 mm/s as printing speeds since these were used in scientific publications dealing with FDM^{TM} of DDS [46, 47, 51, 53, 54, 59, 60, 62, 64, 121, 128, 129]. Due to a higher conveying speed, residence time declined. The results are presented in Table 7.

Table 7. Residence time inside the hot end of different print heads at different printing speeds.

		printing speed [mm/s]		
		15	**50**	**90**
printing time for one DDS [s] (mean ± sd; n = 55)		184.90 ± 0.77	67.48 ± 0.76	45.37 ± 0.72
plug flow [mm/s]		0.84	2.29	3.40
residence time [s] inside hot end	no.1	51	19	13
	no.2	69	25	17

These results clearly illustrated that not only the printing speed, but also the length of the hot end decisively influence the residence time inside the heated parts and thereby the thermal stress applied during the printing process. A short hot end and high printing speeds should therefore be preferred in case of dealing with thermally instable drugs. Even in the worst case with print head type II at 15 mm/s, a residence time of 69 s inside the heated print head is considerably low, compared to an MRT of ~642 s inside the heated extruder barrel. Yet, it should be also considered that printing temperature is usually higher than the extrusion temperature [15, 35, 58, 122]. During the present work (section 3.4.3), extrusion temperature for printable filaments was 160 °C whereas printing temperature was 180 °C. Nevertheless, according to van't Hoff et al. temperature increase of 20 °C might cause a four to nine times higher reaction rate [130]. Moreover, shear forces occurring during both processes (HME and FDM^{TM}) might lead to a locally increased temperature. Consideration of these aspects is therefore indispensable in case of working close to the degradation temperature of one of the chosen APIs or excipients.

3.3.4. Thermography of the Print Head

Thermographic measurements of print heads type I were conducted to estimate the highest temperature affecting the filament and to determine in which range temperatures fluctuated. To assess whether the filament actually reached this temperature during the process, temperature of the filament was determined as well. Further, different materials, PLA (glow in the dark, Prodim International, Netherlands), drug-free F2 and drug-loaded F3 filaments, were evaluated at different conveying speeds: F40, F100, F150, F200 corresponding to 12.1, 27.4, 36.1, 44.3 mm/s as printing speed. Single G-code commands for extrusion were used as described in section 3.3.2. Experiment design should enable analysing whether higher speeds impeded complete heating of the filament and whether different materials showed different temperatures due to varying heat capacities. Set temperatures for the extrusion differed due to the different materials and formulations. They were 170 °C for F2 and 180 °C for PLA and F3.

IR thermography as a contactless measurement method was considered suitable for temperature detection of heated objects in this case. From Kirchhoff's law Equation 2 was derived as follows [131]:

Equation 2. Modification of Kirchhoff's law.

$$1 = R + t + \varepsilon$$

R, t and ε represent the reflected, transmitted or emitted radiation by any object. Since most objects are opaque in the IR, t was considered 0 in these experiments. From that follows that the reflectivity and the emissivity are the two most decisive parameters. The higher the emissivity and the lower the reflectivity, the better a temperature of an object can be assessed using IR thermography. Emissivity of a blackbody is usually equal to 1. Reflectivity of polished metal surfaces, as in case of the die and the heating element of the print head, is very high resulting in emissivities of approximately 0.2 [131]. This makes temperature determination using IR thermography nearly impossible. However, this problem can be circumvented roughening the surface or painting it [131]. In literature, experiments are reported achieving an ε-value of 0.96 for painting of a copper surface in contrast to a polished copper surface and a roughened one with $\varepsilon = 0.03$ and $\varepsilon = 0.11$, respectively. Therefore, the print head was covered with matt brown colour during these thermographic studies.

As for polymers an emissivity equal to 1 could not automatically be assumed, a calibration modified from Seppala and Migler [123] was performed with API-loaded filament. Figure 40 displays the experimental setting using a hot stage. A cross-section and a small lengthwise positioned filament piece were placed on a cover glass and then placed on a hot stage. Part of the cover glass was painted with black colour as internal reference. Reference temperatures, temperature of the lengthwise positioned filament and its cross-section during the heating process are shown in Figure 41 (left). For both measurement fields (lengthwise and cross-section) a linear correlation ($R^2 > 0.999$ in both cases) with slopes close to 1 and small y-axis intercepts were found (Figure 41, right).

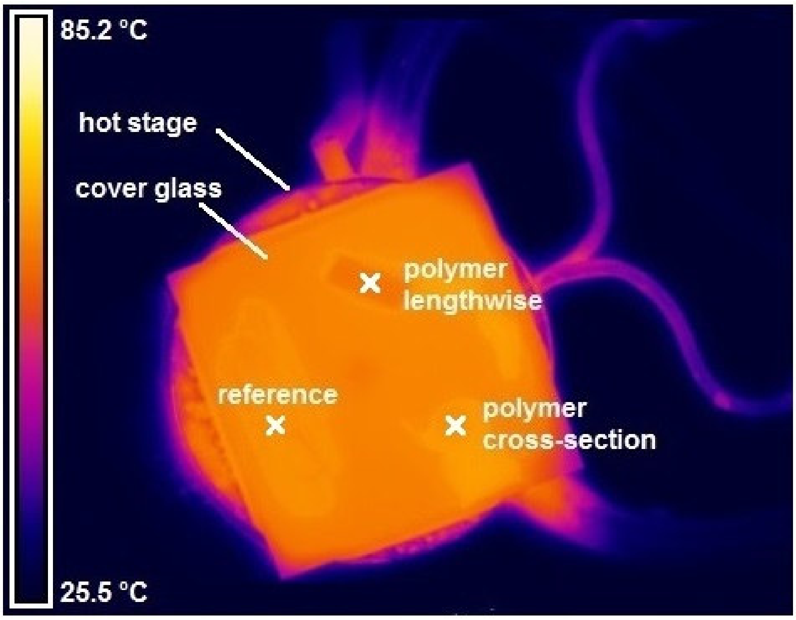

Figure 40. IR image of experimental setting used for calibration taken at 70 °C.

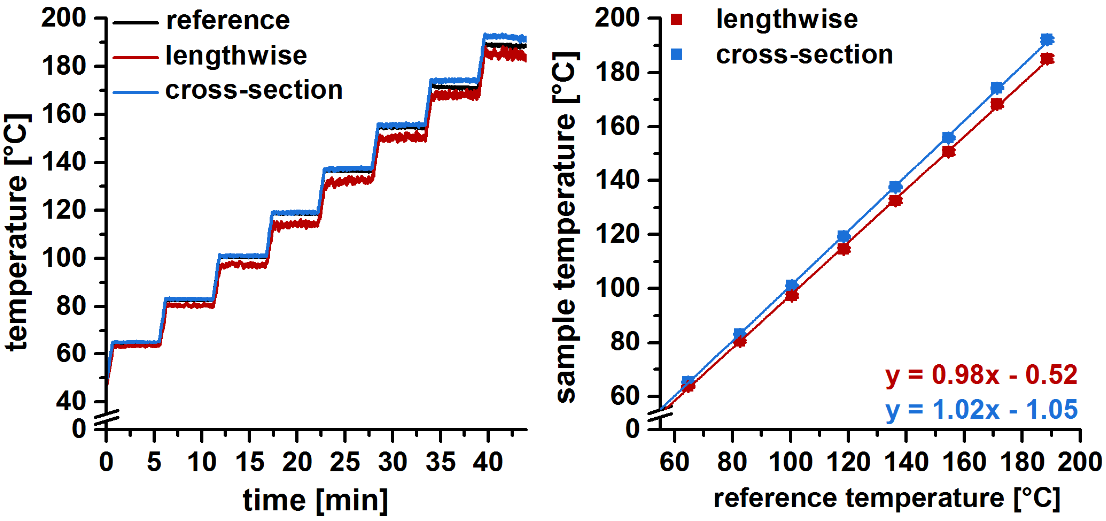

Figure 41. Applied temperature profile during calibration (left).
Sample temperatures against reference temperatures and linear correlation (n = 3000; mean ± sd) (right).

Temperatures taken from the lengthwise positioned filament were always below those of the cross-section (Figure 41, all), likely due to more pronounced cooling effects at the surface of the sample or insufficient contact of the sample with the cover glass. Therefore, the polymer cross-section was considered to generate data that were more reliable. Temperatures of the cross-section and the reference were superposable until 155 °C. Maximum deviations were 1.3 °C, whereas deviations at temperatures ≥ 160 °C were 3 °C and more. Since filament temperatures measured during thermography were below 155 °C, emissivity was considered equal to 1 and the calibration was not further utilized for evaluation of thermographic data.

Figure 42 shows an IR image of the print head and the outlet filament. Two different temperatures were recorded: the highest temperature at the print head as measure for the highest thermal load, which should be expected, and the filament temperature at the outlet. The measurement field for the determination of the maximum temperature of the print head is illustrated as rectangle in Figure 42. The filament temperature was measured directly below the die to minimize distortion of values due to cooling effects.

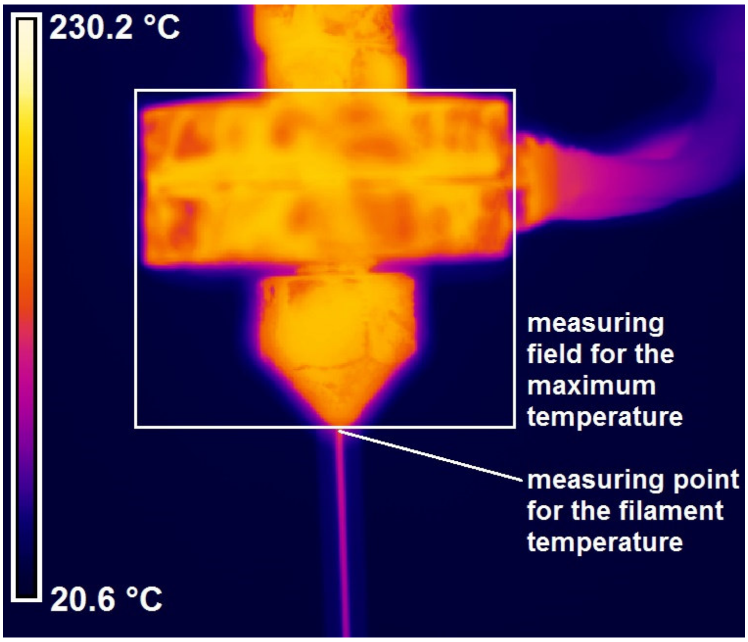

Figure 42. IR image of heat element (metal plates at the top) and tip of the print head during extrusion of a PLA filament. Measuring field for the maximum temperature of the print head and measuring point for the filament are illustrated.

Maximum temperatures of the print head were usually measured between the two metal plates close to the heating element. Temperatures over time are exemplarily displayed in Figure 43 for F3 at a set temperature of 180 °C and command G1 E1500 F100. Temperature values oscillated over time and consequently caused rejection of normal distribution in a Shapiro-Wilk test on a 0.05 significance level. Thus, common statistical parameters, e.g. arithmetic mean and standard deviation, had limited applicability and were not considered for data evaluation. Rather, the mean value, the period duration and the amplitude were determined in a fast Fourier transform (FFT). All measurements, regardless of the formulation, G-code command, temperature or point of measurement (print head or outlet filament), showed the same period duration of 52.25 s due to the implemented PI-controller. Between the periods of temperatures measured close to the heating element and the temperatures of the filament there was a time delay. Dashed lines in Figure 43 illustrate this effect. This was caused by the inertia within the heating system: heating and cooling due to regulation by the PI-controller appears at the heating element first and then at other areas of the print head.

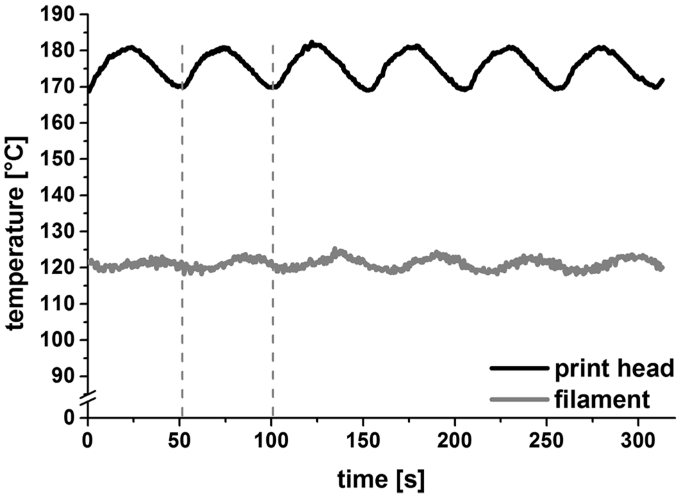

Figure 43. Maximum print head temperatures and filament temperatures of F3 with command G1 E1500 F100 (27.4 mm/s) and set temperature of 180 °C.

Figure 44 shows the maximum as well as filament temperatures and their relative difference determined via IR thermography. Mean maximum temperatures ± amplitude at the print head for a speed of 44.3 mm/s were 167.8 ± 3.9 °C for F2 and 176.7 ± 5.0 °C for F3 and, thereby, slightly below the set values of 170 °C for F2 and 180 °C for F3. For PLA a mean of 180.6 ± 8.3 °C was observed, which was close to the set temperature of 180 °C. However, the target values were in all cases enclosed considering the amplitudes as scattering parameter. Maximum temperatures consequently varied in a range of 8 to 16 °C around the mean value. Filament temperatures were below the maximum temperatures: in case of 44.3 mm/s as inlet filament speed F2 showed temperatures of 111.8 ± 0.8 °C, F3 of 120.3 ± 1.0 °C and PLA of 113.3 ± 2.4 °C. The amplitudes were smaller than those of the maximum temperatures. Temperature fluctuations observed for the print head were transferred to the filament expressed via the periodic oscillation (Figure 43). Nevertheless, the range of fluctuation was much less for the filament as the heat needed some time to be transferred to the filament. This was overlaid by the counter regulation of the PI-controller. Temperatures at the print head ranged between 10 to 16 °C around the mean. This was considered large, as properties of filaments can decisively change, but the impact on the filament temperature appeared to be rather low. They were in a range of ~5 °C around the mean. However, it should be considered that temperature measurements of the filament were performed directly below the die, which did not allow precise conclusions regarding the filament temperature in the zone of the heating element. Differences in temperatures found at the print head and the filament temperature were 12 to 15 % (Figure 44). Rapid cooling after passing the heating zone and insufficient time for entire heating were considered responsible for the rather large temperature differences. This means that thermal stress was overestimated by simply considering the set temperature since this might not be reached during the process or, most likely, only for a short period of time. Further, measurements revealed that the difference between maximum and filament temperature was dependent on the material. Comparing F3 filaments with PLA showed that temperature difference for PLA was larger (~12 % vs. 15 %) despite the same set temperature of 180 °C. Relative differences for F2 and F3 were similar (12-13 %) since the formulations only differed in 10 % anhydrous theophylline. However, a comparison was difficult in this case due to different set temperatures (170 °C vs. 180 °C) needed due to differences in physico-chemical properties. The results suggested that the extent of the thermal stress applied during the process was dependent on the material or most likely on its particular heat capacity at the working temperature as it strongly influences heating and cooling processes [61]. Nevertheless, relative differences detected in thermographic measurements for different materials might also appear due to different emissivities of the materials.

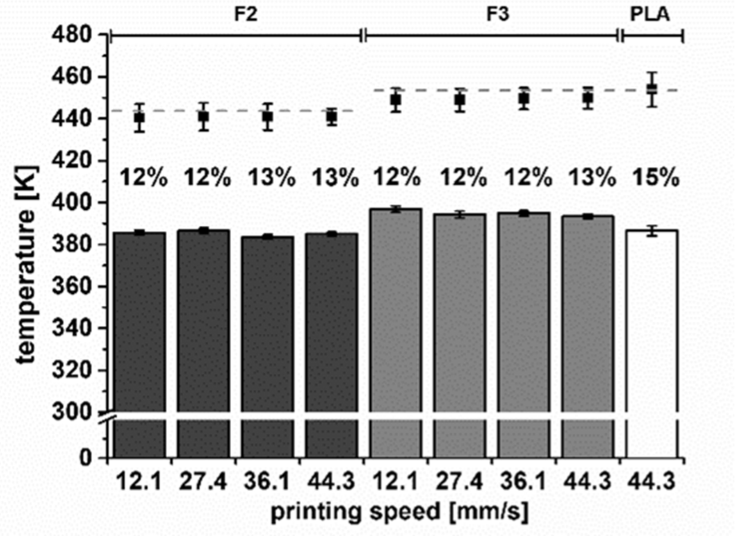

Figure 44. Maximum (squares) and filament temperatures (columns) determined via IR thermography (mean ± amplitude, FFT over 313 s, 2 Hz). F2, F3 and PLA indicate the material of the filament, numbers below the columns the printing speed. Percentages represent the relative difference between maximum and filament temperatures. Dashed lines mark the set temperature of the print head.

Last part of the study was analysing whether filament temperature was also influenced by the conveying speed through the print head. It was suspected that at higher conveying speeds the outlet filament was cooler, since the residence time close to the heating element was shorter and the filament was not entirely heated even at slow printing speeds (Figure 44). Printing speeds of 12.1 to 44.3 mm/s were analysed covering the applied printing speeds during production of DDS in this work (15 mm/s, section 3.4) and during other studies (< 45 mm/s) presented in literature [47, 58, 64]. Neither for F2, nor for F3, differences in the filament temperature depending on the printing speed was observed. The assumption, that a higher molar heat capacity of the API compared to the polymer ($C_{p,m}$ = 218.13 $J \cdot K^{-1} \cdot mol^{-1}$ [132] $C_{p,m}$ = 249.17 $J \cdot K^{-1} \cdot mol^{-1}$ [133] vs. $C_{p,m}$(Poly(methyl methacrylate)) = 186.19 $J \cdot K^{-1} \cdot mol^{-1}$ [134]) might have favoured insufficient heating of the filament passing the hot end at higher speeds, was not underlined in these experiments.

From print head thermography several important conclusions were drawn. Large temperature fluctuations (~16 °C) were found close to the heating element. This effect was less pronounced in the outlet filaments (~5 °C). Although 5 °C of temperature fluctuations was considered rather small, a PI-controller, which enables a more sensitive regulation, would improve this value. Temperature differences between the maximum at the print head and the filament were surprisingly high (52-67 °C) indicating fast cooling or incomplete heating of the filament inside the hot end. Further, the temperature of the filament in comparison to the maximum at the print head was dependent on the material. Inlet speed of the filament had nearly no impact on the filament temperature in the range of 12.1 to 44.3 mm/s, which represented realistic printing speeds. This could be considered positive, since the print head temperature would not have to be adjusted in case of speeding up the process, as e.g. in case of scale-up.

3.3.5. Thermography of the Build Plate

Thermographic measurements of the build plate were conducted to estimate thermal stress generated during the print while the unfinished objects remained on the build plate. This was covered with matt brown colour to minimize reflectivity of the material and, thereby, distortion of the measurement. The IR camera was positioned centrally above the build plate and the build plate moved during the recording. Thereby the whole length of the print bed could be measured from the back to the front (y-axis direction). Time-depending temperature data from the recording had to be converted into the corresponding position on the build plate using the calibration for the build plate movement from section 3.3.2. Figure 45 shows the determined values for the build plate from the back to the front. In the centre, temperatures were always ~10 % higher than the set temperature and fell sharply at the edges of the build plate. It was concluded that there was one centrally positioned heating element underneath the build plate. Thermal stress generated was consequently dependent at which position objects were printed. Interestingly, ~26 of 30.5 cm of the build plate were heated above the target temperature. So the target temperature was rather considered as minimum temperature. Although thermal stress generated by the build plate is comparatively low due to the low temperatures applied, it is higher than expected as the measured temperatures were always higher than the set values aside from the edges. Temperature profile in x-axis direction was not determined.

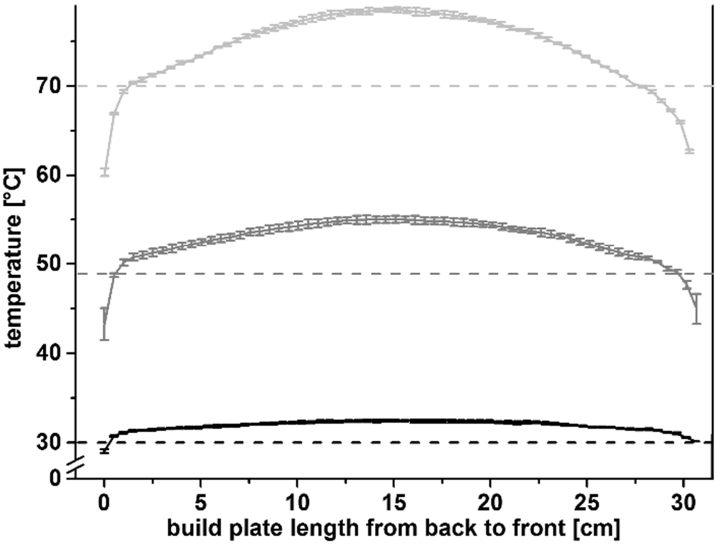

Figure 45. Temperatures of the build plate from the back to the front (n = 3, mean ± sd). Set temperatures (30, 50, 70 °C) for the particular data sets are marked with dashed lines.

3.3.6. Summary

Since FDM™ has not been an established process for DDS production in pharmaceutics yet, analysis of thermal stress was indispensable. To do so, thermographic measurements were applied and a theoretical determination of the residence time based on a plug flow model was conducted.

First, a calibration of the units of the F variable used in G-code had to be performed for the extrusion of the filament by the print head and for the build plate movement. These data was needed for accurate evaluation of thermographic data. The conveying speed for the outlet filament was linear in a range between 6.1 and 27.4 mm/s. Higher printing speeds from 36.1 to 44.3 mm/s lead to inaccuracies in the conveyance, indicated by increased standard deviations and non-conformance with the linear correlation found for slower printing speeds. The build plate movement was uniform and its speed was linearly dependent on the unit of the F variable in the investigated speed range.

Residence time inside the print head was found to be rather short (max. 69 s) compared to the HME process. By applying a short hot end and a fast printing speed this could even be decreased. Due to inaccuracies to be expected at higher printing speeds, the quality of the print should be evaluated carefully in that case. Print head thermography revealed that the printer was able to reach and maintain the target temperature, but with a fluctuation range of 16 °C in the worst case. However, temperature fluctuations found at the filament were only in a range of 5 °C. Generally, the filament temperature was 12 to 15 % below the maximum temperature at the print head. Relative difference between the print head and the filament temperatures were assumed dependent on the material, since the difference was higher for PLA than for F3 despite of the same set temperature of 180 °C. Molar heat capacity and, thereby, the time needed to be heated, was suspected to be the most important property in this regard. Different conveying speeds appeared to have a negligible influence on the filament temperature and the thermal stress.

Build plate thermography showed that temperatures were in all cases above the target temperature. This generated higher thermal stress than expected simply considering the set temperature. Since the printed DDS remains on the build plate during the whole print, printing time is important. This could be shortened by increasing the printing speed or by printing only one DDS in one print job. Printing several DDS in one print job might be functional, but increases the time every dosage form has to remain on the build plate.

Summarizing the present findings, it was stated that thermal stress in FDM^{TM} was comparatively low considering the HME process for filament production due to the shorter residence time. However, in case of dealing with a thermally instable drug, polymers, which can be processed at low temperatures and which have a high heat capacity, would be preferred. Further, higher printing speeds and production of one DDS in one print job can be recommended to decrease thermal load.

3.4. Printed Network Structures as Dosage Forms

3.4.1. Pretext

Essential contents of this chapter are based on the research article “3D-Printed Network Structures as Controlled-Release Drug Delivery Systems: Dose Adjustment, API Release Analysis and Prediction” previously published in the AAPS PharmSciTech special issue about printing and additive manufacturing (DOI: 10.1208/s12249-018-1017-0) by Carolin Korte and Julian Quodbach. Texts have been linguistically adapted and the content was extended by further data.

3.4.2. Introduction and Objectives

The final goal of the present work was the development of a dosage form produced via FDM^{TM}, which enabled predictable and sustained drug release. Further, the combination of filaments with different release properties printed in one dosage form was evaluated.

It has already been shown that differences in surface/mass ratio decisively influences the drug release from sustained-release matrices [15]. This led to the idea to create a dosage form with a similar surface/mass ratio, in case the dose is changed. Three-dimensional network structures were considered to solve this problem. Based on the assumption that all branches of the network have the same size and thickness, varying the dose by varying the network density should enable a constant surface/mass ratio, or rather a constant specific surface area (SSA). If uniform perfusion of the network was enabled, prediction of drug release should be feasible.

Other authors have already studied printing varying fill densities for dose adjustment. Drug release has also been analysed [37, 51]. However, in these cases, the network was only an internal structure and was not presented to the dissolution medium, since it was used as scaffold structure inside the dosage forms. These were closed from all sides. Other studies, which evaluated network structures without (entire) shell did not intend to vary doses by varying the fill density or to perform drug release prediction [65, 88]. Thus, the present work united several approaches from literature to create a novel solid dosage form with predictable sustained drug release, despite of varying the drug dose.

Printing of different filaments in one dosage form has been shown to be feasible in literature. This might be desired for the combination of different drugs or for the combination of different release profiles for one drug. The aim of the present study was to generate a biphasic dissolution profile, which could be predicted based on dosage forms printed with one formulation. Hence, two filaments, enabling different drug release of theophylline, were combined in one dosage form and API release prediction was performed.

3.4.3. Dosage Forms Consisting of Single Filaments

3.4.3.1. Production of Dosage Forms

The previous sections mainly focused on examination of F5 filaments and their production process. In printing studies, F5 and F10 filaments were included. They were printable and had the same composition, except for 7 % of solid plasticizer, which was SA for F5 and PEG4000 for F10. Therefore, they were supposed to exhibit different release behaviours. F5 and F10 filaments were printed into dosage forms displayed in Figure 46 (n = 10) with different fill densities (10, 15, 20, 25, 30 and 40 %) using print head type I. The shape of an oblong tablet was exemplarily chosen and designed as CAD model (Figure 46, left). To ensure proper handling during analysis, large dimensions were chosen (20 x 10 x 5 mm), although printed DDS might be too large for oral administration. The inner network structure was created via slicer adjustments (section 5.5.2.3). Thereby, depicted dosage forms were generated (Figure 46, right). All dosage forms of one kind (filament and infill) were produced in one print job.

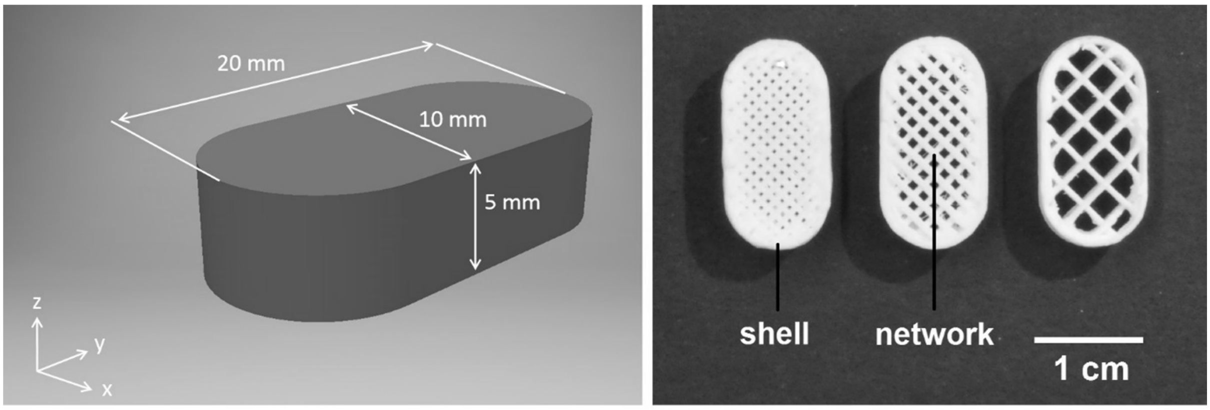

Figure 46. CAD model of printed DDS (left). Top view of printed DDS (F5) with internal network structures of different densities 30, 20, 10 % (right, modified from [135], by courtesy of Springer Nature).

All dosage forms consisted of a shell and an internal network printed of the same matrix. However, neither the internal network nor the shell could be printed independently, since they were too brittle and reliable separation from the build plate was not possible. This might not be the case for more resilient filament formulations, e.g. containing PVA (F15, Figure 21).

Printing times for the dosage forms with different fill densities are listed in Table 8. These were determined using the slicer software with the adjustments presented in Table 13. Therefore, a measure of variation could not be determined. Dosage forms with higher fill densities needed longer printing times, since more material had to be extruded by the print head. Printing times for F5 and F10 filaments were the same, as the settings, which determined the G-code file and consequently the printing were identical.

Table 8. Printing time of dosage forms with different fill densities.

	infill [%]					
	10	15	20	25	30	40
printing time per dosage form [s]	130	167	185	218	243	294

3.4.3.2. Physical Properties

Keeping constant the dimension of the printed DDS, the mass, and consequently the dose, increased with increasing fill density. Between these two parameters, a linear correlation was found for both formulations with a coefficient of determination ≥ 0.9967 (Figure 47). Masses varied between 260 and 706 mg, corresponding to 78 and 212 mg theophylline, showing the feasibility of dose adjustment via infill variation. Relative standard deviations were below 3.7 %, indicating a good mass precision. F10 DDS, however, always exhibited a higher mass than F5 DDS. This might be due to different quality of conveyance inside the print head caused by different surface structures. Another explanation might be a different density of the plasticizers. Based on the linear correlations, y-axis intercepts were considered as mass of the shell, corresponding to 0 % fill density. They were 120.63 mg for F5 and 134.32 mg for F10.

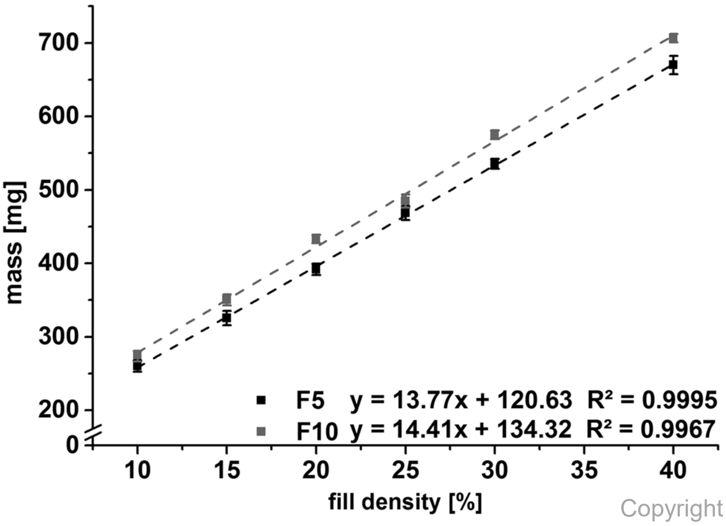

Figure 47. Mass against fill density of printed dosage forms with filaments F5 and F10 (n = 10; mean ± sd) (modified from [135], by courtesy of Springer Nature).

Furthermore, printed dosage forms were analysed using X-ray microcomputed tomography. Obtained images are exemplarily shown for F5 printed dosage forms in Figure 48. They were capable to reveal the inner structure of the printed dosage forms. Figure 48 (a and b) shows slices of an uneven and an even layer. It was illustrated that branches (Figure 48, c) creating the mesh are shifted by 90 degrees in the different layers. The branches are fully dispersed into air, except for the contact points to the proximate layers (Figure 48, c). Conservative pharmaceutical down-streaming processes for extruded matrices, as e.g. tableting or injection moulding, would hardly be capable to produce these sophisticated structures [8].

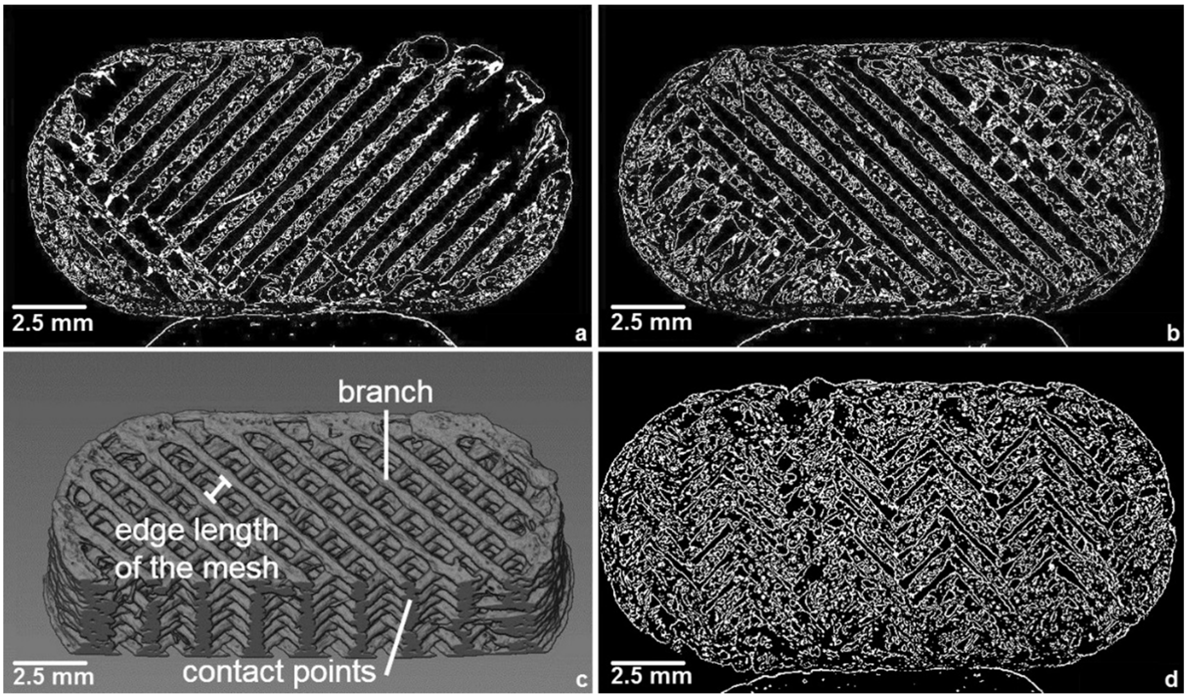

Figure 48. X-ray image of printed dosage forms. (a) Slice of an uneven and (b) of an even layer of a 30 % fill density dosage form. (c) 15 % fill density dosage form with terminology explanation. (d) Slice of a 40 % fill density dosage form (modified from [135], by courtesy of Springer Nature).

In addition, X-ray microcomputed tomography was used to determine the surface areas and the edge lengths of the created meshes. Although the shape of the dosage form appeared rather simple, calculation of the surface did not lead to results comparable with those obtained via X-ray microcomputed tomography. The roughness of the surface (Figure 48) was considered as main reason for this discrepancy. The edge length of the mesh decreased with increasing fill density. Figure 48 d reveals that DDS with 40 % fill density did not exhibit clear meshes, since branches were printed so close together that they touched each other axially. For this reason, these DDS were not analysed further regarding surface area. 40 % fill density was therefore considered as outside of the upper limit of the experiment. Results for the surface areas are displayed in Figure 49. As expected, the surface area increased with increasing fill density. Surface areas were between 18.2 cm² (F5, 10 %) and 47.1 cm² (F10, 30 %). For both formulations, a linear correlation of fill density and surface area was observed with 10.69 cm² (F5) and 17.47 cm² (F10) as y-axis intercepts, representing the surface areas of the shells. F10 printed formulations always exhibited higher values for the surface area. As in case of mass values, reasons for these differences might be differences in conveying performance of the filament. Further, a larger surface might result from a rougher filament leaving the printer nozzle, e.g. in case of melt fracture.

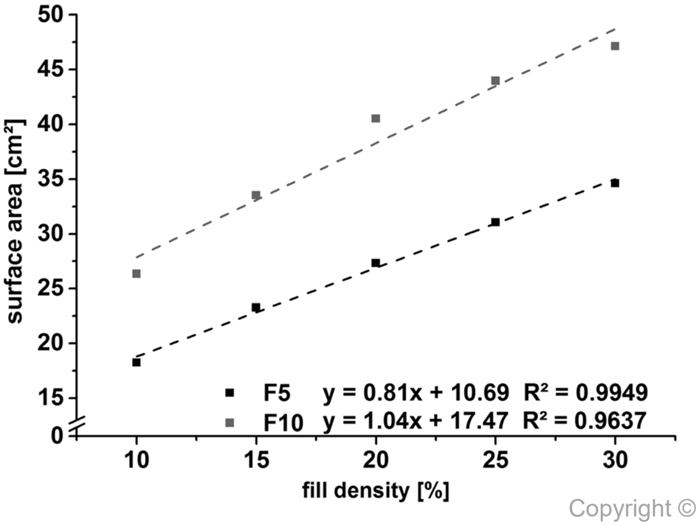

Figure 49. Fill density and corresponding surface areas of printed dosage forms determined via X-ray microcomputed tomography (n = 1) (modified from [135], by courtesy of Springer Nature).

Based on surface data, the SSA for the network without shell was calculated (Table 9). In order to do so, surface areas and masses of the internal network were determined as difference between the value for the whole dosage forms and extrapolated values for the shell (120.63 mg/134.34 mg and 10.69 cm²/17.47 cm²). The resulting SSA for the network varied only in a small range for fill densities of the same formulation (Table 9). This finding underlined the assumption, which was proposed at the beginning: due to the same size of the branches in all cases, the SSA for the internal network structure was nearly constant.

Table 9. SSA for the network [cm²/g] of printed DDS (n = 3 for mass; mean ± sd) (modified from [135], by courtesy of Springer Nature; Copyright © 2018 Springer Nature).

	10 %	**15 %**	**20 %**	**25 %**	**30 %**
F5	56.74 ± 0.06	56.91 ± 1.22	59.59 ± 1.15	58.51 ± 0.56	58.25 ± 0.48
F10	72.91 ± 0.08	73.14 ± 1.57	76.58 ± 1.48	75.19 ± 0.71	74.86 ± 0.62

3.4.3.3. Dissolution Studies

Printed dosage forms were subjected to drug dissolution studies. Due to their extraordinary shape and flotation in the dissolution medium, a suitable dissolution set up had to be developed in advance.

First preliminary studies were conducted using a United States Pharmacopoeia (USP) apparatus type I. Minimal swelling of the matrix during dissolution studies caused tilting of the DDS inside the basket (Figure 50). This, however, inhibited uniform perfusion of the whole surface with the dissolution medium. Therefore, large differences in the dissolution curves were found, depending of the orientation of the DDS inside the basket and the results were not reliable.

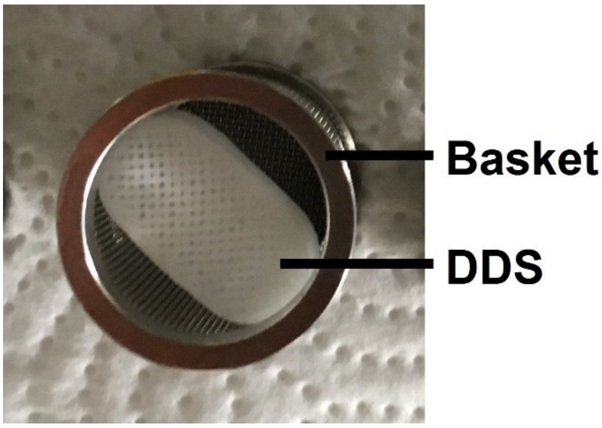

Figure 50. Dissolution basket with tilted DDS after 24 h of dissolution testing.

Thus, the flow-through cell was evaluated regarding its suitability in consecutive dissolution studies. The DDS were embedded into glass spheres to ensure correct positioning inside the cell. Obtained curves, however, did not provide consistent information, if different infills were compared. In this case, a slight swelling of the matrix [76] and, thereby, increase of pore size of the DDS, caused that the glass spheres could penetrate and clog the pores. As a consequence, uniform perfusion with the dissolution medium was no longer given. In particular, DDS with higher fill densities and smaller pore size were affected. DDS with low densities had larger pores, which were not clogged by the glass spheres. This effect is exemplarily displayed in Figure 51 for DDS with 30 % and 20 % fill density. After dissolution, DDS appeared larger due to swelling of the matrix. For 30 % fill density, pores could hardly be examined after dissolution analysis (Figure 51, b), since they were entirely closed by stuck glass spheres.

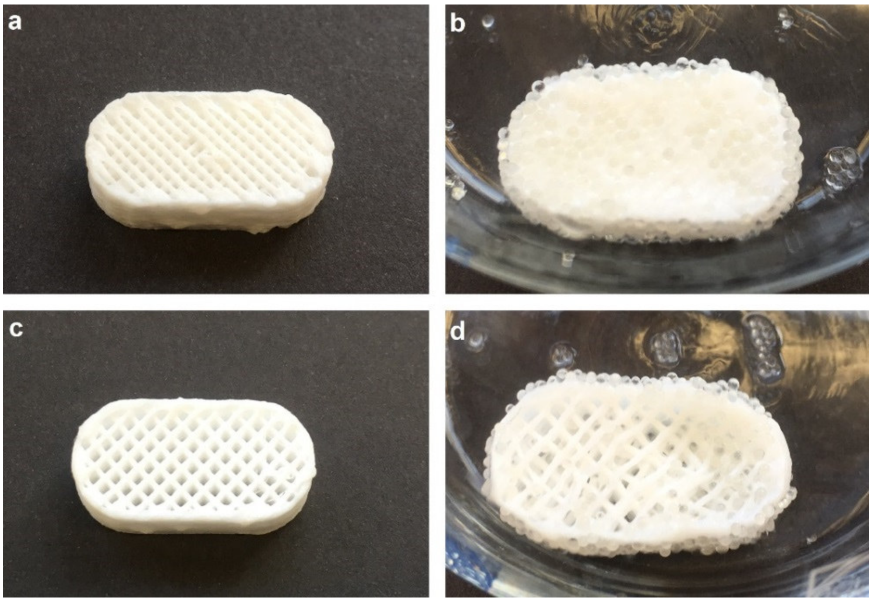

Figure 51. F5 30 % (a) and 20 % (c) fill density DDS before dissolution analysis. F5 30 % (b) and 20 % (d) fill density DDS after dissolution analysis in a flow-through cell.

To overcome these difficulties, special sinkers were developed, allowing central and vertical positioning of the DDS at the vessel bottom in a USP-II apparatus and, thus, uniform perfusion of the pores by the dissolution medium (Figure 52). The DDS were fixed in the sinker by a flexible clasp. A teflon disk ensured an upright position of the DDS and impeded floating during the test.

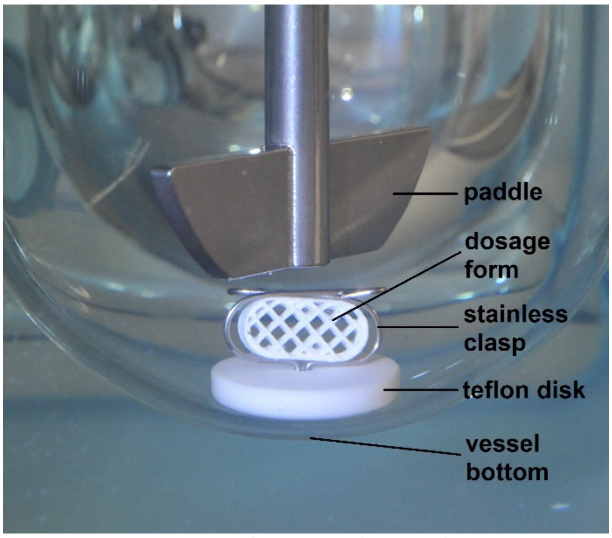

Figure 52. Vessel of an USP-II apparatus with DDS fixed in sinkers (modified from [135], by courtesy of Springer Nature).

Other conditions of in-vitro dissolution studies were chosen according Test 6 of USP 39 monograph *Theophylline Extended-Release Capsules*. A USP-II apparatus was used with a paddle rotation speed of 100 rpm and 1000 mL of 0.05 M phosphate buffer at pH 6.6 and 37.0 ± 0.5 °C. Quantitative determination of the API concentration was performed at 271 nm. 40 % fill density dosage forms were not considered, since meshes of the internal network were not clearly exhibited. For reasons of clarity, the number of data points depicted in dissolution curves was reduced from 50 to 17. Results from in-vitro dissolution studies are illustrated in Figure 53. Both formulations show changes in drug release depending on the fill density, whereby gradual shifts were more obvious for F5. High fill densities tended to release slower than low densities. Of course, this was only true considering the relative amount of released API, since DDS with higher fill densities had a higher total amount of API. During in-vitro dissolution testing, all DDS released >90 % of the incorporated API within 24 h. Both formulations, however, contained the same amount (7 %) of plasticizer. Comparing DDS with the same infill density but different formulation, for F5, containing SA, a considerably slower drug release was determined. This observation was explained with differences in water solubility of SA and PEG4000. SA is classified as insoluble [84], whereas PEG4000 is considered very soluble [85] according to the Ph. Eur. PEG4000 was thereby able to form pores and facilitate API release in comparison to SA [86]. $F10_{10\%}$ and $F10_{15\%}$ even met the USP requirements for immediate release theophylline capsules (> 80 % of theophylline release within 60 min), whereas $F5_{10\%}$ and $F5_{15\%}$ only released 45 and 35 %, respectively.

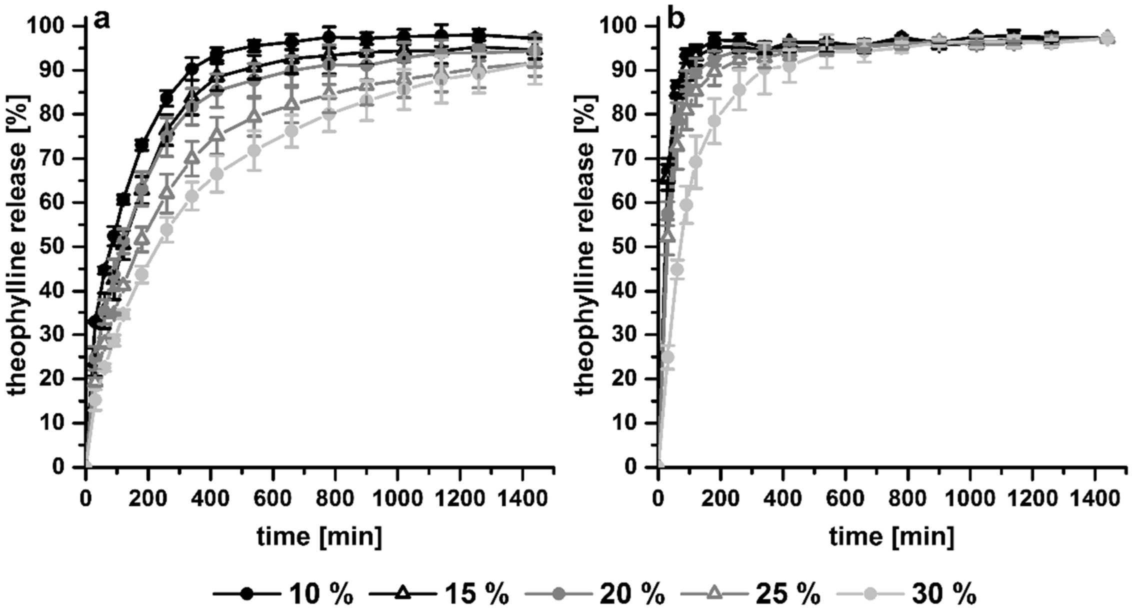

Figure 53. Dissolution curves of DDS with fill densities from 10 to 30 % printed with F5 (a [135], by courtesy of Springer Nature) and F10 (b) filaments (n = 3, mean ± sd; 37 ± 0.5 °C, 100 rpm, 1000 mL phosphate buffer 0.05 M pH = 6).

The time after 50 % theophylline release was compared to market products. Dissolution data for extended-release capsules containing coated pellets and sustained-release tablets were evaluated by Knop et al. [78, 136]. Experimental settings were the same (medium, apparatus, rotation speed, wavelength) as for the printed dosage forms, with the exception that capsules were tested in a basket apparatus. Results are displayed in Figure 54. Times for 50 % drug release were higher for the matrix tablets than for the capsules with coated pellets, which released all API when cracks in the film were formed. The matrix, however, stayed intact and thereby enabled a more sustained release. This also applied for the printed matrices. Comparing the values of market products to those of the printed dosage forms showed that all printed ones were in the range between 12 min (Theophyllin HEXAL®) and 653 min (Solosin®). Sustained release from printed dosage forms was better than for the coated pellets but worse than for the matrix tablets. Commercial tablets consisted of an HPMC or HEC matrix. Swelling and gel-forming at the surface led to a more distinct sustained release than the extruded aPMMA matrix. Nevertheless, printed dosage forms, especially in case of F5, were comparable to market products considering the time for 50 % drug release. However, market products contained 270 to 350 mg of theophylline, which was more than the printed ones (78 - 160 mg).

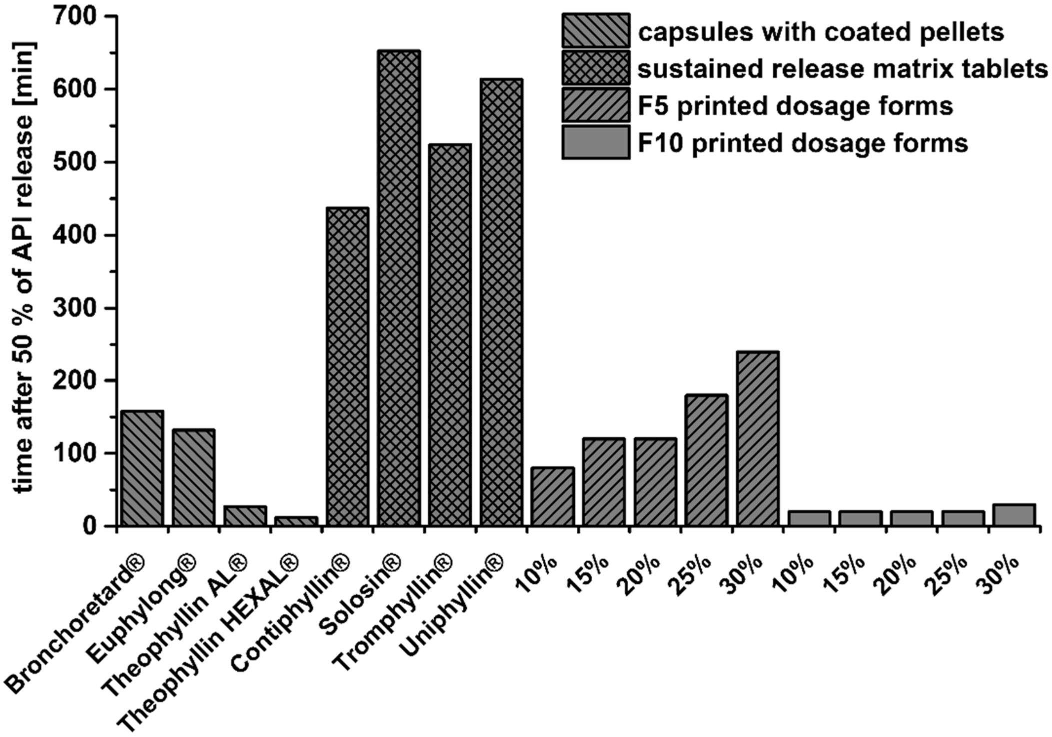

Figure 54. Time after 50 % of theophylline was released from eight different market products and F5 and F10 printed dosage forms with different fill densities (n = 3; mean).

In-vitro dissolution studies clearly indicated that F10 as PEG4000 containing formulation was not capable to maintain sustained-release properties of the matrix due to pore forming properties (Figure 53 and Figure 54). Pronounced differences in dissolution properties of different formulations F5 and F10 were considered positive for studies, in which a biphasic dissolution profile should be achieved (section 3.4.4). However, prediction of immediate release was not reasonable or beneficial. For this reason, the following part of the section focused on F5 printed solid dosage forms.

3.4.3.4. Modelling of 0 % Fill Density Dissolution Curve

As previously stated, neither printing of the shell nor of the infill solely was feasible. Consequently, the shell and the infill were printed in every case, which was cumbersome for the examination of the network dissolution properties. Due to edge effects, release from infill and shell might also show a different kinetic and was therefore indispensable to eliminate. For the evaluation, a 0 % fill density dissolution curve was modelled. A different drug distribution in shell and infill was considered unlikely, as the drug was homogeneously distributed along the filament (section 3.2.4.1) and shell and infill were printed simultaneously.

Since mass and surface area correlated linearly with the fill density, it was assumed that linear correlations might also exist for the dissolution profiles. Hence, for every time point, a linear fit was calculated based on dissolution data of dosage forms with 10 to 30 % fill density. The procedure is exemplarily illustrated in Figure 55 for time points 60, 120 and 240 min. Extrapolation to the y-axis provided corresponding relative amount of released API from the shell for the time point ($M_{t,rel,0\%}$). After 260 min, calculated values were greater than 100 % for the shell. The release of theophylline from the shell was considered completed and therefore assumed constant after 260 min.

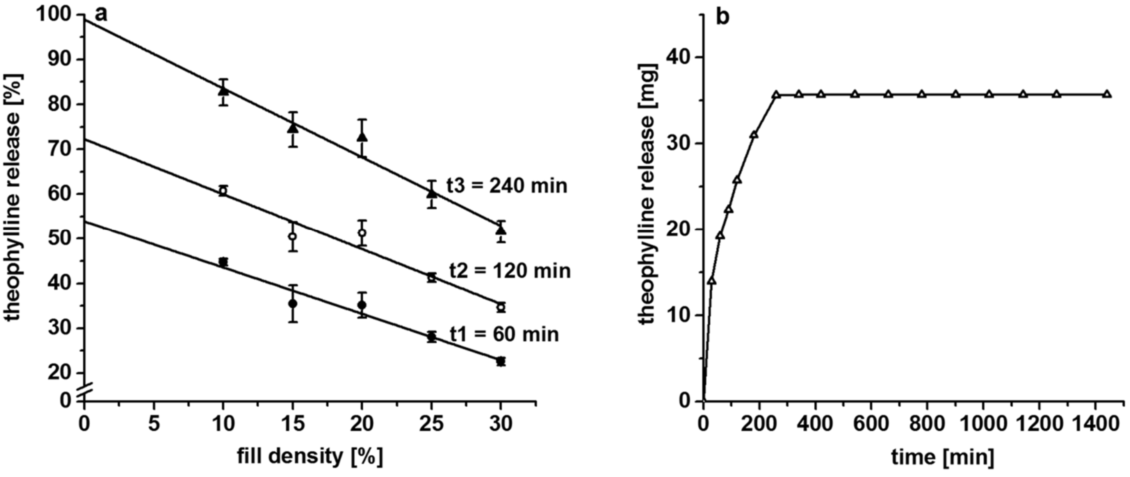

Figure 55. (a) Linear extrapolation for different time points (n = 3; mean ± sd). (b) Modelled 0 % fill density dissolution curve for absolute amount of API (a: modified figure, b: adopted figure, both from [135] by courtesy of Springer Nature).

Taking the mass of the shell (m = 120.6 mg) and its API load of 30 % into consideration, dissolution curve for the absolute amount of released API ($M_{t,0\%}$) was modelled using Equation 3 (Figure 55, b).

Equation 3. Calculation of absolute amount of released API from the shell [135].

$$M_{t,o\%} = \frac{M_{t,rel,0\%}}{m} \cdot 30\%$$

All further data evaluations and predictions were performed based on differential curves ($M_{t,net}$) of the measured released amounts (M_t) and the modelled ones for 0 % fill density (Equation 4).

Equation 4. Calculation of released total amount of API from the network [135].

$$M_{t,net} = M_t - M_{t,0\%}$$

3.4.3.5. Dissolution Data Analysis using Korsmeyer's and Peppas' Approach

Differential curves, describing the drug release solely from the internal network, were subjected to a kinetic analysis based on Korsmeyer's and Peppas' approach. This enabled distinction between release according to zero order and square root of time kinetics [137]. Based on Equation 5, dissolution kinetics were analysed [138]:

Equation 5. Fractional drug release as a function of time.

$$\frac{M_t}{M_\infty} = kt^n$$

M_t/M_∞ represents the fractional theophylline release, which is dependent on time t. Constant k describes geometrical and structural properties of the dosage form, whereas n, also called diffusional release exponent, refers to the underlying diffusion mechanism. Linearization of Equation 5 was achieved applying the common logarithm:

Equation 6. Linear form of Equation 5 [135].

$$log_{10}\left(\frac{M_t}{M_\infty}\right) = log_{10}k + n \cdot log_{10}t$$

Figure 56 shows the double logarithmic depiction of theophylline release with corresponding linear fits and the diffusional release exponent according to Equation 6. Values >18 % were considered until the linear range in the double logarithmic depiction was covered. Dosage forms with higher fill density tended to exhibit higher diffusional release exponents. According to Ritger and Peppas, in cylindrical shaped matrix systems values for the diffusional exponent n = 0.45 indicate a release following a square root of time kinetic and n = 1 a zero order kinetic [137, 138]. 10 % fill density dosage forms, with n = 0.49, showed a release following a square root of time kinetic. The diffusional release exponents of the other dosage forms, however, suggest a hybrid between square root of time and zero order kinetic (n ≥ 0.58). The applicability of the mentioned thresholds was limited, since one branch of the network might be considered as cylinder but the contact points impaired this approximation.

Nevertheless, under the assumption that theophylline has not dissolved but entirely suspended in the polymer matrix, which showed swelling but no gel-forming or erosion [76], kinetics following a root of time were expected. For 10 % fill density, this expectation was fulfilled. For higher fill densities, on the other hand, square root of time kinetic could not be confirmed. With higher fill densities, the edge length of the mesh decreased resulting in smaller pores. This effect might even be more pronounced, as the matrix showed pH-independent swelling during the dissolution and the sinker inhibited enlargement of the whole dosage form by the clasp (Figure 52). Consequently, uniform perfusion was not ensured at higher fill densities during in-vitro dissolution studies. This led to a slower release (Figure 53) and gradual changes in release kinetic (Figure 56). Another reason for the different behaviour might be, that the diffusivity of the API in the matrix (D) is time dependent and also dependent on the particular position of the drug particle within the system [139]. Calculations regarding the drug release from the shell and increasing contact points of the network branches with increasing fill density included further uncertainties and might cause results not complying with the root of time kinetic.

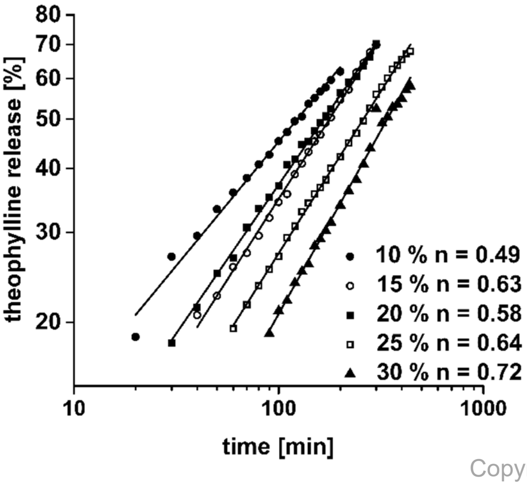

Figure 56. Double logarithmic depiction of theophylline release from the internal network of F5 printed dosage forms (> 18 % release; n = 3; mean) (adopted from [135], by courtesy of Springer Nature).

3.4.3.6. Prediction of Dissolution Based on Higuchi Model

For 10 % fill density dosage forms, a release following a square of root of time kinetic was found and, consequently, Higuchi's model appeared to be valid. Therefore, this model was evaluated as mean for API release prediction of dosage forms with different infills. Higuchi's model, first described for release of suspended drugs from ointments and later shown to be equally valid for a drug release from homogeneous planar polymer matrices [140, 141], is expressed via the following equation:

Equation 7. Drug release per unit of exposed area as function of time [141].

$$Q = \frac{M_t}{A} = \sqrt{D(2C_0 - C_s)C_s t}$$

Q represents the amount of API released in time t (M_t) per unit area (A). D is the diffusivity of API in the polymer matrix, C_0 the initial and C_s the saturation concentration. Since only F5 printed dosage forms were subjected to analysis using Higuchi model, D, C_0 and C_s were the same for the dissolution experiments. Thus, simplification to Equation 8 was feasible:

Equation 8. Simplification of Equation 7 [135].

$$M_t = D_k A\sqrt{t} \text{ , with } \frac{Q}{\sqrt{t}} = D_k$$

Hence, D_k, combining the diffusivity, initial and saturation concentration of theophylline in the polymer matrix, was determined as slope in a Higuchi plot (Q against $\sqrt{t}$) based on data of 10 % fill density dosage forms, following Equation 8 (Figure 57). Calculation of Q was performed using the released amount of API at each time point and the surface area determined via X-ray microcomputed tomography. Although the surface might change marginally due to swelling during the in-vitro dissolution analysis, linear correlation in the Higuchi plot was satisfactory ($R^2 = 0.9993$) and D_k could be determined to $0.2113\ \mathrm{mg{\cdot}cm^{-2}{\cdot}min^{-0.5}}$.

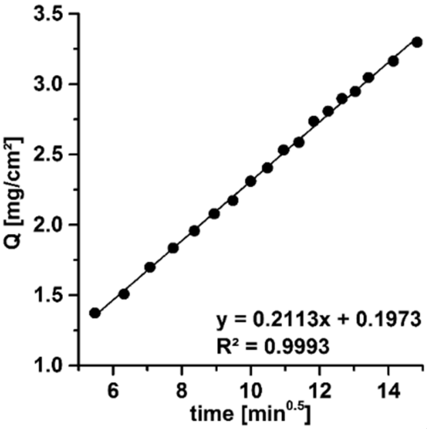

Figure 57. Higuchi plot of theophylline release from F5 printed dosage forms with 10 % fill density (n =3; mean) (adopted from [135], by courtesy of Springer Nature).

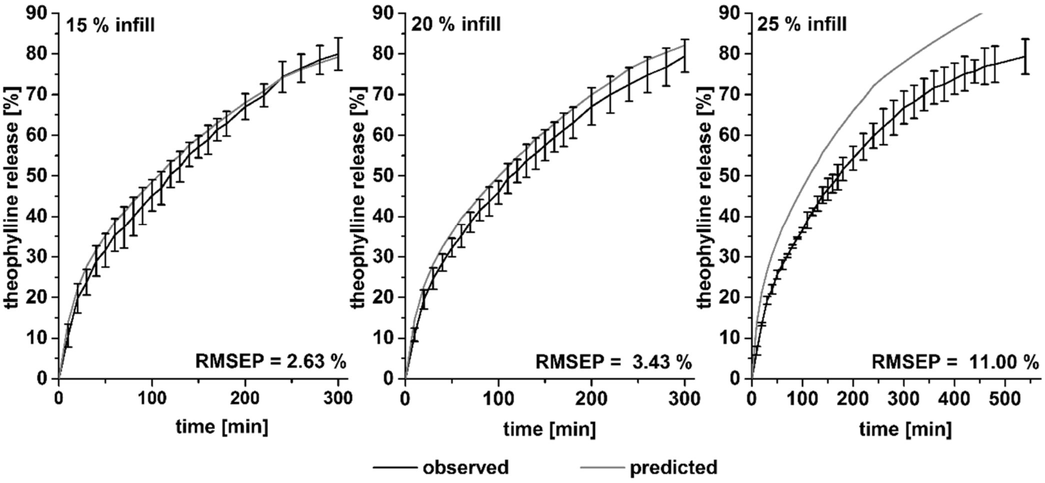

Figure 58. Observed (n = 3, mean ± sd; 37 ± 0.5 °C, 100 rpm, 1000 mL phosphate buffer 0.05 M pH = 6) and predicted dissolution curves for F5 dosage forms with fill densities of 15, 20 and 25 % including particular RMSEP values.

Using $D_k = 0.2113\ \mathrm{mg \cdot cm^{-2} \cdot min^{-0.5}}$ and the particular internal network surface of the dosage forms, the released API amount from the internal networks with different density was calculated for every time point based on Equation 8. Afterwards, the determined API amount solely released from the shell (Figure 55, b) was added for every time point and divided by the total API content of the particular dosage form. Values until 80 % drug release were considered. Observed and predicted curves for the drug release are displayed in Figure 58. The increasing discrepancies between observed and predicted curves with increasing fill density were also reflected in increasing root mean square error of prediction (RMSEP) values. This result was expected, since the applied model assumes a release following a root of time kinetic and diffusional release exponents ≥ 0.58 indicated a hybrid of zero order and square root of time kinetic. Further, D_k is dependent on the position of the particle in the matrix and time dependent, since diffusion paths of later released particles differed from those released at an early time point [139]. Although utilization of the Higuchi model might be an attractive approach, since only one data set is needed for prediction, applicability was very limited in the present case and, therefore, not considered suitable.

3.4.3.7. Prediction of Dissolution Based on Linear Inter- and Extrapolation

Considering gradual changes in dissolution behaviour and feasibility of linear extrapolation for determination of drug release from the shell (Figure 53 and Figure 55, a), linear interpolation between 10 and 30 % fill density was examined for modelling of dissolution curves. The calculated relative values for the drug release from 10 and 30 % fill density networks were used to build a linear regression. Released API from networks with densities from 15 to 25 % was calculated based on the determined regression. After converting these values into absolute ones, API release from the shell was added and finally related to the total theophylline amount. Resulting predicted curves are displayed in Figure 59, a-c.

The predicted curves are enclosed by the observed ones and their standard deviation for nearly all time points (Figure 59 a-c). Quality of the prediction was also reflected in the observed vs. predicted plot (Figure 59, d) and corresponding RMSEP values (Table 10). The RMSEP for dissolution of 20 % fill density dosage forms was slightly higher (3.70 %) than for 15 % (2.18 %) and 25 % (1.40 %). Figure 53 shows, that dissolution curve of 20 % fill density dosage forms did not fully comply with expectations based on values obtained for the other dosage forms. Values obtained, especially in the first half, were higher than estimated. Considering the single curves revealed that two curves were very similar and one deviated to higher values. Using the mean values of the two similar curves for data evaluation resulted in a lower RMSEP of 2.05 %.

Besides interpolation, also extrapolation based on data of 10 and 15 % or on 25 and 30 % fill density, was carried out for prediction of dissolution curves. However, worse RMSEP values resulted, in particular for prediction based on 10 and 15 %. Reason for this might be that relative increase in mass from 10 to 15 % was higher than for 25 and 30 %. This caused higher statistic uncertainties.

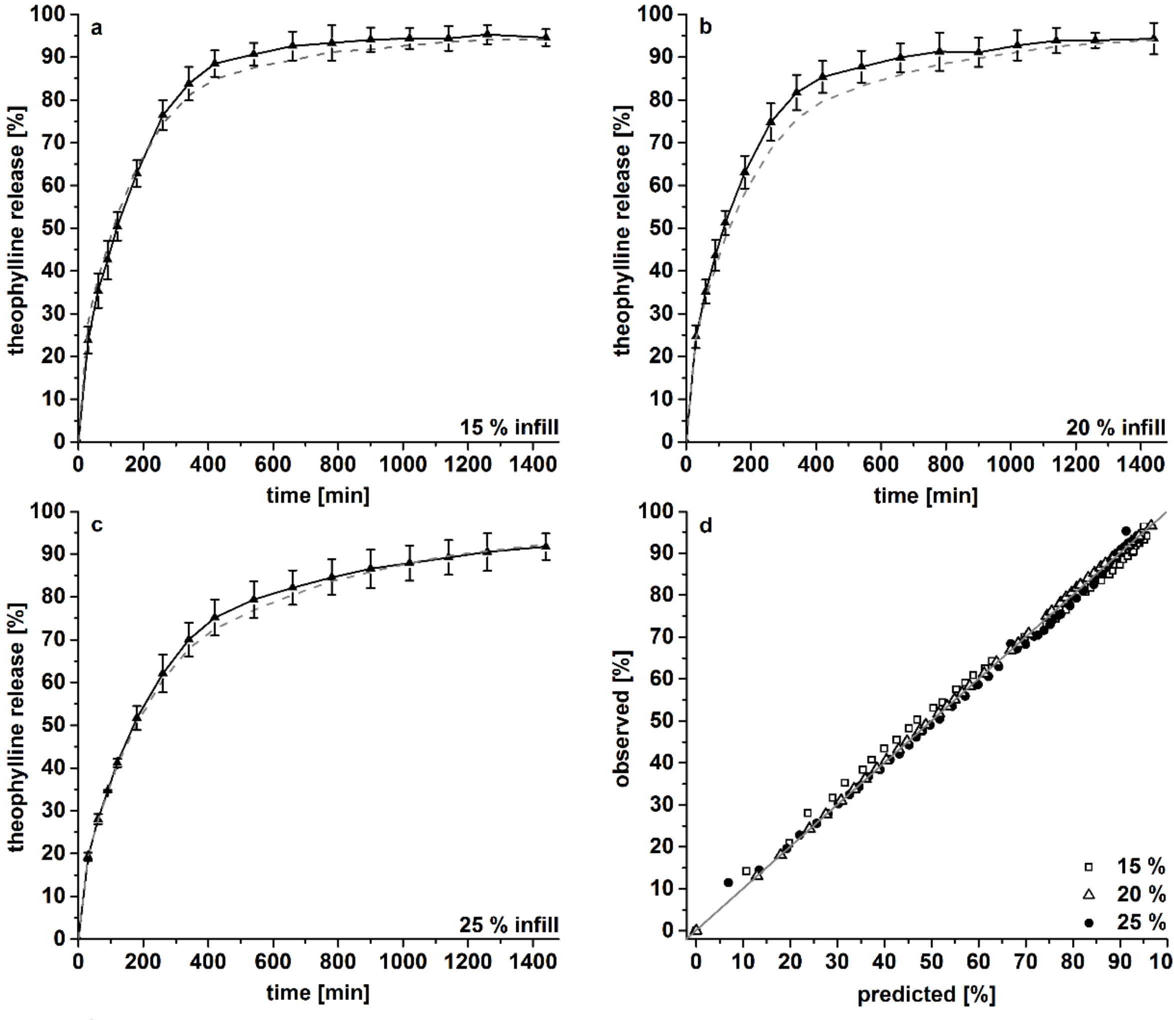

Figure 59. Observed dissolution curves (n = 3, mean ± sd; 37 ± 0.5 °C, 100 rpm, 1000 mL phosphate buffer 0.05 M pH = 6) for theophylline release from printed DDS with (a) 15 %, (b) 20 % and (c) 25 % fill density and corresponding predicted curves based on linear interpolation. (d) Observed vs. predicted plot for prediction based on linear interpolation for different fill densities (adapted from [135], by courtesy of Springer Nature).

Table 10. RMSEP values calculated for different methods of prediction for in-vitro dissolution curves (adapted from [135], by courtesy of Springer Nature; Copyright © 2018 Springer Nature).

	Data sets used for prediction	Fill density [%]				
		10	**15**	**20**	**25**	**30**
RMSEP values obtained via Higuchi model [%]	10 %	-	2.63	3.43	11.00	-
RMSEP values obtained via linear inter-/ extrapolation [%]	10 %, 30 %	-	2.18	3.70	1.40	-
	10 %, 15 %	-	-	5.50	7.05	10.57
	25 %, 30 %	4.07	3.25	2.68	-	-

The predictions (Table 10) based on the Higuchi model and on linear inter- and extrapolation indicated that linear interpolation was more suitable for dissolution prediction with a dose variation between 97.5 mg (15 % fill density) and 140.4 mg (25 % fill density). Linear interpolation was able to involve gradual changes in dissolution behaviour, most likely caused by insufficient perfusion of denser dosage forms. Nevertheless, using the Higuchi model for prediction might be a promising approach, which could be improved. The dose of a solid dosage form might be adjusted by varying the size and keeping the infill constant at 10 %. In this case, Higuchi's model might be able to predict drug release despite of dose changes based on only one data set. Issues regarding the shell might be cancelled out by using a water-soluble drug-free filament for printing it: Stability during the printing process and the removal from the build plate would be given and the dissolution might not be disturbed, since the shell immediately dissolves after placing the dosage form in the testing vessel.

Although regulatory aspects still have to be solved, this dosage form might be a promising approach to produce sustained-release individual dosage forms. It might not only be used similar to an orally taken tablet, but also as drug-eluting insertion in a 3D-printed implant. Hence, the implant itself could be drug-free, but might contain a drug-loaded insertion, which could be able to release the API in a predictable sustained-release manner. Of course, for the prediction of in-vivo drug release, in particular for implants, more effort regarding the development of a bio-relevant dissolution method would be necessary.

3.4.4. Dosage Forms Consisting of Two Filaments

3.4.4.1. Production of Dosage Forms

Dosage forms consisting of both formulations, F5 and F10, were produced to investigate whether a biphasic dissolution profile might be achieved and predicted. For theophylline, this application might not be necessary, but it might be beneficial for numerous APIs. Not only biphasic dissolution profiles of the same API, but also fixed dose combinations of APIs in matrices enabling different release kinetics might be achieved, e.g. as applied for non-steroidal anti-inflammatory drugs, APIs in treatment of hypertension, type II diabetes, or HIV [142, 143]. Certainly, these effects might also be achieved by bilayer tablets, but FDM^{TM} promises to enable a more tailored on-demand medication.

In comparison to previous experiments both print heads type II, the left and the right one, were applied. Preliminary studies had shown that F5 and F10 filaments were printable with print heads type II as well. The thresholds for printability were not investigated for print heads type II. Filaments were printed into dosage forms of the same shape as in section 3.4.3 (Figure 46, left) (n > 3) using both print heads type II. Dosage forms contained different ratios of the two filaments, 5:1, 2:1 and 1:1 referring to the amount of layers, or were entirely printed of one filament used as basis for the release prediction. The CAD-models for the bilayer dosage forms are illustrated in Figure 60. Print heads worked consecutively, when objects with two different filaments were printed. While one was printing, the other one stayed in its waiting position. During this time, oozing from the nozzle was observed, which means that polymer dripped off the print head as it was still heated while waiting for the next application [144]. However, when restarting the print, insufficient material was behind the die and printing was not conducted adequately until the hot end was completely refilled. The typical mean to solve this problem is retraction: the filament is retracted or conveyed backwards a few millimetres so that it is not directly in front of the die [144]. Before restarting, the filament is conveyed to the die again. Nevertheless, in this case, application of different extents of retraction did not solve the oozing problem in a satisfying way, which might be due to inaccuracies in the retraction process.

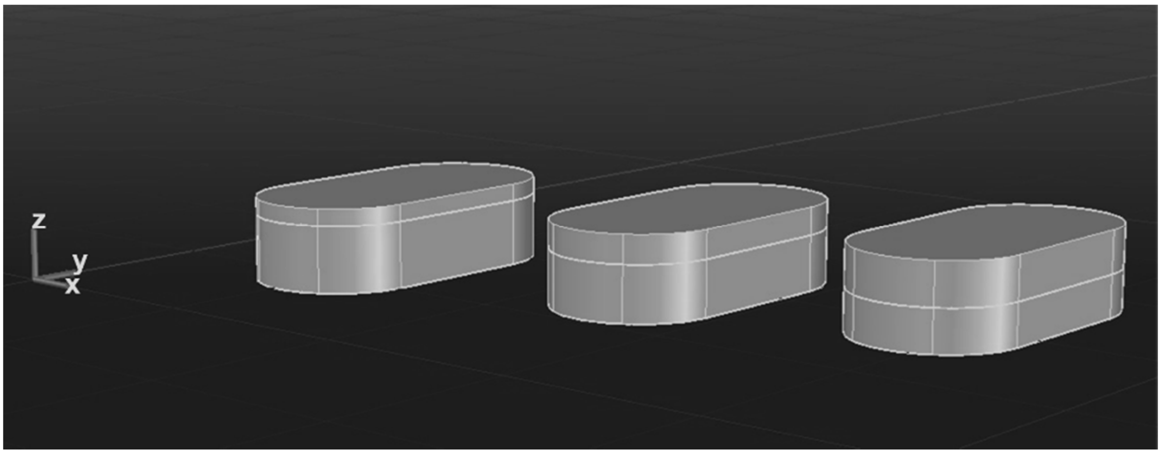

Figure 60. CAD model of bilayer dosage forms with different ratios of 5:1, 2:1 and 1:1. The bottom layer was always printed with F5, the top layer with F10.

Therefore, a special printing regime was applied. In one print job dosage forms of every kind were printed. Figure 61 shows a schematic drawing of the first printed layer. Numbers indicate the printing order, which was the same for every layer. Framed dosage forms were used for further analysis. Accordingly, the first and second dosage form were used to ensure a completely filled hot end. The third and the fourth printed dosage form were chosen for further analysis as their quality was considered sufficient without negative effects due to oozing. This printing regime increased quality of the dosage form used for analysis. However, the required printing time for one dosage form increased as well considering that printing the discarded dosage forms also took its time. Printing time of a 20 % fill density dosage form printed of one filament was 185 s, whereas printing time of a 20 % fill density dosage form printed of two filaments took 348 s in the applied printing regime.

Different ratios of F5 and F10 filaments, containing either 7 % SA or 7 % PEG4000, were used for printing and are indicated in Figure 60 and Figure 61, right. They were printed in style of bilayer tablets starting with F5 filament in the first layer, except for the pure F10 dosage form. All dosage forms consisted of 12 printed layers, so that ratios of 5:1, 2:1 and 1:1 regarding the number of layers could be realized. Dosage forms or pure F5/F10 were also printed, since prediction of biphasic dissolution profiles should be based on those from pure dosage forms. Fill density was in all cases 20 %, since this fill density was the best compromise between API load and good perfusion of the dosage form during dissolution testing.

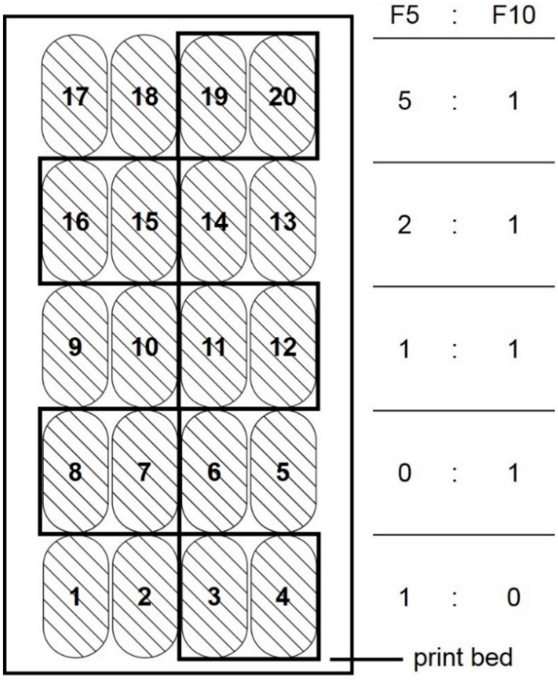

Figure 61. Left: schematic drawing of the first layer of the printing regime for dosage forms containing two filaments. Numbers indicate the printing order. Framed dosage forms were considered for further analysis. Right: ratios of the different dosage forms.

3.4.4.2. Physical Properties

After printing, the mass of the bilayer printed dosage forms was determined. Figure 62 depicts the mass of the dosage forms depending on the ratio of F5 filament. Dosage forms, which were entirely printed using F10 were the lightest ones and with increasing amount of F5 layers the mass increased as well. In previous studies (section 3.4.3), F10 dosage forms were heavier than those printed using F5 filament. Discrepancy was explained by change of the conveying system (print head type I vs. print head type II). Therefore, production conditions and probably properties of the printed DDS were hardly comparable to results from the previous studies. Consequently, data obtained in section 3.4.3.3 was not used for prediction, although the printing commands were similar. Dosage forms containing solely F5 or F10 were printed again using print heads type II for the present study. Since mass variation of the printed DDS were <3 % (Figure 62), they were considered acceptable. A linear correlation with a coefficient of determination of 0.9990 between the values was determined. Further, mass of the bilayer dosage forms was calculated taking the mass of the pure dosage forms and their ratio into account. Resulting values are depicted in Figure 62, too. They corresponded well to the empirically found values and were used for prediction of dissolution curves (section 3.4.4.4).

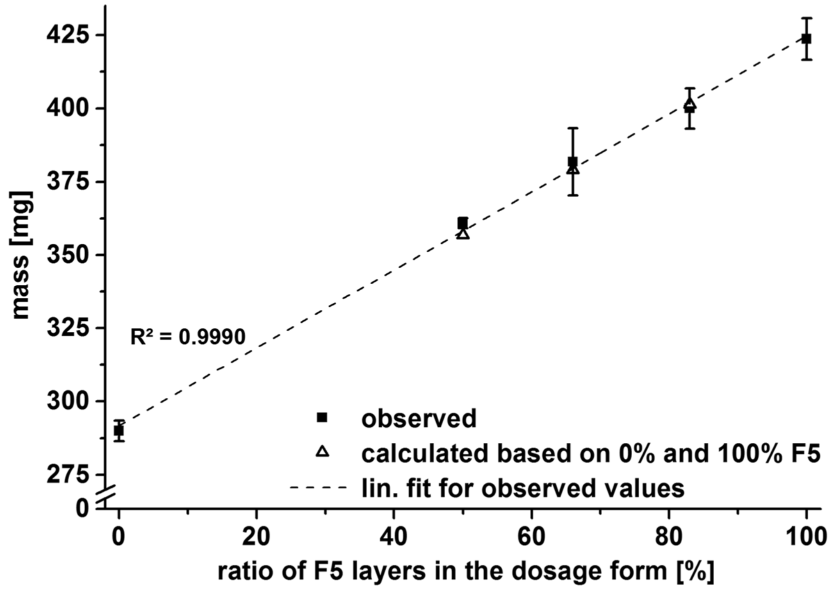

Figure 62. Mass of bilayer dosage forms containing F5 and F10 layers (n = 3; mean ± sd).

3.4.4.3. Dissolution Properties

Bilayer printed dosage forms were subjected to dissolution analysis presented in section 3.4.3.3. Dosage forms had to be fixed carefully in the clasps of the sinker, since at the junction of the both layers a breakage was probable. Obtained in-vitro dissolution data is shown in Figure 63. In this case, the number of data points in dissolution curves was reduced from 50 to 17 similar as in the previous section 3.4.3. All graphs include dissolution curves obtained by pure F5 or F10 printed dosage forms and clearly illustrate that bilayer dosage forms exhibited hybrid dissolution curves between the two extreme cases. With higher ratios of F5 filament in the dosage form, the dissolution profile of the bilayer dosage form aligned to the obtained profile for the pure F5 printed dosage forms. The higher the amount of F10 filament, the more drug was released immediately ($t_{50\%, 1:1}$ = 50 min, $t_{50\%, 2:1}$ = 70 min, $t_{50\%, 5:1}$ = 110 min).

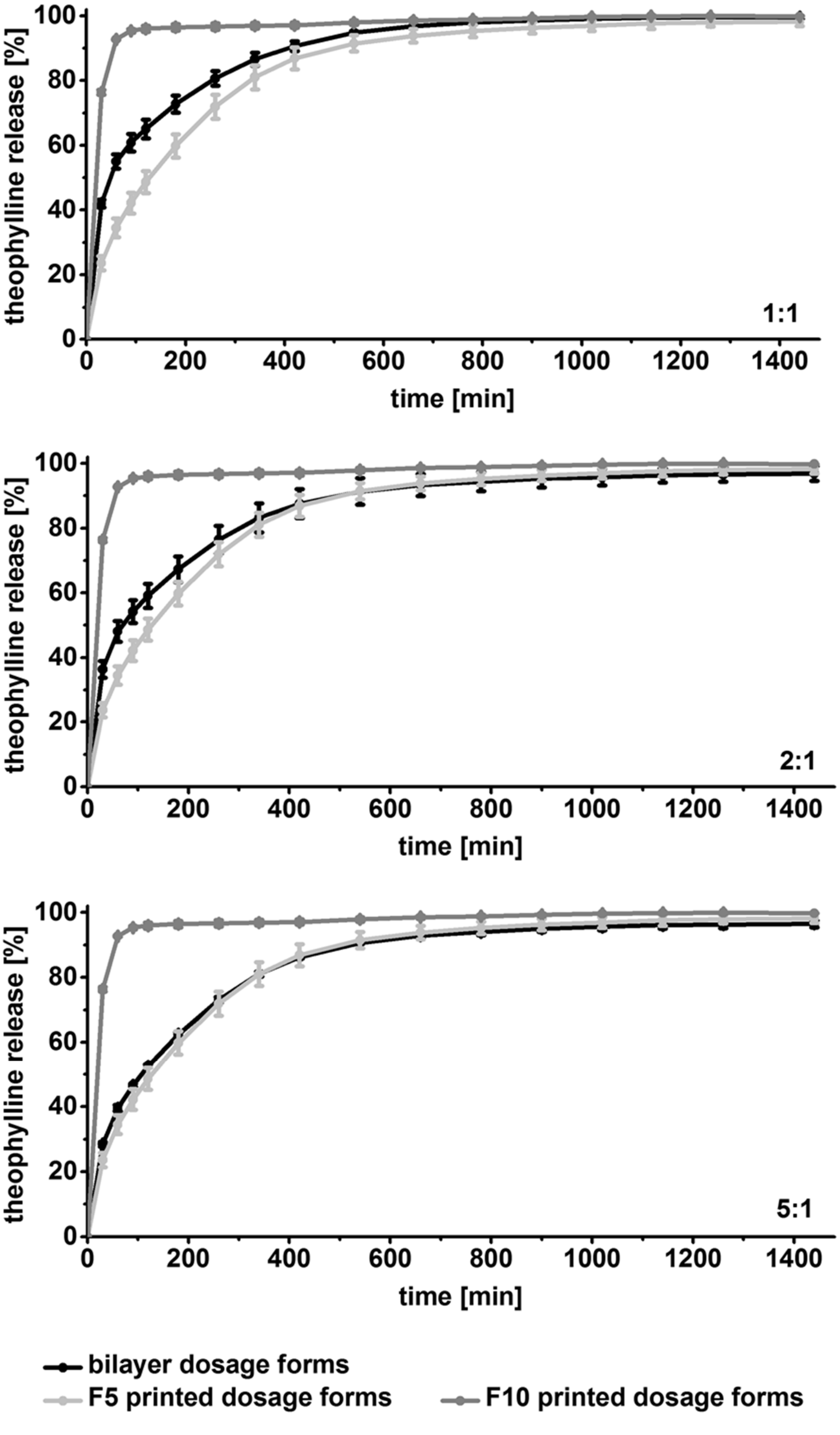

Figure 63. In-vitro drug release from printed dosage forms:
release from F5 and F10 purely printed dosage forms are depicted in every figure for reasons of comparison. Indices 1:1, 2:1 and 5:1 correspond to the number of F5:F10 printed layers in one DDS (n = 3; mean ± sd).

3.4.4.4. Prediction of Biphasic Dissolution Profiles

Similar to the calculation of the mass of the dosage forms (3.4.4.2), profiles of the bilayer printed dosage forms were predicted based on pure printed F5 and F10 dosage forms using Equation 9:

Equation 9. Additive dissolution prediction of bilayer printed tablets.

$$M_{t,rel,bil} = \frac{M_{t,bil}}{M_{100\%,bil}} = \frac{M_{t,F5} \cdot x + M_{t,F10} \cdot y}{M_{100\%,F5} \cdot x + M_{100\%,F10} \cdot y} \cdot 100$$

Relative amount of released API from the bilayer printed tablet at time point t ($M_{t,rel,bil}$) was calculated as quotient of the amount of released API at time point t ($M_{t,bil}$) and the total amount of API in the dosage form ($M_{100\%,bil}$). $M_{t,bil}$ was calculated as sum of the released amount of API from the F5 or F10 printed layers ($M_{t,F5}$ and $M_{t,F10}$) multiplied with the particular ratio (x, y) in the dosage form, e.g. x = y = 0.5 for 1:1 dosage forms. $M_{100\%,bilayer}$ was calculated likewise.

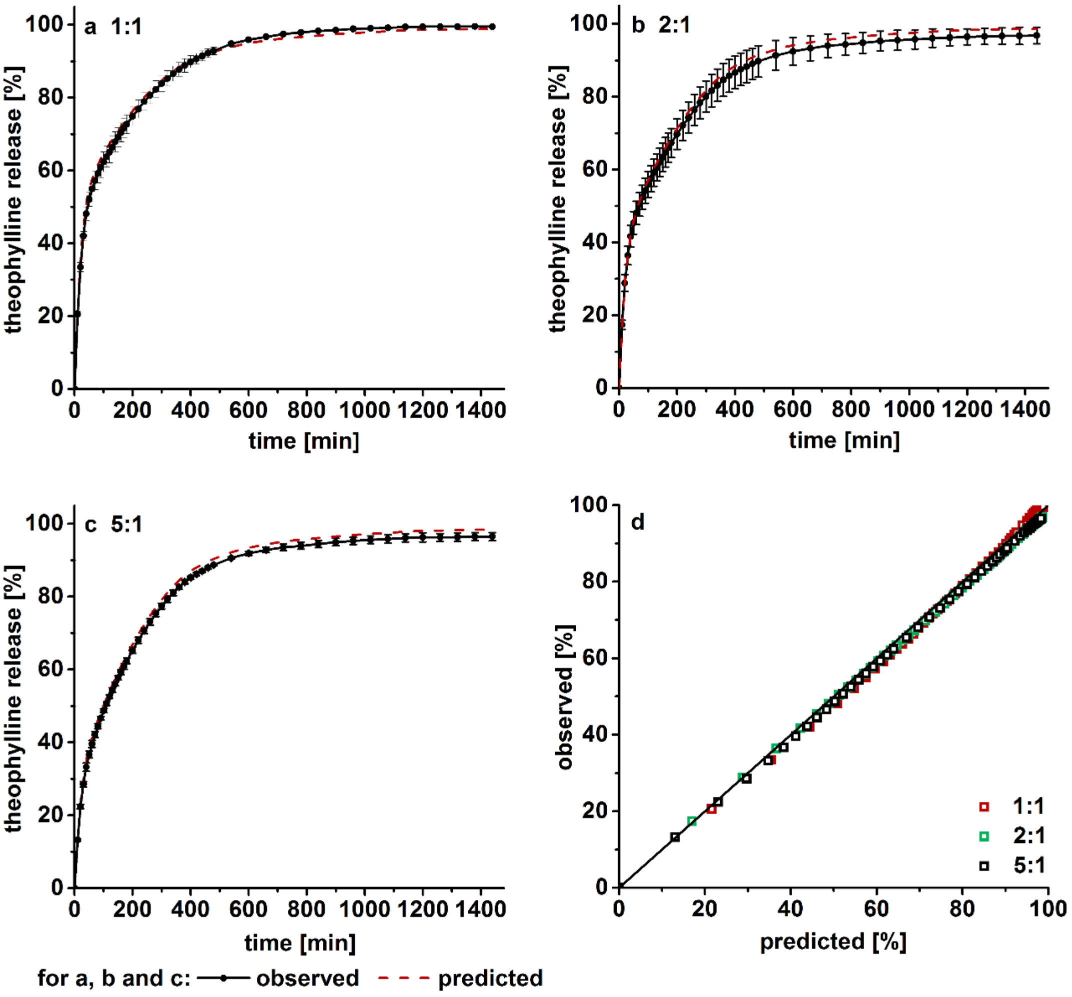

Figure 64. Drug release from bilayer printed dosage forms: observed (n = 3; mean ± sd) and predicted dissolution curves for bilayer printed dosage forms of F5 and F10 in ratios of 1:1 (a), 2:1 (b) and 5:1 (c). Observed vs. predicted plot for release prediction of bilayer printed dosage forms (d).

Figure 64 a-c shows the dissolution curves and the corresponding predicted curves. In all cases, the predicted curves are very close to the experimental ones. Quality of the model was also underlined by observed vs. predicted plot (Figure 64 d) and the RMSEP values. These were 1.49 (1:1), 1.51 (2:1) and 1.64 % (5:1). This indicated that simple proportionate addition of dissolution profiles of purely printed dosage forms was found as adequate mean for prediction of biphasic dissolution profiles. Although it was not explicitly tested, it is probable that dissolution prediction of dosage forms with more than 12 layers or less, and thereby a varying API dose, might be feasible as well.

3.4.5. Summary

Dosage forms with network structures, which are directly exposed to the dissolution medium, were presented as novel solid dosage form produced via FDM^{TM}. This unique structure can hardly be produced via other well-established processes used in pharmaceutical technology, e.g. tableting or injection moulding, and might be useful as oral solid dosage form or as drug-eluting insertion in an implant.

The first part of the printing studies revealed that variations of the fill density was an adequate mean to vary the dose of the printed dosage form. Since a linear correlation between fill density and mass/dose was found, a predetermined target dose might be printable. Additionally, the SSA of the network hardly varied. However, different fill densities led to differences in pore size and, thereby, at higher fill densities to a non-uniform perfusion of the dosage form by the dissolution medium. This changed the dissolution kinetics, despite of a nearly constant SSA. Nevertheless, dissolution profiles were predictable using linear interpolation between 10 and 30 % fill density. Due to change in release kinetics, the Higuchi model was not applicable. Still, this might be used varying the dose by using different sizes of the printed dosage form and keeping the fill density constant at 10 %. This might be evaluated in future studies.

Second part of the printing studies dealt with the printing of bilayer dosage forms. The two layers consisted of the same API and polymer but contained a different type of plasticizer. F5 formulation contained lipophilic SA and F10 hydrophilic PEG4000 in the same ratio (7 %). Due to differences in hydrophobicity, F5 and F10 released the API at a different rate. This led to biphasic dissolution profiles for the bilayer printed dosage forms. Considering purely printed dosage forms of F5 or F10, an accurate and reliable prediction (RMSEP < 1.64 %) was feasible.

Printing studies involved in this work showed the applicability of FDM^{TM} for the production of solid dosage forms, which cannot be produced with established techniques used in pharmaceutical technology. Developed networks might enable production of tailored sustained-release dosage forms with predictable dissolution profiles. However, especially for the production of individual oral solid dosage forms with sustained drug release, explicit advantages of 3D-printing still have to be shown compared to multi particulates. For 3D-printed dosage forms, regulatory issues, a comparatively long production time and thermal stress during production are still severe drawbacks.

4. Summary

The focus of the present work has been the development of 3D-printable filaments via continuous HME for 3D-printing of innovative dosage forms exhibiting sustained theophylline release. This also involved process analytical technologies useful for HME and 3D-printing.

Formulation development of printable filaments was performed taking the mechanical resilience and the drug release properties into account. Anhydrous theophylline was chosen as model API as it is thermally stable, shows low tendency for incompatibilities and required high drug loadings of the filament. Amongst sustained-release polymers, aPMMA was selected as matrix. A plasticizer was required to improve extrudability by a decreased melt viscosity and probability of melt fracture during the process and, thereby, to improve the shape uniformity of the filament. Further, plasticizers were needed to achieve suitable mechanical properties for processing the filament inside the print head. To avoid the evaporation of plasticizer either during the process or over storage, which might have caused deterioration of mechanical properties and change of the relative API content in the filament, only solid plasticizers were considered for formulation development. With regard to the release properties, SA and PEG4000 were chosen as solid plasticizers with different hydrophilicities assuming to achieve differences in drug release.

To evaluate the printability of the filament prior to using them in an FDM^{TM} 3D-printer and to estimate the influence of different excipient ratios in the formulation, a suitable mechanical testing regime for the filaments was developed. The regime involved a tensile test in longitudinal direction for the determination of the YM and a 3PB test in axial direction for the evaluation of the distance at break. A combination of both tests allowed the involvement of different kinds of mechanical stress occurring inside the print head during the conveyance of the filament. In order to ensure printability, thresholds of 300 N/mm² for the YM and 1.125 mm for the distance at break were empirically found. Testing different formulations containing aPMMA, anhydrous theophylline and either SA or PEG4000 revealed systematic chances of mechanical properties. Increasing the API content (10, 30, 50 %) increased the YM and decreased the distance at break. Increasing the plasticizer (3.5 to 21 %) decreased the YM and increased the distance at break. Two formulations containing aPMMA, 30 % anhydrous theophylline and either 7 % SA or 7 % PEG4000 resulted optimal regarding their mechanical resilience and high drug load. Therefore, these were used for subsequent printing of dosage forms. Moreover, printable filaments containing bPMMA or PVA as polymers were successfully developed.

Further, the HME process of printable filaments had to be evaluated regarding its influence on critical quality attributes of the filaments. A decrease in moving speed of the conveyor belt and an increase of the PFR resulted to be the most important parameters to increase the diameter and, thereby, the mechanical resilience of a filament. The extrusion process was shown to be suitable for the production of a filament with a homogeneous API distribution. However, the printability of filaments was not given for more than one week due to ageing phenomena. The period for printability could be enlarged to two weeks by curing the freshly extruded filaments for 24 h in an oven (60 °C).

Since HME of drug-loaded filaments and subsequent processing of the filaments in an FDM^{TM} printer involves heating twice the API, assessment of residence times in both processes was indispensable. During HME the MRT was 642 s, whereas the residence time in the print head was, depending on the print settings, 13 to 69 s. Applied temperatures in the print head were higher than those applied in HME. Nevertheless, it was concluded that the thermal stress in 3D-printing might not play a decisive role for the thermal degradation of APIs in comparison to the previous extrusion process. Contactless temperature measurements using an IR camera further revealed that a decrease of thermal stress in 3D-printing might be achieved by a polymer with a high molar heat capacity. Further, a high printing speed, which decreases the residence time in the heated print head and on the heated build plate, can be recommended. The maximum temperature reached in the filament was independent of the printing speed.

Finally, dosage forms were printed using a filament of aPMMA, 30 % anhydrous theophylline and 7 % of either SA or PEG4000. Dosage forms containing SA exhibited a sustained release whereas, dosage forms with PEG4000 showed an immediate release. Due to their sophisticated network design, dosage forms were intended to have a constant SSA, if the API dose is varied. Contrary to the expectations a constant SSA did not lead to a dissolution of the same relative amount of API due to impeded perfusion of the DDS by the dissolution medium at higher fill densities. For the prediction of release behaviour from dosage forms containing SA, the method of linear interpolation with RMSEP values between 1.4 and 3.7 % was developed and resulted in the most suitable technique. Application of the Higuchi model and prediction based on the particular surface was not feasible due to impediment of perfusion in dosage forms with a higher dose. Bilayer dosage forms containing both formulations were successfully printed as well. Their in-vitro drug release was predicted based on the dosage forms containing one formulation with an RMSEP between 1.49 and 1.64 %.

It can be stated that a successful formulation and process development was performed to produce continuously 3D-printable filaments, which were used to print solid dosage forms with innovative geometries and properties via FDM^{TM}. The present work, thereby, provides important knowledge for the establishment of 3D-printing in the production of highly individualized DDS, from which in particular geriatric and paediatric therapy might derive their benefits.

5. Experimental Part

5.4. Materials

Table 11. Substances used for HME of filaments.

substance	abbreviation	trade name	batch	source of supply
anhydrous theophylline	-	-	G120836520	BASF, Ludwigshafen, Germany
basic butylated methacrylate copolymer	bPMMA	Eudragit® E	G150731543	Evonik, Darmstadt, Germany
ammonio methycrylate copolymer type A	aPMMA	Eudragit® RL	G130736099	Evonik, Darmstadt, Germany
hydroxypropyl cellulose MW = 850,000 g/mol	HPC	Klucel™ MF	40280	Ashland, Schaffhausen, Switzerland
polyvinyl alcohol	PVA	Parteck MXP	F1952164640	Merck, Darmstadt, Germany
stearic acid	SA	Baerocid SP-1 A	T100299411	Bärlocher, Lingen, Germany
macrogol MW = 300 g/mol	PEG300	Polyglycol 300	DEG4044171	Clariant, Diemen, Germany
macrogol MW = 4000 g/mol	PEG4000	Pluriol® E 4000 Powder	80318068E0	BASF, Ludwigshafen, Germany
colloidal anhydrous silica	-	Aerosil® 200 VV Pharma	SO08/10580100	Evonik Degussa, Essen, Germany
iron(III)oxide	-	Eisen(III)-oxid rot	18197109	Caesar & Loretz, Hilden, Germany

5.5. Methods

5.5.1. Pretext

Most of the methods have been published similarly in the research papers “Formulation Development and Process Analysis of Drug-loaded Filaments manufactured via Hot-Melt Extrusion for 3D-Printing of Medicines” (DOI: 10.1080/10837450.2018.1433208) and “3D Printed Network Structures as controlled Release Drug Delivery Systems: Dose Adjustment, API Release Analysis and Prediction” (DOI: 10.1208/s12249-018-1017-0).

5.5.2. Manufacturing Methods

5.5.2.1. Powder Mixtures

Colloidal anhydrous silica and anhydrous theophylline were passed through a sieve (355 µm) to ensure absence of powder agglomerates. All components of the powder mixture, usually API, colloidal anhydrous silica, polymer and plasticizer, were blended for 20 min (Turbula® mixer T 2 F, Willy A. Bachofen Maschinenfabrik, Switzerland). The ratios of the components are displayed in Table 1. The batch sizes varied dependent on the intended use and are shown in Table 12.

Table 12. Batch sizes used in the different sections, the purposes and corresponding formulations.

section	purpose	formulation	batch size [g]
3.1.3	formulation development	F1 to F13; F16	300
		F14	600
		F15	400
3.2.3.1	process analysis (DoE)	F5	two batches à 700
3.2.3.3	determination of the residence time distribution	F5	two batches à 400
3.2.4.1	analysis of homogeneous drug distribution	F5; F10	500
3.2.4.2	thermal stability testing	F5; F8	20
3.2.4.2	off-line dosing experiment for segregation analysis	F5	300
3.4	production of printable filaments	F5; F10	300

5.5.2.2. Hot-Melt Extrusion (HME)

The powder mixture was gravimetrically fed (KT 20, K-Tron Soder, Switzerland) into the extruder barrel. Dosing factor calibration was performed prior to every trial. HME was conducted using a 16 mm 40 D co-rotating twin-screw extruder (Pharmalab HME 16, Thermo Fisher Scientific, Germany) equipped with a 1.75 mm die. Behind the outlet the extruded filament was cooled and transported using a conveyor belt (model 846102.001, Brabender, Germany). PFR and RPM speed were always 5 g/min and 20 rpm, respectively. However, for the DoE these parameters were varied systematically (section 3.2.3.1). The applied screw configuration was the same for all experiments and is shown in Figure 12. For F14 and F15 feeding of liquid plasticizer PEG300 was performed with a peristaltic pump (Minipuls 2, Gilson, USA). Effective mass fed per minute was determined directly after extrusion against an analytical balance (CP 224s, Sartorius, Germany).

The speed of the conveyor belt was determined by measuring the time for one turn at four different levels (29, 80, 120, 200, 300). Figure 65 displays the corresponding calibration function.

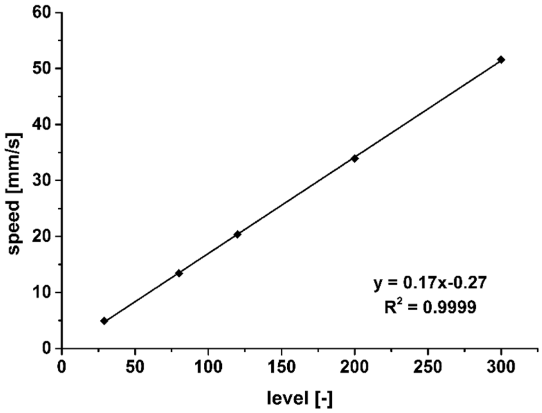

Figure 65. Conveyor belt speed (n = 3; mean ± sd)

Keeping constant the screw configuration, the PFR, the RPM and the die diameter, temperatures and CBS were adapted individually for the formulations to achieve extrudability and acceptable extrudate diameters. Barrel temperatures and CBS are displayed in Table 2.

Process parameters were recorded and monitored via a LabView 2015 application at a frequency of 1 Hz. Sampling time always started after reaching a process equilibrium, which was assumed, when the pressure at the die and the torque appeared constant.

5.5.2.3. 3D-Printing via Fused Deposition Modelling (FDM^{TM})

The CAD model (Figure 46) for 3D-printing was designed in AutoCAD$^{®}$ 2016 (Autodesk, USA) and exported as .stl-file. The G-code file, which contained corresponding commands for the 3D-printer, was generated by processing the .stl-file with the open source software Slic3r (version 1.2.9). Dosage forms were printed with a Prodim XXL pro FDM^{TM} printer (XXL pro, Prodim International, Netherlands). This printer was equipped with two print heads. Most of the printing experiments (sections 3.1.4.2, 3.2.3.1, 3.2.5, 3.4.3) were conducted with the commercially provided print heads type I (Figure 17, left). Printing of dosage forms containing two types of filaments (section 3.4.4) were performed with the customized print heads type II (Figure 17, right).

Kapton tape is a self-adhesive film widely used in FDM^{TM} was used to cover the build plate to improve adhesion of the printed object. Print parameters were adapted with regard to the particular aim of the experiment and to the utilized filaments. Since there were many print settings to choose, the most important ones are displayed in Table 13, whereas Table 17 (appendix) contains all settings. Printing speed refers to the speed of the outlet filament. DDS printed in the DoE were printed one by one in separate printing jobs. Network DDS used in section 3.4.3 were printed in a batch of 10 in one print job. Printing regime for networks of two filaments was described in detail in section 3.4.4.

Table 13. Print parameters.

parameter	DoE (section 3.2.3.1)	networks of single filaments (section 3.4.3)	networks of two filaments (section 3.4.4)
print head temperature	180 °C	180 °C for F5 170 °C for F10	180 °C for F5 185 °C for F10
build plate temperature	30 °C	50 °C	40 °C
fill density	80 %	10, 15, 20, 25, 30, 40 %	20 %
fill pattern	rectilinear	rectilinear	rectilinear
fill angle	45°	45°	45°
layer height	0.2 mm	0.4 mm	0.4 mm
first layer height	0.4 mm	0.4 mm	0.4 mm
perimeters	2	1	1
solid layers	2 top 2 bottom	-	-
seam position	random	random	random
speed for the perimeters	15 mm/s	15 mm/s	15 mm/s
speed for the infill	15 mm/s	15 mm/s	15 mm/s
speed for the top solid infill	15 mm/s	-	-
travel speed	80 mm/s	80 mm/s	80 mm/s
first layer speed	20 mm/s	20 mm/s	20 mm/s
print head no.	1, left	1, left	2, left for F5 2, right for F10
nozzle diameter	0.4 mm	0.4 mm	0.4 mm

5.5.3. Design of Experiments (DoE)

Systematic analysis of the effects of HME process parameters on the quality attributes of filaments was performed using a 2^4 full factorial DoE. PFR, CBS, TEMP and RPM as factors were varied on two different levels. Further, three repetitions at the centre point were performed. The corresponding matrix is displayed in Table 14. The diameter of the filament, the E_{mod} determined in a tensile test and the extrudate content were chosen as responses. Experiments were conducted in a randomized run order. The first 9 experiments were conducted on one day, the last 10 on another. For both days 700 g of an F5 powder mixture were prepared. Experimental settings were adapted for each run and sampling time started after reaching a process equilibrium. Data evaluation was done in Modde 9.0 (Umetrics, Sweden) on a 5 % significance level. Multiple-linear regression and removal of insignificant parameters by backward regression were used to obtain models with highest goodness of prediction (Q^2).

Table 14. DoE matrix
(modified from [92] by courtesy of Taylor & Francis; Copyright © 2018 Taylor & Francis Group).

	-1	0	1
PFR [g/min]	5	7.5	10
CBS [mm/s]	46.67	60.61	74.55
TEMP [°C]	140	160	180
RPM [1/min]	20	30	40

5.5.4. Drawing of Chemical Structures

Chemical structures of theophylline, aPMMA, SA and PEG4000 were depicted using ChemDraw® Professional 16.0.0.82 (PerkinElmer Informatics, USA).

5.5.5. Analytical Methods

5.5.5.1. Arithmetic Operations

All arithmetic operations used for data evaluation were performed using Microsoft Excel 2013 (Microsoft Corporation, USA). For FFT, Shapiro-Wilk normality test ($\alpha = 0.05$) and unpaired two sample student's t-test ($\alpha = 0.05$) Origin Pro software (9.0.0G, OriginLab Corporation, USA) was applied.

5.5.5.2. In-Line Diameter Determination of Filaments

After cooling of the extrudate on a conveyor belt, in-line diameter determination of the filament was performed. While the filament passed horizontally, the measurement module (Laser 2025

T, Sikora, Germany) recorded diameter values of the cross section in three different directions with a frequency of 1 Hz. The smallest of the given values was used for data evaluation and calculation of the cross-sectional area.

Correctness of the collected diameter data was ensured by performing a calibration against a micrometre screw measuring six metal rods of different diameters between 1.2 and 6 mm ($n = 5$). The determined calibration function with a slope close to 1 and an intercept close to 0 was considered adequate ($y = 0.9998x + 0.0083$). Sufficient linearity was underlined by $R^2 = 0.999999$.

5.5.5.3. Young's Modulus (YM)

YM was determined as a measure for longitudinal stiffness in a tensile test using a texture analyser TA.XTplus (Stable Micro Systems, UK). The experimental setup is displayed in Figure 66 on the left. The filament was fixed between two grips with a torque of 1 N·m to ensure both identical test conditions and properly fixed samples without breakage. Clamps had a small furrow on the inside so that filaments did not slip to the side during fixation. In all cases, sample length was 20 mm and moving speed of the probe was 0.01 mm/s. While testing, force-elongation curves were recorded by Exponent software 6.1.5.0 (Stable Micro Systems, UK). Force values were converted into corresponding tensions by dividing them by the cross-sectional area of the particular filament. For all samples, a linear elastic behaviour was observed below 0.25 % elongation. Therefore, YM could be calculated as the slope in a tension-elongation curve between 0.05 and 0.25 % elongation according to DIN EN ISO 527-1 [101].

All measurements, except for those presented in section 3.2.5, were performed one day after extrusion to avoid influences due to filament ageing.

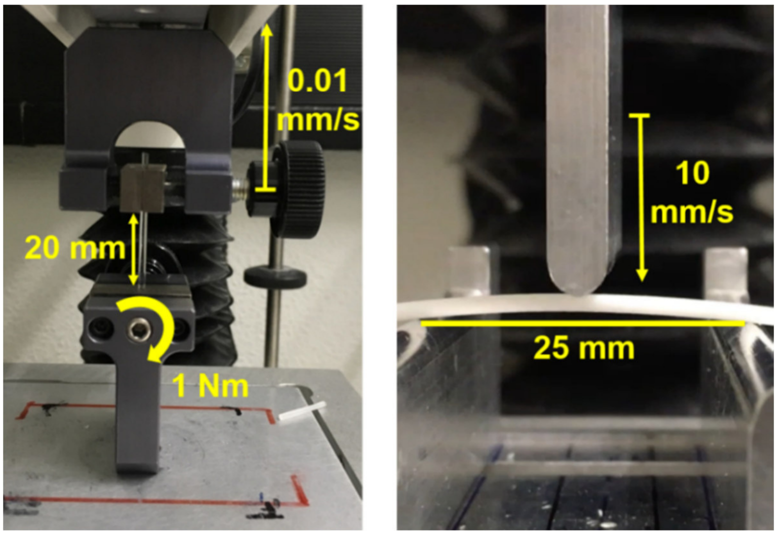

Figure 66. Experimental setup for the tension (left) and the 3PB test (right).

5.5.5.4. Distance at Break

The distance at break was determined as a measure for transversal, punctual mechanical resilience in a 3PB test using a texture analyser (TA.XTplus, Stable Micro Systems, UK). The experimental setup is displayed in Figure 66 on the right. The test settings were chosen according to Zhang et al. [64]. Test length was 25 mm and moving speed of the probe was 10 mm/s. The distance at break was defined as the distance the probe covered from the first contact with the filament to material failure. In case material failure did not occur, e.g. due to high flexibility of the filament, distance at break was considered unlimited under the defined testing conditions.

As in case of the YM, the distance at break was measured one day after extrusion to avoid influences due to filament ageing, except for those experiments presented in section 3.2.5.

5.5.5.5. Differential Scanning Calorimetry[1] (DSC)

Samples of ~ 5 mg were subjected to DSC (DSC 1, Mettler-Toledo, Germany) analysis in a sealed aluminium pan with a punctured lid. For the raw materials, always two heating cycles were used, whereas extrudates were heated only once. Detailed information about heating and cooling profiles are shown in Table 15. Data evaluation, including determination of melting points and glass transition temperatures was performed using STAR^e software (Version 9.20, Mettler-Toledo, Germany).

Table 15. Heating and cooling profiles for DSC measurements.

	sample	heating and cooling profile	section
powders	anhydrous theophylline SA aPMMA	- 20 °C to 170 °C, 10 °C/min 170 °C to - 20 °C, 20 °C/min - 20 °C to 300 °C, 10 °C/min	3.1.4.3
	PEG4000	- 50 °C to 300 °C, 10 °C/min 300 °C to - 50 °C, 10 °C/min - 50 °C to 300 °C, 10 °C/min	
extrudates	F2	- 50 °C to 300 °C, 10 °C/min	3.1.4.3
	F10		
	F5 beginning	- 20 °C to 300 °C, 10 °C/min	
	F5 ending		
	F5 after two weeks	- 20 °C to 300 °C, 10 °C/min	3.2.5
	F5 cured after two weeks		

5.5.5.6. Hot-Stage Microscopy

Hot-stage microscopy images were taken using a polarization filter to enable detection of crystalline structures. Substances were put onto a cover glass positioned onto a hot stage

---

[1] Measurements as well as parts of the data evaluation were performed by Karin Matthée at the Institute of Pharmaceutics and Biopharmaceutics at the Heinrich Heine University in Düsseldorf.

connected to a temperature control module (THMS 600 and TMS 94, Linkam Scientific Instruments, UK). Automatic heating was performed with 10 °C/min until 50 °C, 2 °C/min between 50 and 100 °C and 5 °C/min between 100 °C and 190 °C. Every 3 s an automatically triggered picture (DFC450, Leica Microsystems, Germany) was taken, while inspecting the sample with a light microscope (DM LB, Leica Microsystems, Germany). Based on the particular heating rates, the temperature for every picture was calculated. Only selected pictures were displayed (Figure 24).

5.5.5.7. E_{mod} Value

The experimental procedure was the same as for YM (section 5.5.5.3). However, data evaluation was performed differently. The E_{mod} value was calculated as slope in a force-elongation-curve between 0.05 and 0.25 % elongation.

5.5.5.8. Theophylline Assay

The content of theophylline was determined for extrudates, printed dosage forms and intact matrices after dissolution testing. In all cases, samples were dissolved in 70 % (w/w) ethanol using sonication. A clear and transparent solution resulted. Sample size varied and was described in the particular section of this work. After entirely dissolving the matrices, solutions were diluted so that an absorption covered by the calibration function was achieved. Quantitative spectroscopic measurements were performed with either Lambda 2 UV/Vis-spectrometer, Lambda 25 UV/Vis-spectrometer (both Perkin-Elmer, USA) or UV-1800 (Shimadzu, Germany) at 271 nm. Evaporated ethanol was refilled right before the analyses. A solution of drug-free extruded matrix containing aPMMA did not show absorption at 271 nm in 70 % (w/w) ethanol. Quantitative evaluation was performed using the calibration functions displayed in Figure 67.

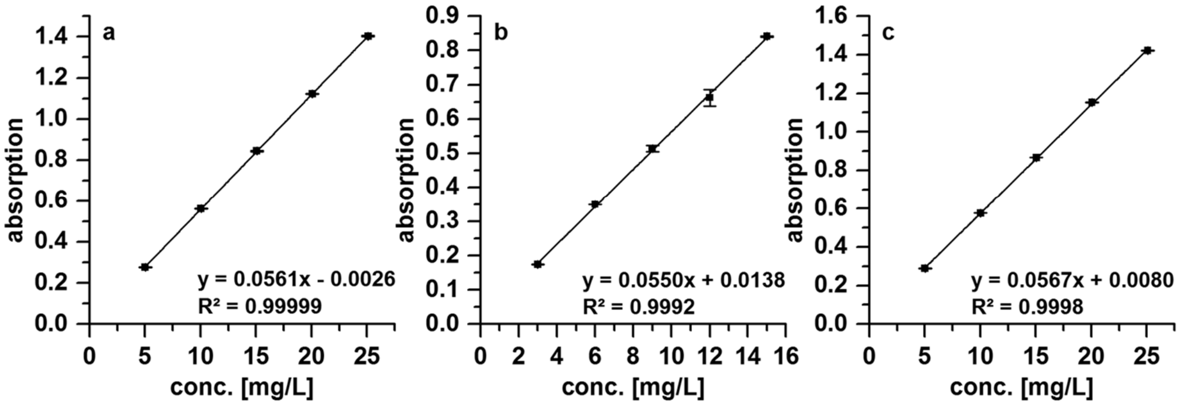

Figure 67. UV-absorption by anhydrous theophylline in 70 % (w/w) ethanol; (a) Lambda 2; (b) Lambda 25; (c) UV-1800; λ = 271 nm; n = 3; mean ± sd.

5.5.5.9. Inspection of Filament Surface Structures

Images of filaments were taken by a Perfection V37 Scanner (Epson, Germany) at a resolution of 2400 dpi.

5.5.5.10. Residence Time Distribution in Twin-Screw Hot-Melt Extrusion

Determination of residence time distribution in twin-screw HME was performed (n = 2) using the ExtruVis 3 system and corresponding ExtruVis 3 software (ExtruVis, Germany). The ExtruVis 3 system consists of a camera (USB-CAM-052H, Phytec,Germany) and an LED ring light to ensure an equally bright measuring field. Addition of red iron oxide as pulse via the feeding funnel is further described in section 3.2.3.3. The camera was able to detected RGB-distribution (red, green, blue) for a selected image section. Since a red dye was applied, changes in the red color ratio were used as response variable. Red color ratio was defined as red signal divided by the sum of red, green and blue signal. The chosen experimental setup enabled data evaluation based on a 93 and 93.4 frame rate. Measured intensities were automatically fit to an exit age distribution function (E(t)) modified according to Danckwerts et al. [111, 127]:

Equation 10. Modified exit age distribution function for residence time analysis using ExtruVis system.

$$E(t) = \frac{C(t)}{\int_{t_1}^{t_{out}} C(t)dt}$$

C(t) represents the tracer concentration between time points t and t+dt. As MRT the time point was defined, at which a perpendicular line to the x-axis divided the integral of E(t), or rather the area under the curve of E(t), into two areas of equal sizes [71]. The MRT was calculated and provided by the software based on following equation [145]:

Equation 11. Calculation of the MRT using ExtruVis system.

$$MRT = \frac{\int_{t1}^{t_{out}} tCdt}{\int_{t_1}^{t_{out}} Cdt}$$

Equations include the concentration of tracer between t and t+dt as time points (C(t)), the time point at which the tracer was detected for the first (t_1) and the last time (t_{out}). Using the fit function, the software provided time points for the maximum tracer concentration (t_{max}) as well.

5.5.5.11. Thermal Stability Testing

Powder mixtures (20 g) containing SA 7 %, aPMMA and 30 or 50 % theophylline (F5, F8) were blended. Half of the mixture was put into an oven (Klevitront, Thermo Scientific Heraeus, Germany) for 15 min at 180 °C. After cooling back to room temperature, the theophylline content was determined in the initial and the heat-treated mixture (n = 3). Samples of 100 mg were diluted in ethanol 70 % (w/w) and analysed according to section 5.5.5.8.

5.5.5.12. Particle Size Distribution

The particle size distributions (n = 3) were determined via laser diffraction (Mastersizer 3000, Malvern Instruments, Great Britain) with dry dispersion using Fraunhofer approximation for data evaluation. 3 bar were chosen as dispersion pressure.

5.5.5.13. Off-line Dosing Experiments for Segregation Analysis

For segregation analysis, off-line dosing experiments using KT 20-powder feeder (K-Tron Soder, Switzerland) were performed. An F5 powder mixture was produced (section 5.5.2.1) and filled into the feeder. 5 g/min were dosed and at time points 0, 10, 20, 30, 40 and 45 min samples (n = 3) were drawn. Sampling time was 5 s in each case, corresponding to ~422 mg. Further, remaining powder from the feeder was mixed again and samples (n = 3) of ~422 mg were taken. Samples were then diluted in ethanol 70 % (w/w) and subjected to quantitative analysis as described in section 5.5.5.8.

5.5.5.14. Curing of Filaments

Curing was only performed with F5 extrudates. Directly after extrusion, filaments were stored for 24 h at 60 °C in an oven (Klevitront, Thermo Scientific Heraeus, Germany). Further operations, e.g. printing and determination of mechanical properties, were performed after cooling samples to room temperature.

5.5.5.15. Calibration of the F-Unit for the Filament Conveyance in the Print Head

A PLA green filament (Prodim International, Netherlands) was marked lengthwise at a distance of 10 cm and put as feedstock into the print head type I. G-code commands starting with ‘G92 E0’ and followed by ‘G1 E100 FX’ with X equal to 20, 40, 60, 80, 100, 150 and 200 were sent manually to the print head (T = 190°C; n = 3) in randomized order. Inlet filament speed was calculated using the conveyed filament length, determined via the applied marks, and the corresponding time. Finally, the inlet filament speed was converted into outlet filament speed using Equation 1.

5.5.5.16. Calibration of F-Unit for the Build Plate Movement

G-code commands starting with ‘G92 E0’ and followed by ‘G1 Y100 FX’ with X equal to 100, 200 and 300 were sent manually to the build plate (n = 3) in randomized order. The build plate speed was calculated using the moved distance and the corresponding time.

5.5.5.17. Residence Time in the Print Head

While generating the G-code file for printing one to ten DDS in one print job using print adjustments from section 3.4.3 and printing speeds of 15, 50 or 90 mm/s, the required printing time was provided by the slicer software (open source software Slic3r, 1.2.9). Plotting the required printing time against the amount of printed DDS resulted in a linear correlation (Figure 39). The obtained y-axis intercept was subtracted from the printing time given by the software and a mean printing time was calculated (n = 55). Required length of extrudate for one DDS was determined using the mass per extrudate length (2.74 mg/mm; mean, n = 10) and the mean mass of a DDS (423.7 mg; mean, n = 3; section 3.4.3). The quotient of the extrudate length required for one DDS and the mean printing time per DDS was considered as plug flow. For the calculation of corresponding residence times the different lengths of the hot ends ($l_{no.1}$ = 42.8 mm and $l_{no.2}$ = 57.86 mm; Figure 17) were divided by the determined plug flow.

5.5.5.18. Emissivity Calibration of API-loaded Filament

The API-loaded filament was positioned lengthwise and as filament cross-section onto a cover glass, which was placed onto a hot stage connected to a temperature control module (THMS 600 and TMS 94, Linkam Scientific Instruments, UK). A small part of the cover glass was painted with matt brown color to obtain an internal reference during the measurement (Figure 41, left). The hot stage was heated from 70 to 200°C in steps of 20 °C. Target temperatures were hold for 5 minutes and the heating rate was 30 °C/min (Figure 41, left). This process was recorded using an Optris PI 640 IR camera in combination with Optris PI Connect software (both Optris, Germany) at 32 Hz and a distance of 7 cm. Sampling time was 187.5 s at every temperature step and started 60 s after reaching the target temperature to ensure entire heating of the samples.

5.5.5.19. Thermography of the Print Head

Thermography of print head type I was performed using an Optris PI 640 IR camera in combination with Optris PI Connect software (both Optris, Germany). The distance between camera and tip was 9 cm achieving a medium field of view (3 x 3 px) of 270 µm. This was considered small enough for temperature determination of the outlet filament (Ø ≈ 400 µm). Surfaces of the tip and the heating element were covered with matt brown colour. IR images were recorded with a 32 Hz frequency and reduced to 2 Hz during data evaluation. Experiments were conducted using commercial PLA filaments (glow in the dark, Prodim International, Netherlands), F2 and F3 filaments. G-code commands were entered manually so that the print head only extruded the filament at a certain speed but stayed in the same position. Commands and temperatures are displayed in Table 16. The maximum temperature of the print head and temperature of the outlet filament were exported over 313 s in a field of 3 x 3 px. The mean temperature, frequency and amplitude were determined via FFT using Origin Pro 9.0.0G (OriginLab Corporation, USA).

Table 16. Commands and temperatures for thermometric measurement of the print head.

filament	temperature	commands
PLA	180 °C	G1 E2000 F200
F2 **F3**	170 °C 180 °C	G1 E1500 F40 G1 E1500 F100 G1 E1500 F150 G1 E2000 F200

5.5.5.20. Thermography of the Build Plate

Thermography of the build plate was performed using Optris PI 640 camera and Optris PI Connect software. The camera was positioned centrally above the build plate at a distance of 13.7 cm. Surface of the build plate was covered with matt brown colour. Recordings were performed at a frequency of 32 Hz. Temperatures over the length of the build plate were recorded while moving horizontally from back to front with the G-Code command G1 Y220 F300 at set temperatures of 30, 50 and 70 °C (each n = 3). Obtained time depending temperature data was exported from the recording and converted to position depending temperature data taking the moving speed of the build plate into account. For the applied command, this was 4.86 mm/s. Position-dependent temperature data was taken for every 0.5 cm.

5.5.5.21. X-ray Microcomputed Tomography

Surface area (n = 1) and edge length of the created mesh (Figure 48, c) were determined using X-ray microcomputed tomography imaging (CT alpha, ProCon X-Ray, Germany). Scanning was performed with 1600 projections at a 12 µm voxel resolution. 80 kV was chosen as acceleration voltage and 80 µA as currency. VG Studio software 3.0.1 (Volume Graphics, Germany) was applied for image reconstruction. Subsequent visualization and calculation of the surface area as well as the edge length was accomplished with Avizo Fire 9.0 software (FEI, USA). Assignment of particular voxels to the particular material was done by setting starting points using the threshold tool for grey values and application of a watershed algorithm afterwards. Inaccuracies regarding automatic assignment via watershed algorithm were corrected manually. Avizo Fire 9.0 calculated the voxels at the interface of the object and air or fixing material for the sample. Thereby, the surface area of the DDS was obtained.

5.5.5.22. Dissolution Testing

Dissolution studies (n = 3) were performed for 24 h with printed DDS according USP 39 monograph *Theophylline Extended-Release Capsules*. Dosage forms were analysed in a qualified USP-II apparatus (DT 726, Erweka, Germany) equipped with a reciprocating pump (PVP 820, Erweka, Germany) and an UV/Vis- spectrometer (UV-1800, Shimadzu, Germany). Data was recorded using Disso.Net 3.0.3.0 software (Erkweka, Germany). DDS were fixed in in-house built sinkers, which inhibited floating of the DDS and ensured central positioning at the vessel bottom. Rotation of the paddle was 100 rpm. 1000 mL of 0.05 M phosphate buffer at pH 6.6 and a temperature of 37 ± 0.5 °C were used as medium. Dissolution studies were operated under sink conditions, taking a maximum concentration of 201 mg/L into account [146]. Samples were measured spectrophotometically every 10 min for the first 3 h, every 20 min for subsequent 5 h and every 60 min for the last 16 h at $\lambda = 271$ nm in a 1 mm flow-through cuvette. Sampling was done in uneven time intervals, since the dissolution software only enabled taking of 50 samples per cycle and dissolution curves should be displayed as good as possible.

Matrices of aPMMA were non-erodible and still intact after 24 h of dissolution testing. Therefore, after every dissolution run, matrices were analysed regarding their remaining drug content according to section 5.5.5.8. For all data evaluations, sum of residual API in the matrix and released API after 24 h was considered as total API content.

Influence of apparatus related issues on the results was minimized by simultaneous dissolution of different batches in one run. Samples of one batch were analysed in different runs and different vessels.

5.5.5.23. Dissolution Kinetics

Dissolution kinetics of differential curves (Equation 4) were analysed. Data was plotted in a double logarithmic depiction of released API [%] against time [min]. Values > 18 % covering the linear range were considered. Based on Equation 6 the diffusional release exponent n was determined as slope in the double logarithmic depiction indicating the present release kinetic.

5.5.5.24. Modelling of Dissolution Curves Based on the Higuchi Model

Constant D_k (section 3.4.3.6) was determined based on differential curves of released API from 10 % fill density dosage forms (Equation 4). Q, as the quotient of the absolute amount of released API and the surface of the dosage form (section 5.5.5.21) [mg/cm²], was plotted against the root of time [$\text{time}^{0.5}$]. D_k represented the slope in this graph. Considering D_k and the particular surface of the dosage forms (section 3.4.3.2) a prediction of drug release was performed based on Equation 8.

5.5.5.25. Modelling of Dissolution Curves Based on Linear Inter- or Extrapolation

Differential curves (Equation 4) for the API release [%] of two fill densities were used to predict the drug release. Interpolation was done based on dissolution data of 10 and 30 % fill density dosage forms, whereas extrapolation was done using data of 10 and 15 % or 25 and 30% fill density dosage forms. Percentage values of API release were used to build a linear correlation for each time point. Corresponding percentage values for the other dosage forms were calculated using the determined linear equation. Percentage values were converted into absolute ones using the absolute API content of the network and the API release from the shell was added. Afterwards, calculated released API was related to the whole amount of API.

5.5.5.26. Root Mean Square Error of Prediction (RMSEP)

For evaluation of the goodness of a prediction model, RMSEP was considered as parameter for the predictive performance. It was calculated using Equation 12 [147]:

Equation 12. Calculation of RMSEP.

$$RMSEP = \sqrt{\frac{\sum_{i=1}^{n}(y_i - \hat{y}_i)^2}{n}}$$

Calculation was performed using n as the number of samples i. For every point of time y_i was the observed and $\hat{y}_i$ the predicted value during dissolution studies.

6. Appendix

Table 17. Detailed print parameters, categorization was adopted from the slicer software.

parameter	DoE (section 3.2.3.1)	networks of single filaments (section 3.4.3)	networks of two filaments (section 3.4.4)
temperatures			
print head	180 °C	180 °C for F5 170 °C for F10	180 °C for F5 185 °C for F10
build plate	30 °C	50 °C	40 °C
layers and perimeters			
layer height			
layer height	0.2 mm	0.4 mm	0.4 mm
first layer height	0.4 mm	0.4 mm	0.4 mm
vertical shells			
perimeters	2	1	1
spiral vase	-	-	-
horizontal shells			
solid layers	2/2	0/0	0/0
quality			
extra perimeters if needed	x	x	x
avoid crossing perimeters	-	-	-
detect thin walls	x	x	x
detect bridging perimeters	x	x	x
advanced adjustments			
seam position	random	random	random
external perimeters first	-	-	-
infill			
infill			
fill density	80 %	10, 15, 20, 25, 30 %	20 %
fill pattern	rectilinear	rectilinear	rectilinear
top/bottom fil pattern	rectilinear	rectilinear	rectilinear
reducing printing time			
combine infill every	1 layer	1 layer	1 layer
only infill where needed	-	-	-
advanced			
solid infill every	0	0	0
fill angle	45°	45°	45°
solid infill threshold area	70 mm²	70 mm²	70 mm²
only retract when crossing perimeters	-	-	-
infill before perimeters	-	-	-
skirt and brim			
skirt			
loops (minimum)	1	1	1
distance from object	10 mm	10 mm	10 mm
skirt height	1 layer	1 layer	1 layer
minimum extrusion length	5 mm	5 mm	5 mm
brim			
brim width	0 mm	0 mm	0 mm
support material			
support material	-	-	-
generate support material	-	-	-
overhang threshold	-	-	-

enforce support for the first	-	-	-
raft			
raft layers	-	-	-
options for support material and raft			
contact z distance	-	-	-
pattern	-	-	-
pattern spacing	-	-	-
pattern angle	-	-	-
interface layers	-	-	-
interface pattern spacing	-	-	-
don’t support bridges	-	-	-
speed			
speed for print moves			
perimeters	7 mm/s	15 mm/s	15 mm/s
small perimeters	40 %	80 %	80 %
external perimeters	40 %	80 %	80 %
infill	7 mm/s	15 mm/s	15 mm/s
solid infill	37 %	-	-
support material	50 mm/s	50 mm/s	-
support material interface	-	-	-
bridges	10 mm/s	20 mm/s	20 mm/s
gap fill	7 mm/s	15 mm/s	-
speed for non-print moves			
travel	80 mm/s	80 mm/s	80 mm/s
modifiers			
first layer speed	7 mm/s	20 mm/s	20 mm/s
acceleration control (advanced)			
perimeters	750 mm/s²	750 mm/s²	750 mm/s²
infill	2000 mm/s²	2000 mm/s²	2000 mm/s²
bridge	0 mm/s²	0 mm/s²	0 mm/s²
first layer	750 mm/s²	750 mm/s²	750 mm/s²
default	1300 mm/s²	1300 mm/s²	1300 mm/s²
autospeed (advanced)			
max print speed	80 mm/s	80 mm/s	-
max volumetric speed	0 mm³/s	0 mm³/s	0 mm³/s
multiple extruders			
extruders			
perimeter extruder	1	1	1
infill extruder	1	1	1
solid infill extruder	1	-	-
support material/raft/skirt extruder	1	1	1
support material/raft interface extruder	-	-	-
ooze prevention			
enable	-	-	-
temperature variation	-	-	-
advanced			
interface shells	-	-	-
advanced			
extrusion width			
default extrusion width	0.37 mm	0.37 mm	0.37 mm
first layer	0.4 mm	0.4 mm	0.4 mm
perimeters	0.3 mm	0.3 mm	0.3 mm
external perimeters	0.3 mm	0.3 mm	0.3 mm

infill	0.37 mm	0.37 mm	0.37 mm
solid infill	0.37 mm	-	0.37 mm
top solid infill	0.37 mm	-	0.37 mm
support material	-	-	0.2 mm
overlap			
infill/perimeters overlap	25 mm	25 mm	25 mm
flow			
bridge flow ratio	1	1	1
other			
XY size compensation	0 mm	0 mm	0 mm
threads	2	2	-
resolution	0 mm	0 mm	0 mm
filament			
filament			
color	-	-	-
diameter	mean of the filament	1.6 mm	1.6 mm for F5 1.4 mm for F10
extrusion multiplier	1	1.2	1.2
temperature			
extruder			
first layer	0	0	0
other layers	0	0	0
bed			
first layers	0	0	0
other layers	0	0	0
cooling			
enable			
keep fan always on	-	-	-
enable auto cooling	-	-	-
fan settings			
fan speed	-	-	-
bridges fan speed	100	100	100
disable fan for the first	-	-	-
cooling thresholds			
enable fan if layer print time is below	-	-	-
slow down if layer print time is below	-	-	-
min print speed	-	-	-
extruder			
size			
nozzle diameter	0.4 mm	0.4 mm	0.4 mm
position			
extruder offset	0/0	0/0	0/0
retraction			
length	1 mm	1 mm	1 mm
lift z	0 mm	0 mm	0 mm
speed	20 mm/s	20 mm/s	20 mm/s
extra length on restart	0 mm	0 mm	0 mm
minimum travel after retraction	2 mm	2 mm	2 mm
retract on layer change	x	x	x
wipe while retracting	-	-	-
retraction when tool is disabled			
length	10 mm	10 mm	10 mm
extra length on restart	0 mm	0 mm	0 mm

7. Bibliography

[1] J. Breitkreutz, J. Boos. *Paediatric and geriatric drug delivery.* Expert Opin. Drug Deliv. 4 (2007) 37-45.

[2] G.L. Kearns, S.M. Abdel-Rahman, S.W. Alander, D.L. Blowey, J.S. Leeder, R.E. Kauffman. *Developmental pharmacology - Drug disposition, action, and therapy in infants and children.* N. Engl. J. Med. 349 (2003) 1157-1167.

[3] J.F. Schlender, M. Meyer, K. Thelen, M. Krauss, S. Willmann, T. Eissing, U. Jaehde. *Development of a Whole-Body Physiologically Based Pharmacokinetic Approach to Assess the Pharmacokinetics of Drugs in Elderly Individuals.* Clin. Pharmacokinet. 55 (2016) 1573-1589.

[4] U. Klotz. *The elderly - A challenge for appropriate drug treatment.* Eur. J. Clin. Pharmacol. 64 (2008) 225-226.

[5] K. Wening, J. Breitkreutz. *Oral drug delivery in personalized medicine: Unmet needs and novel approaches.* Int. J. Pharm. 404 (2011) 1-9.

[6] K. Wening, J. Breitkreutz. *Novel delivery device for monolithical solid oral dosage forms for personalized medicine.* Int. J. Pharm. 395 (2010) 174-181.

[7] E.J. Laukamp, K. Knop, M. Thommes, J. Breitkreutz. *Micropellet-loaded rods with dose-independent sustained release properties for individual dosing via the Solid Dosage Pen.* Int. J. Pharm. 499 (2016) 271-279.

[8] J. Norman, R.D. Madurawe, C.M.V. Moore, M.A. Khan, A. Khairuzzaman. *A new chapter in pharmaceutical manufacturing: 3D-printed drug products.* Adv. Drug Deliver. Rev. 108 (2017) 39-50.

[9] R. Petzold, H.F. Zeilhofer, W.A. Kalender. *Rapid prototyping technology in medicine - Basics and applications.* Comput. Med. Imaging Graph. 23 (1999) 277-284.

[10] J. Giannatsis, V. Dedoussis. *Additive fabrication technologies applied to medicine and health care: A review.* Int. J. Adv. Manuf. Tech. 40 (2009) 116-127.

[11] S.A. Khaled, J.C. Burley, M.R. Alexander, C.J. Roberts. *Desktop 3D printing of controlled release pharmaceutical bilayer tablets.* Int. J. Pharm. 461 (2014) 105-111.

[12] Y. Sun, S. Soh. *Printing Tablets with Fully Customizable Release Profiles for Personalized Medicine.* Adv. Mat. 27 (2015) 7847-7853.

[13] M.A. Alhnan, T.C. Okwuosa, M. Sadia, K.W. Wan, W. Ahmed, B. Arafat. *Emergence of 3D Printed Dosage Forms: Opportunities and Challenges.* Pharm. Res. 33 (2016) 1817-1832.

[14] J. Skowyra, K. Pietrzak, M.A. Alhnan. *Fabrication of extended-release patient-tailored prednisolone tablets via fused deposition modelling (FDM) 3D printing.* Eur. J. Pharm. Sci. 68 (2015) 11-17.

[15] K. Pietrzak, A. Isreb, M.A. Alhnan. *A flexible-dose dispenser for immediate and extended release 3D printed tablets.* Eur. J. Pharm. Biopharm. 96 (2015) 380-387.

[16] CAD-file for lattice structure. available at: www.thingiverse.com/thing:2522147. last access 08/15/2018.

[17] S.A. Khaled, J.C. Burley, M.R. Alexander, J. Yang, C.J. Roberts. *3D printing of five-in-one dose combination polypill with defined immediate and sustained release profiles.* J. Control. Release. 217 (2015) 308-314.

[18] S.A. Khaled, J.C. Burley, M.R. Alexander, J. Yang, C.J. Roberts. *3D printing of tablets containing multiple drugs with defined release profiles.* Int. J. Pharm. 494 (2015) 643-650.

[19] L. Zema, A. Melocchi, A. Maroni, A. Gazzaniga. *Three-Dimensional Printing of Medicinal Products and the Challenge of Personalized Therapy.* J. Pharm. Sci. 106 (2017) 1697-1705.

[20] A. Vijverman. *Hot Legal and Regulatory Issues of 3D Printed Medicinal Products.* oral presentation at: 2D and 3D Printing - A new Trend in Pharmaceutical Manufacturing: Hype or Future? Berlin, Germany. 2017.

[21] Federal Ministry of Health. *Ordinance on the Operation of Pharmacies (Verordnung über den Betrieb von Apotheken - ApBetrO).* 1987. Section 7.

[22] 3D Printing of Medical Devices: When a Novel Technology Meets Traditional Legal Principles. available at: www.reedsmith.com/en/perspectives/2015/09/3d-printing-of-medical-devices--when-a-novel-techn. last access 07/06/2018.

[23] ZipDose® Formulations. Aprecia Pharmaceuticals. available at: www.aprecia.com/zipdose-platform/zipdose-technology.php. last access 05/15/2018.

[24] J.-B. Park, B.-J. Lee, C.-Y. Kang, R.V. Tiwari, M.A. Repka. *Process analytical quality control of tailored drug release formulation prepared via hot-melt extrusion technology.* J. Drug Deliv. Sci. Technol. 38 (2017) 51-58.

[25] D. Markl, J.A. Zeitler, C. Rasch, M.H. Michaelsen, A. Müllertz, J. Rantanen, T. Rades, J. Bøtker. *Analysis of 3D Prints by X-ray Computed Microtomography and Terahertz Pulsed Imaging.* Pharm. Res. 34 (2017) 1037-1052.

[26] P. Mohan Pandey. *Slicing procedures in layered manufacturing: A review.* Rapid Prototyp. J. 9 (2003) 274-288.

[27] F.P.W. Melchels, J. Feijen, D.W. Grijpma. *A review on stereolithography and its applications in biomedical engineering.* Biomaterials. 31 (2010) 6121-6130.

[28] W.E. Katstra, R.D. Palazzolo, C.W. Rowe, B. Giritlioglu, P. Teung, M.J. Cima. *Oral dosage forms fabricated by Three Dimensional Printing™.* J. Control. Release. 66 (2000) 1-9.

[29] C.W. Rowe, W.E. Katstra, R.D. Palazzolo, B. Giritlioglu, P. Teung, M.J. Cima. *Multimechanism oral dosage forms fabricated by three dimensional printing™.* J. Control. Release. 66 (2000) 11-17.

[30] M. Schmidt, D. Pohle, T. Rechtenwald. *Selective Laser Sintering of PEEK.* CIRP Annals. 56 (2007) 205-208.

[31] F. Xie, X. He, X. Lu, S. Cao, X. Qu. *Preparation and properties of porous Ti–10Mo alloy by selective laser sintering.* Mater. Sci. Eng. C. 33 (2013) 1085-1090.

[32] F. Fina, A. Goyanes, C.M. Madla, A. Awad, S.J. Trenfield, J.M. Kuek, P. Patel, S. Gaisford, A.W. Basit. *3D printing of drug-loaded gyroid lattices using selective laser sintering.* Int. J. Pharm. 547 (2018) 44-52.

[33] P.R. Martinez, A. Goyanes, A.W. Basit, S. Gaisford. *Influence of Geometry on the Drug Release Profiles of Stereolithographic (SLA) 3D-Printed Tablets.* AAPS PharmSciTech. (2018) *3355-3361*.

[34] J.J. Adams, E.B. Duoss, T.F. Malkowski, M.J. Motala, B.Y. Ahn, R.G. Nuzzo, J.T. Bernhard, J.A. Lewis. *Conformal printing of electrically small antennas on three-dimensional surfaces.* Adv. Mat. 23 (2011) 1335-1340.

[35] A. Melocchi, F. Parietti, A. Maroni, A. Foppoli, A. Gazzaniga, L. Zema. *Hot-melt extruded filaments based on pharmaceutical grade polymers for 3D printing by fused deposition modeling.* Int. J. Pharm. 509 (2016) 255-263.

[36] Y. Jin, J. Plott, A.J. Shih. *Extrusion-based additive manufacturing of the moisture-cured silicone elstaomer.* poster at: International Solid Freeform Fabrication Symposium. Austin, USA. 2015.

[37] Q. Li, X. Guan, M. Cui, Z. Zhu, K. Chen, H. Wen, D. Jia, J. Hou, W. Xu, X. Yang, W. Pan. *Preparation and investigation of novel gastro-floating tablets with 3D extrusion-based printing.* Int. J. Pharm. 535 (2018) 325-332.

[38] W. Kempin, C. Franz, L.-C. Koster, F. Schneider, M. Bogdahn, W. Weitschies, A. Seidlitz. *Assessment of different polymers and drug loads for fused deposition modeling of drug loaded implants.* Eur. J. Pharm. Biopharm. 115 (2017) 84-93.

[39] H. Kadry, T.A. Al-Hilal, A. Keshavarz, F. Alam, C. Xu, A. Joy, F. Ahsan. *Multi-purposable filaments of HPMC for 3D printing of medications with tailored drug release and timed-absorption.* Int. J. Pharm. 544 (2018) 285-296.

[40] M. Siyawamwaya, L.C. du Toit, P. Kumar, Y.E. Choonara, P.P.P.D. Kondiah, V. Pillay. *3D printed, controlled release, tritherapeutic tablet matrix for advanced anti-HIV-1 drug delivery.* Eur. J. Pharm. Biopharm. (2018) *article in press*.

[41] P. Ravi, P.S. Shiakolas, T.R. Welch. *Poly-l-lactic acid: Pellets to fiber to fused filament fabricated scaffolds, and scaffold weight loss study.* Addit. Manuf. 16 (2017) 167-176.

[42] J.J. Water, A. Bohr, J. Boetker, J. Aho, N. Sandler, H.M. Nielsen, J. Rantanen. *Three-Dimensional Printing of Drug-Eluting Implants: Preparation of an Antimicrobial Polylactide Feedstock Material.* J. Pharm. Sci. 104 (2015) 1099-1107.

[43] A. Maroni, A. Melocchi, F. Parietti, A. Foppoli, L. Zema, A. Gazzaniga. *3D printed multi-compartment capsular devices for two-pulse oral drug delivery.* J. Control. Release. 268 (2017) 10-18.

[44] M. Kyobula, A. Adedeji, M.R. Alexander, E. Saleh, R. Wildman, I. Ashcroft, P.R. Gellert, C.J. Roberts. *3D inkjet printing of tablets exploiting bespoke complex geometries for controlled and tuneable drug release.* J. Control. Release. 261 (2017) 207-215.

[45] Interational Conference on Harmonisation of Technical Requirements for Registration of Pharmaceuticals for Human Use. *Impurities: Guideline For Residual Solvents Q3C(R6)*. 2016.

[46] A. Goyanes, A.B.M. Buanz, G.B. Hatton, S. Gaisford, A.W. Basit. *3D printing of modified-release aminosalicylate (4-ASA and 5-ASA) tablets.* Eur. J. Pharm. Biopharm. 89 (2015) 157-162.

[47] A. Goyanes, U. Det-Amornrat, J. Wang, A.W. Basit, S. Gaisford. *3D scanning and 3D printing as innovative technologies for fabricating personalized topical drug delivery systems.* J. Control. Release. 234 (2016) 41-48.

[48] T.C. Okwuosa, C. Soares, V. Gollwitzer, R. Habashy, P. Timmins, M.A. Alhnan. *On demand manufacturing of patient-specific liquid capsules via co-ordinated 3D printing and liquid dispensing.* Eur. J. Pharm. Sci. 118 (2018) 134-143.

[49] D.M. Smith, Y. Kapoor, G.R. Klinzing, A.T. Procopio. *Pharmaceutical 3D printing: Design and qualification of a single step print and fill capsule.* Int. J. Pharm. 544 (2018) 21-30.

[50] M. Sadia, A. Sośnicka, B. Arafat, A. Isreb, W. Ahmed, A. Kelarakis, M.A. Alhnan. *Adaptation of pharmaceutical excipients to FDM 3D printing for the fabrication of patient-tailored immediate release tablets.* Int. J. Pharm. 513 (2016) 659-668.

[51] A. Goyanes, A.B.M. Buanz, A.W. Basit, S. Gaisford. *Fused-filament 3D printing (3DP) for fabrication of tablets.* Int. J. Pharm. 476 (2014) 88-92.

[52] J. Boetker, J.J. Water, J. Aho, L. Arnfast, A. Bohr, J. Rantanen. *Modifying release characteristics from 3D printed drug-eluting products.* Eur. J. Pharm. Sci. 90 (2016) 47-52.

[53] A. Goyanes, H. Chang, D. Sedough, G.B. Hatton, J. Wang, A. Buanz, S. Gaisford, A.W. Basit. *Fabrication of controlled-release budesonide tablets via desktop (FDM) 3D printing.* Int. J. Pharm. 496 (2015) 414-420.

[54] A. Goyanes, P. Robles Martinez, A. Buanz, A.W. Basit, S. Gaisford. *Effect of geometry on drug release from 3D printed tablets.* Int. J. Pharm. 494 (2015) 657-663.

[55] M. Alhijjaj, P. Belton, S. Qi. *An investigation into the use of polymer blends to improve the printability of and regulate drug release from pharmaceutical solid dispersions prepared via fused deposition modeling (FDM) 3D printing.* Eur. J. Pharm. Biopharm. 108 (2016) 111-125.

[56] N. Genina, J. Holländer, H. Jukarainen, E. Mäkilä, J. Salonen, N. Sandler. *Ethylene vinyl acetate (EVA) as a new drug carrier for 3D printed medical drug delivery devices.* Eur. J. Pharm. Sci. 90 (2016) 53-63.

[57] T.C. Okwuosa, D. Stefaniak, B. Arafat, A. Isreb, K.-W. Wan, M.A. Alhnan. *A lower temperature FDM 3D printing for the manufacture of patient-specific immediate release tablets.* Pharm. Res. 33 (2016) 2704-2712.

[58] T.C. Okwuosa, B.C. Pereira, B. Arafat, M. Cieszynska, A. Isreb, M.A. Alhnan. *Fabricating a shell-core delayed release tablet using dual FDM 3D printing for patient-centred therapy.* Pharm. Res. 34 (2017) 427-437.

[59] R.C.R. Beck, P.S. Chaves, A. Goyanes, B. Vukosavljevic, A. Buanz, M. Windbergs, A.W. Basit, S. Gaisford. *3D printed tablets loaded with polymeric nanocapsules: An innovative approach to produce customized drug delivery systems.* Int. J. Pharm. 528 (2017) 268-279.

[60] Z. Muwaffak, A. Goyanes, V. Clark, A.W. Basit, S.T. Hilton, S. Gaisford. *Patient-specific 3D scanned and 3D printed antimicrobial polycaprolactone wound dressings.* Int. J. Pharm. 527 (2017) 161-170.

[61] C. Rauwendaal. *Polymer Extrusion.* Carl Hanser Verlag. Munich, Germany. 2014.

[62] P.F. Costa, A.M. Puga, L. Díaz-Gomez, A. Concheiro, D.H. Busch, C. Alvarez-Lorenzo. *Additive manufacturing of scaffolds with dexamethasone controlled release for enhanced bone regeneration.* Int. J. Pharm. 496 (2015) 541-550.

[63] C. Wang, J. Wang, C. Yu, B. Wu, Y. Wang, W. Li. *A novel method for the determination of steady-state torque of polymer melts by HAAKE MiniLab.* Polym. Test. 33 (2014) 138-144.

[64] J. Zhang, X. Feng, H. Patil, R.V. Tiwari, M.A. Repka. *Coupling 3D printing with hot-melt extrusion to produce controlled-release tablets.* Int. J. Pharm. 519 (2017) 186-197.

[65] J. Zhang, W. Yang, A.Q. Vo, X. Feng, X. Ye, D.W. Kim, M.A. Repka. *Hydroxypropyl methylcellulose-based controlled release dosage by melt extrusion and 3D printing: Structure and drug release correlation.* Carbohyd. Polym. 177 (2017) 49-57.

[66] J.B. Field, L. Graf, K.P. Link. *The effect of methylxanthines on the hypocoagulability induced by chloroform in the dog.* Blood. 7 (1952) 445-453.

[67] S2k-Leitlinie zur Diagnostik und Therapie von Patienten mit Asthma. available at: www.awmf.org/uploads/tx_szleitlinien/020-009l_S2k_Asthma_Diagnostik_Therapie_2017-11_1.pdf. last access 07/08/2018.

[68] S2k - Leitlinie zur Diagnostik und Therapie von Patienten mit chronisch obstruktiver Bronchitis und Lungenemphysem (COPD). available at: http://www.awmf.org/uploads/tx_szleitlinien/020-006l_S2k_COPD_chronisch-obstruktive-Lungenerkrankung_2018-01.pdf. last access 07/08/2018.

[69] M.E. Hopkins, R.V. MacKenzie-Ross. *Case Report: The risks associated with chronic theophylline therapy and measures designed to improve monitoring and management.* BMC Pharmacol. Toxicol. 17 (2016) 13.

[70] P.J. Barnes. *Theophylline.* Am. J. Respir. Crit. Care Med. 188 (2013) 901-906.

[71] E. Reitz. *Extrudierte feste Dispersionen zur Verbesserung der Lösungsgeschwindigkeit und Bioverfügbarkeit (PhD thesis in German).* Institute of Pharmaceutics and Biopharmaceutics. Heinrich Heine University, Düsseldorf, Germany. 2014. pp. 23.

[72] E. Suzuki, K. Shimomura, K. Sekiguchi. *Thermochemical study of theophylline and its hydrate.* Chem. Pharm. Bull. 37 (1989) 493-497.

[73] I. Fix. *Anwendungen der quantitativen Röntgendiffraktometrie (QXRD) in der pharmazeutischen Analytik (PhD thesis in German).* Faculty of Mathematics and Natural Sciences. University of Bonn, Bonn, Germany. 2004. pp. 31-33.

[74] Theophylline containing dosage forms. available at: www.gelbe-liste.de/suche/theophyllin. last access 07/08/2018.

[75] European Directorate for the Quality of Medicines. European Pharmacopoeia 9.0. *Ammonio methacrylate copolymer (type A).* Deutscher Apotheker Verlag. Stuttgart, Germany. 2017.

[76] T. Quinten, G.P. Andrews, T. De Beer, L. Saerens, W. Bouquet, D.S. Jones, P. Hornsby, J.P. Remon, C. Vervaet. *Preparation and evaluation of sustained-release matrix tablets based on metoprolol and an acrylic carrier using injection moulding.* AAPS PharmSciTech. 13 (2012) 1197-1211.

[77] J. Siepmann, F. Siepmann. *Stability of aqueous polymeric controlled release film coatings.* Int. J. Pharm. 457 (2013) 437-445.

[78] K. Knop, M. Kremer, S. Ridder, P. Kleinebudde. *In vitro dissolution behavior of extended-release theophylline capsules in media containing alcohol.* poster at: DPhG Annual meeting. Düsseldorf. 2015.

[79] S.A. Kucera, L.A. Felton, J.W. McGinity. *Physical aging in pharmaceutical polymers and the effect on solid oral dosage form stability.* Int. J. Pharm. 457 (2013) 428-436.

[80] D. Desai, H. Sandhu, N. Shah, W. Malick, H. Zia, W. Phuapradit, S.R.K. Vaka. *Selection of Solid-State Plasticizers as Processing Aids for Hot-Melt Extrusion.* J. Pharm. Sci. 107 (2018) 372-379.

[81] M.A. Frohoff-Hülsmann, A. Schmitz, B.C. Lippold. *Aqueous ethyl cellulose dispersions containing plasticizers of different water solubility and hydroxypropyl methylcellulose as coating material for diffusion pellets: I. Drug release rates from coated pellets.* Int. J. Pharm. 177 (1999) 69-82.

[82] R.V. Nellore, G. Singh Rekhi, A.S. Hussain, L.G. Tillman, L.L. Augsburger. *Development of metoprolol tartrate extended-release matrix tablet formulations for regulatory policy consideration.* J. Control. Release. 50 (1998) 247-256.

[83] Y. Teng, Z. Qiu, H. Wen. *Systematical approach of formulation and process development using roller compaction.* Eur. J. Pharm. Biopharm. 73 (2009) 219-229.

[84] European Directorate for the Quality of Medicines. European Pharmacopoeia 9.0. *Stearic Acid.* Deutscher Apotheker Verlag. Stuttgart, Germany. 2015.

[85] European Directorate for the Quality of Medicines. European Pharmacopoeia 9.0. *Macrogols.* Deutscher Apotheker Verlag. Stuttgart, Germany. 2017.

[86] S. Güres, P. Kleinebudde. *Dissolution from solid lipid extrudates containing release modifiers.* Int. J. Pharm. 412 (2011) 77-84.

[87] E. Gomaa, A.S. Abu Lila, A.A. Hasan, F.E.S. Ghazy. *Preparation and characterization of intravaginal vardenafil suppositories targeting a complementary treatment to boost in vitro fertilization process.* Eur. J. Pharm. Sci. 111 (2018) 113-120.

[88] Y. Yang, H. Wang, H. Li, Z. Ou, G. Yang. *3D printed tablets with internal scaffold structure using ethyl cellulose to achieve sustained ibuprofen release.* Eur. J. Pharm. Sci. 115 (2018) 11-18.

[89] C.I. Gioumouxouzis, A. Baklavaridis, O.L. Katsamenis, C.K. Markopoulou, N. Bouropoulos, D. Tzetzis, D.G. Fatouros. *A 3D printed bilayer oral solid dosage form combining metformin for prolonged and glimepiride for immediate drug delivery.* Eur. J. Pharm. Sci. 120 (2018) 40-52.

[90] C. Wu, J.W. McGinity. *Influence of methylparaben as a solid-state plasticizer on the physicochemical properties of Eudragit® RS PO hot-melt extrudates.* Eur. J. Pharm. Biopharm. 56 (2003) 95-100.

[91] M.A. Repka, J.W. McGinity. *Influence of Vitamin E TPGS on the properties of hydrophilic films produced by hot-melt extrusion.* Int. J. Pharm. 202 (2000) 63-70.

[92] C. Korte, J. Quodbach. *Formulation development and process analysis of drug-loaded filaments manufactured via hot-melt extrusion for 3D-printing of medicines.* Pharm. Dev. Technol. 23 (2018) 1117-1127.

[93] K. Kolter, M. Karl, A. Gryczke. *Hot-Melt Extrusion with BASF Pharma Polymers.* BASF SE Pharma Ingredients & Services. Ludwigshafen, Germany. 2012.

[94] R. Meier, K.-P. Moll, M. Krumme, P. Kleinebudde. *Impact of fill-level in twin-screw granulation on critical quality attributes of granules and tablets.* Eur. J. Pharm. Biopharm. 115 (2017) 102-112.

[95] European Directorate for the Quality of Medicines. European Pharmacopoeia 9.0. *Theophylline.* Deutscher Apotheker Verlag. Stuttgart, Germany. 2017.

[96] W. Kempin, V. Domsta, G. Grathoff, I. Brecht, B. Semmling, S. Tillmann, W. Weitschies, A. Seidlitz. *Immediate Release 3D-Printed Tablets Produced Via Fused Deposition Modeling of a Thermo-Sensitive Drug.* Pharm. Res. 35 (2018).

[97] W. Grellmann, S. Seidler. *Kunststoffprüfung.* Carl Hanser Verlag. Munich, Germany. 2015.

[98] R.J. Hernandes. *Polymer Properties.* in: The Wiley Encyclopedia of Packaging Technology K.L. Yam (Ed.). John Wiley & Sons. Hoboken, USA. 2009. pp. 993-1000.

[99] C. Bonten. *Kunststofftechnik.* Carl Hanser Verlag. Munich, Germany. 2014.

[100] Deutsches Institut für Normung. *DIN EN ISO 604: Kunststoffe - Bestimmung von Druckeigenschaften*. Beuth Verlag GmbH. Berlin, Germany. 2003.

[101] Deutsches Institut für Normung. *DIN 527-1: Kunststoffe - Bestimmung der Zugeigenschaften - Teil 1: Allgemeine Grundsätze*. Beuth Verlag GmbH. Berlin, Germany. 2012.

[102] Deutsches Institut für Normung. *DIN 66001: Informationsverarbeitung - Sinnbilder und ihre Anwendung*. Beuth Verlag GmbH. Berlin, Germany. 1983.

[103] B.C. Hancock, G. Zografi. *The Relationship Between the Glass Transition Temperature and the Water Content of Amorphous Pharmaceutical Solids.* Pharm. Res. 11 (1994) 471-477.

[104] S. Thakral, N.K. Thakral, D.K. Majumdar. *Eudragit®: a technology evaluation.* Expert Opin. Drug Deliv. 10 (2013) 131-149.

[105] R. Simha, R.F. Boyer. *On a General Relation Involving the Glass Temperature and Coefficients of Expansion of Polymers.* J. Chem. Phys. 37 (1962) 1003-1007.

[106] Z. Cernosek, E. Holubová, E. Cernoskova, M. Liska. *Enthalpic relaxation and the glass transition.* J. Optoelectron. Adv. M. 4 (2002) 489-503.

[107] S.Y. Lin, H.L. Yu. *Microscopic Fourier transform infrared/differential scanning calorimetry system used to study the different thermal behaviors of polymethacrylate copolymers of Eudragits RS, RL, E 30D, or E.* J. Appl. Polym. Sci. 78 (2000) 829-835.

[108] Interational Conference on Harmonisation of Technical Requirements for Registration of Pharmaceuticals for Human Use. *Stability Testing of New Drug Substances and Products Q1A(R2)*. 2003.

[109] U.S.F.a.D. Administration. *Guidance for Industry: Immediate Release Solid Oral Dosage Forms*. 1995.

[110] P.R. Wahl, G. Hörl, D. Kaiser, S. Sacher, C. Rupp, G. Shlieout, J. Breitenbach, G. Koscher, J.G. Khinast. *In-line measurement of residence time distribution in melt extrusion via video analysis.* Polym. Eng. Sci. 58 (2018) 170-179.

[111] H. Mangal, P. Kleinebudde. *Experimental determination of residence time distribution in continuous dry granulation.* Int. J. Pharm. 524 (2017) 91-100.

[112] D. Ma, A. Djemai, C.M. Gendron, H. Xi, M. Smith, J. Kogan, L. Li. *Development of a HPMC-based controlled release formulation with hot melt extrusion (HME).* Drug Dev. Ind. Pharm. 39 (2013) 1070-1083.

[113] European Directorate for the Quality of Medicines. European Pharmacopoeia 9.0. *Uniformity of Dosage Units.* Deutscher Apotheker Verlag. Stuttgart, Germany. 2017.

[114] P.M.C. Lacey. *Developments in the theory of particle mixing.* J. Appl. Chem. Biotechnol. 4 (1954) 257-267.

[115] S. Lakio, T. Ervasti, P. Tajarobi, H. Wikström, M. Fransson, A.-P. Karttunen, J. Ketolainen, S. Folestad, S. Abrahmsén-Alami, O. Korhonen. *Provoking an end-to-end continuous direct compression line with raw materials prone to segregation.* Eur. J. Pharm. Sci. 109 (2017) 514-524.

[116] J.-H. Guo. *Aging processes in pharmaceutical polymers.* Pharm. Sci. Technol. Today. 2 (1999) 478-483.

[117] M.H. Cohen, D. Turnbull. *Molecular transport in liquids and glasses.* J. Chem. Phys. 31 (1959) 1164-1169.

[118] L.C.E. Struik. *Physical aging in plastics and other glassy materials.* Polym. Eng. Sci. 17 (1977) 165-173.

[119] R. Greiner, F.R. Schwarzl. *Volume relaxation and physical aging of amorphous polymers I. Theory of volume relaxation after single temperature jumps.* Colloid Polym. Sci. 267 (1989) 39-47.

[120] G. Hudovornik, F. Vrečer. *Impact of the curing parameters on drug release from Eudragit RS and RL 30D coated pellets: Design of experiments.* J. Drug Deliv. Sci. Technol. 30 (2015) 146-153.

[121] A. Goyanes, F. Fina, A. Martorana, D. Sedough, S. Gaisford, A.W. Basit. *Development of modified release 3D printed tablets (printlets) with pharmaceutical excipients using additive manufacturing.* Int. J. Pharm. 527 (2017) 21-30.

[122] N.G. Solanki, M. Tahsin, A.V. Shah, A.T.M. Serajuddin. *Formulation of 3D Printed Tablet for Rapid Drug Release by Fused Deposition Modeling: Screening Polymers for Drug Release, Drug-Polymer Miscibility and Printability.* J. Pharm. Sci. 107 (2018) 390-401.

[123] J.E. Seppala, K.D. Migler. *Infrared thermography of welding zones produced by polymer extrusion additive manufacturing.* Addit. Manuf. 12 (2016) 71-76.

[124] Deutsches Institut für Normung. *DIN 66025-2: Programmaufbau für numerisch gesteuerte Arbeitsmaschinen - Wegbedingungen und Zusatzfunktionen*. Beuth Verlag GmbH. Berlin, Germany. 1988.

[125] RepRap Wiki. available at: reprap.org/wiki/RepRap. last access 04/09/2018.

[126] Deutsches Institut für Normung. *DIN 66025-1: Programmaufbau für numerisch gesteuerte Arbeitsmaschinen - Allgemeines*. Beuth Verlag GmbH. Berlin, Germany. 1983.

[127] P.V. Danckwerts. *Continuous flow systems. Distribution of residence times.* Chem. Eng. Sci. 2 (1953) 1-13.

[128] G. Verstraete, A. Samaro, W. Grymonpré, V. Vanhoorne, B. Van Snick, M.N. Boone, T. Hellemans, L. Van Hoorebeke, J.P. Remon, C. Vervaet. *3D printing of high drug loaded dosage forms using thermoplastic polyurethanes.* Int. J. Pharm. 536 (2018) 318-325.

[129] A. Goyanes, J. Wang, A. Buanz, R. Martínez-Pacheco, R. Telford, S. Gaisford, A.W. Basit. *3D Printing of Medicines: Engineering Novel Oral Devices with Unique Design and Drug Release Characteristics.* Mol. Pharm. 12 (2015) 4077-4084.

[130] J.H. van't Hoff, E. Cohen, T. Ewan. *Studies in Chemical Dynamics.* E. Cohen (Ed.). Frederik Muller & Co. Amsterdam, Netherlands. 1896.

[131] M. Vollmer. *Infrared thermal imaging : fundamentals, research and applications.* Wiley-VCH. Weinheim, Germany. 2010.

[132] F. Xu, S. Qiu, J.-G. Liang, L.-X. Sun, F. Li. *Low Temperature Heat Capacity and Thermal Analysis of Caffeine, Theophylline and Aminophylline.* Acta Phys. Chim. Sin. 26 (2010) 2096-2102.

[133] T. Gondová, J. Gonda, P. Králik. *Molar heat capacities of some derivatives of uracil and theophylline.* Thermochim. Acta. 225 (1993) 37-41.

[134] V. Bares, B. Wunderlich. *Heat Capacity of Molten Polymers.* J Polym Sci Part A-2 Polym Phys. 11 (1973) 861-873.

[135] C. Korte, J. Quodbach. *3D-Printed Network Structures as Controlled-Release Drug Delivery Systems: Dose Adjustment, API Release Analysis and Prediction.* AAPS PharmSciTech. 19 (2018) 3333-3342.

[136] K. Knop, P. Kleinebudde. *In vitro dissolution behavior of extended release theophylline tablets in ethanolic media.* poster at: 1st European Conference on Pharmaceutics. Reims. 2015.

[137] P.L. Ritger, N.A. Peppas. *A simple equation for description of solute release I. Fickian and non-fickian release from non-swellable devices in the form of slabs, spheres, cylinders or discs.* J. Control. Release. 5 (1987) 23-36.

[138] R.W. Korsmeyer, R. Gurny, E. Doelker, P. Buri, N.A. Peppas. *Mechanisms of solute release from porous hydrophilic polymers.* Int. J. Pharm. 15 (1983) 25-35.

[139] J. Siepmann, F. Siepmann. *Modeling of diffusion controlled drug delivery.* J. Control. Release. 161 (2012) 351-362.

[140] T. Higuchi. *Rate of release of medicaments from ointment bases containing drugs in suspension.* J. Pharm. Sci. 50 (1961) 874-875.

[141] T. Higuchi. *Mechanism of sustained-action medication. Theoretical analysis of rate of release of solid drugs dispersed in solid matrices.* J. Pharm. Sci. 52 (1963) 1145-1149.

[142] A. Pestieau, B. Evrard. *In vitro biphasic dissolution tests and their suitability for establishing in vitro-in vivo correlations: A historical review.* Eur. J. Pharm. Sci. 102 (2017) 203-219.

[143] A. Abebe, I. Akseli, O. Sprockel, N. Kottala, A.M. Cuitiño. *Review of bilayer tablet technology.* Int. J. Pharm. 461 (2014) 549-558.

[144] J. Hergel, S. Lefebvre. *Clean color: Improving multi-filament 3D prints.* Comput. Graph. Forum. 33 (2014) 469-478.

[145] A. Gryczke. *ExtruVis 3 Operating Manual Version 1.0.0.37.* 2016.

[146] European Directorate for the Quality of Medicines. European Pharmacopoeia 9.0. *Recommendations on dissolution testing.* Deutscher Apotheker Verlag. Stuttgart, Germany. 2017.

[147] S. Barimani, P. Kleinebudde. *Monitoring of tablet coating processes with colored coatings.* Talanta. 178 (2018) 686-697.

8. Eidesstattliche Versicherung

Ich versichere an Eides Statt, dass die Dissertation von mir selbständig und ohne unzulässige fremde Hilfe unter Beachtung der „Grundsätze zur Sicherung guter wissenschaftlicher Praxis an der Heinrich-Heine-Universität Düsseldorf“ erstellt worden ist.

Carolin Korte

9. Danksagung

Die vorliegende Arbeit ist am Institut für Pharmazeutische Technologie und Biopharmazie der Heinrich-Heine-Universität Düsseldorf entstanden. Mein besonderer Dank gilt meinem Doktorvater, Prof. Dr. Jörg Breitkreutz, für die Aufnahme in seinen Arbeitskreis und die Möglichkeit ein solch innovatives Thema im Rahmen einer Dissertation bearbeiten zu dürfen. Die vielen fruchtbaren fachlichen Diskussionen mit ihm und seinen kreativen Denkanstöße waren sehr motivierend und entscheidend für das Gelingen der Arbeit. Ich möchte mich auch dafür bedanken, dass er mir ermöglicht hat an zahlreichen Konferenzen und Fortbildungen teilzunehmen. Darüber hinaus bedanke ich mich sehr dafür, dass er sich nach Diebstahl des 3D-Druckers für eine überaus schnelle und unkomplizierte Beschaffung eines neuen Geräts eingesetzt hat.

Bei Dr. Julian Quodbach möchte ich mich für seine Betreuung und seine permanente Ansprechbarkeit bzgl. meines Promotionsthemas und vieler anderer Themen sowie für das Korrekturlesen von Abstracts, Postern, Papern und der Dissertation herzlich bedanken. Meinem Mentor, Prof. Dr. Dr. h.c. Peter Kleinebudde, danke ich für viele konstruktive und motivierende Diskussionen, insbesondere in Bezug auf mein Dissertationsthema und 3D-Druck im Allgemeinen. Vielen Dank gilt auch Dr. Klaus Knop, der die vorliegende Dissertation Korrektur gelesen hat und mir bei fachlichen und nicht fachlichen Fragestellungen zur Seite gestanden hat.

Stefan Stich danke ich für die schnelle Anfertigung von Extruder Düsenplatten und speziellen Sinkern für die Freisetzungsapparatur. Bei Karin Matthée bedanke ich mich für die Durchführung unzähliger DSC Messungen und für ihre Bereitschaft die Ergebnisse mit mir zu diskutieren. Dorothee Eikeler danke ich sehr für ihre Unterstützung, wenn ich bei praktischen Arbeiten im Labor zwei helfende Hände brauchte. Für die Hilfe bei der Methodenentwicklung für die µCT-Aufnahmen möchte ich mich bei Raphael Wiedey bedanken. Bei Svenja Niese bedanke ich mich für den 3D-Druck der in Figure 1 dargestellten Form. Fabian Loose und Tilmann Spitz vom Institut für Produktentwicklung und Kontruktionstechnik der TH Köln danke ich für die Anfertigung der neuen Druckköpfe (print heads type II) und die entsprechende Implementierung. Bei Joana Schlink und Kathrin Joeris bedanke ich mich für ihre praktische Mithilfe bei den Untersuchungen zur Alterung von Filamenten. Lisa Man danke ich für ihre außerordentliche Hilfsbereitschaft in allen organisatorischen Belangen.

Dr. Elisabeth Lenz, Dr. Sandra Meier und Dr. Robin Meier danke ich für die besondere Unterstützung am Anfang der Promotionszeit sowohl auf fachlicher als auch auf privater Ebene. Das hat mir den Einstieg sehr erleichtert. Kira Adam, Dorothee Eikeler, Julia Harting, Svenja Korthues, Svenja Niese, Sebastian Pohl, Hanna Ponsar, Isabell Speer und Raphael

Wiedey danke ich für eine tolle Arbeitsatmosphäre, die gemeinsamen Stunden und die fortwährende emotionale und fachliche Unterstützung. Großen Dank möchte ich auch an Claudia Grevelding richten, die für Angelegenheiten aller Art immer ein offenes Ohr hatte und mich das ein oder andere Mal mit dem nötigen Abstand auf den Boden der Tatsachen zurückgeholt hat.

Zuletzt möchte ich mich im Besonderen bei meinen Eltern und meiner Schwester für ihre Unterstützung bedanken. Ihr habt immer zu mir gestanden, mich gut beraten und mir einen Rückzugsort geboten. Vielen Dank, dass ihr mir das Studium und die Promotion auf diese Weise ermöglicht habt.